11-5-2015

# Photoacoustic Imaging for Ovarian Cancer Detection: System Development and Classification Algorithm

Hai Li
*University of Connecticut - Storrs*, hal09003@engr.uconn.edu

**Photoacoustic Imaging for Ovarian Cancer Detection: System Development and Classification Algorithm**

Hai Li, PhD

University of Connecticut, 2015

Ovarian cancer is relatively rare but it has the highest mortality with a five-year survival rate of only 30% comparing with other gynecologic cancers. Most of ovarian cancers are diagnosed at late stages because of no efficacious screening techniques. So there is an urgent need to develop new imaging techniques for early stage ovarian cancer detection. Photoacoustic imaging (PAI) inherently combines the merits of optical imaging and ultrasound imaging. In PAI, photoacoustic waves are generated by illuminating tissue samples with a short laser pulse. Photoacoustic waves are then measured by ultrasound transducers to reconstruct optical absorption at ultrasound resolution, which is directly related to tumor angiogenesis.

This research mainly focuses on the development of real-time co-registered ultrasound (US)/ photoacoustic tomography (PAT) imaging system and a classification algorithm for diagnosis of malignant vs. benign ovarian tissues. In this study, two versions of US/PAT systems were designed and implemented. To achieve real-time imaging capability for clinical application, efforts had been devoted to hardware structure and software algorithm optimization. We have achieved real-time imaging capability of 15 frames per second for patient studies. The system's imaging capability is demonstrated in phantom and animal studies. A classification algorithm for diagnosis of malignant vs. benign ovarian tissues is the second topic of this search. Features from US/PAT imaging data, which may be helpful for ovarian cancer diagnosis, are extracted. Feature selection method is applied to select optimal subset for logistic regression classifier and supporter vector machine (SVM) classifier and promising results have obtained. The frame work set by this classification algorithm can be extended by having more features and advanced classifiers in the future.

# Photoacoustic Imaging for Ovarian Cancer Detection: System Development and Classification Algorithm

Hai Li

B.S., Xi'an Jiaotong University, 2006

M.S., Xi'an Jiaotong University, 2009

A Dissertation

Submitted in Partial Fulfillment of the

Requirements for the Degree of

Doctor of Philosophy

at the

University of Connecticut

2015

APPROVAL PAGE

Doctor of Philosophy Dissertation

**Photoacoustic Imaging for Ovarian Cancer Detection: System Development and Classification Algorithm**

Presented by

Hai Li, B.S., M.S.

Major Advisor

_____

Quing Zhu

Associate Advisor

_____

Rajeev Bansal

Associate Advisor

_____

Peter Willett

University of Connecticut
2015

**Acknowledgements**

First of all, I would like to thank my advisor Prof. Quing Zhu to recruit me as a research assistant of Optical and Ultrasound Imaging Laboratory of University of Connecticut (UCONN) in 2009, especially under the circumstances that I had no research paper before that. After adapting to the study and research of our lab, I learnt a lot from her to finish my PhD degree. Her knowledge on ultrasound and optical imaging, management and leadership of our lab, and even her social skills played an important guide for both my research and personal mind development.

I appreciate the help from Dr Andre Aguirre. I had one year co-work experience with him from 2009 to 2010. In that year, I started the learning of ultrasound imaging from him. He was an expert in every stage of ultrasound imaging and was nice and considerate to everyone in our lab. His patience, organism about experimental data and sunny life belief gave me a great positive impact on my research and daily life.

Here, I present special thanks for my dear lab mate, Dr Umar Alqasemi. We had 4 years collaboration with each other. We built our co-registered ultrasound and photoacoustic imaging system from scratch. It was a good experience to discuss with him about every aspect of our system. Although we had some disagreements during the development, we finally made the agreement and implemented our design, which was our pride in our lives. His innovative thinking and wide knowledge in the development of our system was what I was pursuing during my PhD.

I also appreciate the help from all my associate advisors, Prof. Rajeev Bansal, Prof. Peter Willet, defense participating faculty Dr Patrick Kumavor and Prof. Guoan Zhen for their knowledge and guidance in my research.

I'd like to thank any person giving me help and suggestion for my research during my PhD, including all the past and present members of the Optical and Ultrasound laboratory and my

friends in life. It's a pleasure to work with all of them. Here I'd like to mention Dr Chen Xu, Dr Nrusingh Biswal, Dr Patrick Kumavor, Dr Yi Yang, Dr Tianheng Wang, Dr Saeid Zanganeh, Dr Behnoosh Tavakoli, Guangqian Yuan, Dr Hassan Salehi, Akram Abuteen, Feifei Zhou, Sreyankar Nandy, Mohsen Erfanzadeh, Hamed VaVadi, Atahar Kamal Mostafa, Donald McMenemy, Murad Althobaiti, Jinglong Li and Shihab Uddin. In addition, I also want to bring my thanks to Dr Yibo Zhu and Dr Son Le in Computer Science and Engineering Department of UCONN for helping me to debug my program and provide suggestion about software structure.

I could not finish my PhD without the help and encouragement from my family, especially from my wife Rong Zhou and my mother-in-law. They undertook the majority of the load of raising my daughter Zoe while my wife was even also pursuing her PhD in UCONN.

# Table of Contents

# List of Figures

# List of Tables

# Chapter 1 Introduction

To date, there are four common medical imaging modalities: ultrasound imaging, X-ray computed tomography (CT), positron emission tomography (PET) and magnetic resonance imaging (MRI). They are widely used in daily diagnosis. However, these modalities have their own limitations which limit their application, especially on ovarian tissues. Ultrasound imaging can achieve real-time imaging and is less expensive than other three modalities. However, its contrast only comes from the mechanical properties of tissue. X-ray based modalities have a relatively high biological hazards of ionizing radiation and its contrast mechanism is only based on one tissue parameter: electron density. It extensively overlaps between normal and diseased tissues.[1] MRI imaging can provide detailed diagnostic images of most of the important organs and tissues. However its high cost of operation and imaging conditions prevent its wide application due to patient selectiveness.

Optical imaging is currently emerging as a promising new medical imaging modality. Light can provide high sensitivity to functional changes, either via intrinsic changes in absorption, fluorescence, or scatter, or through the use of extrinsic contrast agents. Hemoglobin is the most commonly measured intrinsic chromospheres in living tissue. The use of absorbing and fluorescent dyes can provide highly specific optical contrast enhancement. Comparing with other clinical imaging modalities, optical imaging is relatively low costly. Besides, it is non-ionizing and can provide a broad range of contrast mechanism. The major challenge of optical imaging is to overcome the effects of light scattering, which strongly affects penetration depth and imaging resolution.[2]

Photoacoustic imaging (PAI) is a hybrid imaging technique of optical imaging and ultrasound imaging.[3-15]Depending on the detection depth, it is divided into two categories:

photoacoustic microscopy (PAM) and photoacoustic tomography (PAT). Both of them are based on photoacoustic effect: non-ionizing short duration laser pulses are illuminated upon tissue surfaces. Part of the laser energy is absorbed and converted into heat which leads to transient thermoelastic expansion and generates wideband ultrasound wave. The generated photoacoustic waves are collected and used for reconstruction of 2D/3D absorption map inside tissues. In PAM, usually both laser and ultrasound have same foci to achieve best solution (15um or less). The imaging frame rate usually is only limited by its laser pulse repetition rate and solution is determined by ultrasound transducer center frequency. However, its penetration depth is very limited (2~3 mm) [16]. In the other hand, PAT is more applicable in clinical cases because it uses diffusive light and several centimeters can be achieved. The resolution of photoacoustic imaging is determined by ultrasound transducer bandwidth and its aperture size. The contrast of photoacoustic imaging comes from the light absorption distribution inside tissue which is directly related to tumor angiogenesis[17, 18]. Tumor angiogenesis is a key process for tumor growth and metastasis. The clinical probe (3-10MHz) plus near infrared light in the range of 700nm to 900nm in photoacoustic tomography system can achieve up to 5cm penetration depth. The optical contrast and ultrasound resolution grants PAT a great potential in clinical study. Theories about photoacoustic imaging and reconstruction methods are presented in chapter 2.

Chapter 3 describes the details of system design of our real-time co-registered ultrasound and photoacoustic imaging.[19] Front end design, communication, signal processing and system optimization are discussed step by step from the very beginning FPGA-DSP-PC structure to multi-FPGA-PC structure. Animal studies and contrast agents experiments are presented in this chapter.

Chapter 4 shows a novel photoacoustic imagining enhancement agent which may be able to improve our signal to noise ratio in the future clinical study. Its performance for signal

enhancement was demonstrated from in-vivo mouse models and verified with fluorescent imaging in this chapter, which is much better than traditional dyes.

After building the real-time system, it is used for clinical data accumulation. In chapter 5, a classification algorithm for benign (normal) and malignant ovaries diagnosis is discussed based on *ex vivo* photoacoustic data.[20] Features from multiple aspects of photoacoustic data are collected and analyzed for its physiological backgrounds. Methods of feature selection are also discussed to get the optimal sets of feature for final classification. New features in ultrasound domain and clinical observation are also introduced which may be helpful for in-vivo diagnosis. Although classification for in-vivo diagnosis needs more consideration in the future, this classification method has already opened a window for further development of computer-aided diagnosis for early stage ovary cancer detection.

## References


1. P.E. Kim and C.S. Zee, "Imaging of the cerebrum," Neurosurgery 61(1 Suppl), 123-46; discussion 146 (2007).

2.E.M. Hillman, "Optical brain imaging in vivo: techniques and applications from animal to man," Journal of biomedical optics 12(5), 051402 (2007).

3. V.G. Andreev, A.A. Karabutov, S.V. Solomatin, E.V. Savateeva, V. Aleinikov, Y.V. Zhulina, R.D. Fleming and A. Oraevsky, "Optoacoustic tomography of breast cancer with arc-array transducer," Biomedical Optoacoustics 3916, 36-47 (2000).

4. R.A. Kruger, P. Liu, Y.R. Fang and C.R. Appledorn, "Photoacoustic ultrasound (PAUS)--reconstruction tomography," Medical physics 22(10), 1605-1609 (1995).

5. A. Oraevsky and A.A. Karabutov, "Ultimate sensitivity of time-resolved optoacoustic detection," Biomedical Optoacoustics 3916(1), 228-239 (2000).

6. X. Wang, Y. Pang, G. Ku, X. Xie, G. Stoica and L.V. Wang, "Noninvasive laserinduced photoacoustic tomography for structural and functional in vivo imaging of the brain," Nature Biotechnology 21(7), 803-806 (2003).

7. B.T. Cox and P.C. Beard, "Fast calculation of pulsed photoacoustic fields in fluids using k-space methods," The Journal of the Acoustical Society of America 117(6), 3616-3627 (2005).

8. C.G. Hoelen, F.F. de Mul, R. Pongers and A. Dekker, "Three-dimensional photoacoustic imaging of blood vessels in tissue," Optics Letters 23(8), 648-650 (1998).

9. A. Karabutov, E.V. Savateeva, N.B. Podymova and A.A. Oraevsky, "Backward mode detection of laser-induced wide-band ultrasonic transients with optoacoustic transducer," Journal of Applied Physics 87, 2003-2014 (2000).

10. R.A. Kruger, D.R. Reinecke and G.A. Kruger, "Thermoacoustic computed tomography--technical considerations," Medical physics 26(9), 1832-1837 (1999).

11. G. Ku, X. Wang, G. Stoica and L.V. Wang, "Multiple-bandwidth photoacoustic tomography," Physics in Medicine and Biology 49(7), 1329-1338 (2004).

12. G. Paltauf, J.A. Viator, S.A. Prahl and S.L. Jacques, "Iterative reconstruction algorithm for optoacoustic imaging," The Journal of the Acoustical Society of America 112(4), 1536-1544 (2002).

13. S. Sethuraman, J.H. Amirian, S.H. Litovsky, R.W. Smalling and S.Y. Emelianov, "Spectroscopic intravascular photoacoustic imaging to differentiate atherosclerotic plaques," Optics Express 16(5), 3362-3367 (2008).

14. L. V. Wang and H. Wu, Biomedical Optics: Principles and Imaging, Wiley, Hoboken, NJ, (2007).

15. L.V. Wang, "Tutorial on Photoacoustic Microscopy and Computed Tomography," IEEE Journal of Selected Topics in Quantum Electronics 14(1), 171-179 (2008).

16. J. Gamelin, A. Aguirre, A. Maurudis, F. Huang, D. Castillo, L.V. Wang and Q. Zhu, "Curved array photoacoustic tomographic system for small animal imaging," Journal of Biomedical Optics 13(2), 024007 (2008).

17. J.J. Niederhauser, M. Jaeger, R. Lemor and P. Weber, "Combined Ultrasound and Optoacoustic System for Real-Time High-Contrast Vascular Imaging in Vivo," IEEE Transactions on Medical Imaging 24(4), 436-440 (2005).

18. P. Vaupel, F. Kallinowski and P. Okunieff, "Blood flow, oxygen and nutrient supply, and metabolic microenvironment of human tumors: a review," Cancer Research 49(23), 6449-6465 (1989).

19. Umar Alqasemi, Hai Li, Guangqian Yuan, Patrick Kumavor, Saeid Zanganeh, and Quing Zhu, "Interlaced photoacoustic and ultrasound imaging system with real-time co-registration for ovarian tissue characterization", J Biomed Opt.; 19(7):76020(Jul ,2014)

20. Hai Li; Patrick Kumavor; Umar Salman Alqasemi; Quing Zhu, “Utilizing spatial and spectral features of photoacoustic imaging for ovarian cancer detection and diagnosis“, J. Biomed. Opt. 20 (1), 016002 (January 02, 2015).

# Chapter 2 Principles of Ultrasound and Photoacoustic Imaging

The discovery of photoacoustic effect dates back to 1880 by Alexander Graham Bell. However, limited by the techniques, photoacoustic imaging (PAI) was not invented until the advent of ultrasound transducers, computers and lasers. PAT, as an emerging imaging modality, combines excellent optical absorption contrast with ultrasound resolution. Short duration laser pulses with wavelength in near infrared region (NIR) penetrate into tissue samples.[1-11] Photons are either absorbed or scattered in its transportation path. Since human tissues are usually highly scattered medium. Photons can reach up to 5 cm below the surface. The diffusive light is partially absorbed by absorbers inside tissue (natural absorbers or artificial contrast agents) and causes local thermal expansion. The wideband photoacoustic waves propagate in three dimensional (3D) spaces and can be collected by ultrasound transducers for optical absorption reconstruction. Note that the resolution of reconstructed image is determined by ultrasound frequency while the contrast is determined by optical absorption inside tissues. PAT has the unique strength to combine the high contrast of optical imaging with high spatial resolution of ultrasound imaging in the diffusive regime.

This chapter is organized for the introduction of photoacoutic principle, signal processing and reconstruction. Before that, basics about biomedical optics and ultrasound imaging are also reviewed which helps the understanding of design of real time co-registered ultrasound and photoacoustic imaging system in chapter 3.

## 2.1 Tissue Optics

Biological tissues are usually highly scattered and inhomogeneous media. Photons suffer multiple scattering and absorption events before dying out which results in the laser beam broadening and decay. Therefore, the propagation of light in tissue depends on the size, shape and

density, as well as the scattering and absorption properties, of cells, cell organelles and various fiber structures. The main natural absorbers of light in 400-1350 nm are oxygenated-hemoglobin ($HbO_2$), deoxygenated-hemoglobin (Hb) and water. In the range of 700-900 nm (referred as "optical window"), tissue absorption was dominated by $HbO_2$ and Hb and water absorption in this range is much less than hemoglobin. This optical window provides a better penetration depth than other wavelengths. Figure 2.1 shows the absorption coefficients of Hb and $HbO_2$ for the wavelength between 250nm to 1000nm.[12]

The physical meaning of absorption coefficient μa is the probability of absorption event in a medium per unit infinitesimal path length. For a single absorber, the absorption coefficient is given by:

$$\mu_a = \mathrm{N}_a \sigma_a \tag{2.1}$$

, where $N_a$ is the number density of absorbers ($cm^{-3}$) in the medium and $\sigma_a$ is the absorption cross section ($cm^2$).

Light also attenuates along its propagation path. In an absorbing-only medium, the attenuation follows the following equation, where I is the light intensity and x is the infinitesimal distance.

$$\frac{dI}{I} = -\mu_a dx \tag{2.2}$$

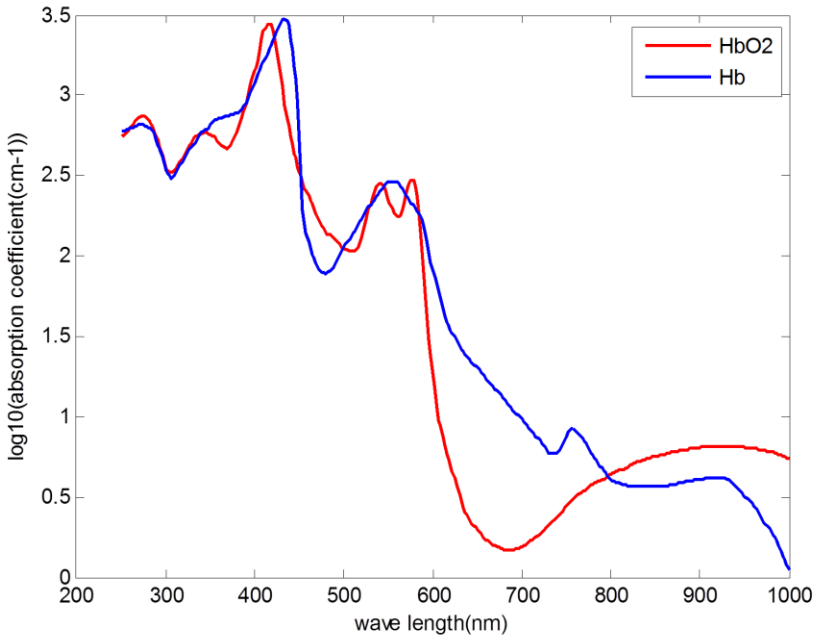


Figure 2.1 Absorption of Hb and HbO2 in blood, assuming 150g/l as hemoglobin concentration and 64500 g/mole as molar weight, data compiled from Reference 12

The solution to equation 2.2 is the famous Beer-Lambert Law:

$$I(x) = I_0 \exp(-\mu_a x) \tag{2.3}$$

, where $I_0$ is the intensity at $x = 0$. The speed of decay is absorption coefficient while the amount of light being absorbed is proportional to the product of $\mu_a$ and the traveled distance $x$.

For a medium with sparsely distributed (where the mean distance between particles is much greater than both the scatter size and the wavelength), scattering events are considered to be independent and involve only one particle. Similar to the definition of absorption coefficients, scattering coefficients $\mu_s$ is the probability of scattering event in a unit of path length. For a single scatter, the scattering cross-section $\sigma_s$ indicates the scattering capability of the particle and $\mu_s$ is determined by the product of $\sigma_s$ and number density $N_s$ of scatters in a medium.

$$\mu_s = N_s \sigma_s \tag{2.4}$$

Photons experience the strongest scattering when both the structure size matches the wavelength and the refractive index mismatches that of the surrounding medium. In general, the overall refractive index of tissue falls within 1.34-1.62, which is greater than that of water (1.33).

For hemoglobin, its absorption coefficient is much larger than its scattering coefficient ( $\mu_a \gg \mu_s$). Extinction coefficient is the summation of both absorption coefficient and scattering coefficient ($\mu_t = \mu_a + \mu_s$). It can be measured by collecting the ballistic transmittance T of a clear medium with similar refractive index as hemoglobin sample using collimated light,

$$T = \frac{I_s}{I_0} \tag{2.5}$$

where $I_s$ is the intensity of light after penetrating sample of thickness d; Combining equation 2.5 with Beer's law, the extinction coefficient is obtained by

$$\mu_t = -\frac{1}{d} \ln T \tag{2.6}$$

Alternatively, extinction coefficient can also be represented by absorbance ($A = -log_{10}T$ ) as following equation:

$$\mu_t = \ln 10 \, \frac{A}{d} \tag{2.7}$$

, where ln10 is about 2.303.

The scattering properties of a medium can be described as a probability density function (PDF) p(s, s') for scattering in the direction s' of a photon traveling in the direction s, characterizing an elementary scattering act. Assuming symmetric scattering relative to the direction of the incident wave, p(s, s') depends only on the scattering angle θ between directions s and s' as p(s, s') = p (θ). Hence assuming random distribution of the scatters in the medium leads to:

$$\int_0^{\pi} p(\theta) 2\pi \sin\theta \, d_\theta = 1 \tag{2.8}$$

In practice, *p (θ)* is approximately by the Henyey-Greenstein phase function:

$$p(\theta) = \frac{1}{4\pi} \frac{1 - g^2}{(1 + g^2 - 2g\cos\theta)^{\frac{3}{2}}} \tag{2.9}$$

, where $g$ is the scattering anisotropy parameter and it is defined as the mean cosine of the scattering angle $\theta$.

$$g \stackrel{\text{def}}{=} < \cos\theta \geq \int_0^{\pi} \cos\theta \, p(\theta) 2\pi \sin(\theta) \, d_\theta \tag{2.10}$$

The value of g varies from -1 to 1: g = 0 corresponds to isotropic scattering, g = 1 to total forward scattering and g = -1 to total backward scattering. For most biological tissues, g is about 0.9. Then the reduced scattering coefficient can be defined as:

$$\mu_s' = (1 - g)\mu_s \tag{2.11}$$

, the reciprocal of which is the average distance travelled by a photon in tissue before losing memory of its initial direction of propagation (the transport mean free path). In the near infrared range, typical values of $\mu_a$ in tissues range from 0.02 $cm^{-1}$ to 0.30 $cm^{-1}$, while $\mu_s'$ ranges from 2 to 20 $cm^{-1}$. It means the transport mean free path is only several millimeters. The transport mean free path is the boundary of ballistic regime and diffusive regime. In ballistic regime, high resolution surface imaging can be achieved by several modalities, such as regular optical microscopy(OM) , scanning near-field optical microscopy(SNOM), confocal microscopy(CM), two photon microscopy (2PM), second harmonic microscopy(SHM). There is a new technique called optical coherence tomography (OCT) allowing to image up to 1~2 mm depth. For photon beyond the transport mean free path, photons behave in the similar way as heat transportation.

Diffuse optical tomography (DOT) allows imaging of up to several centimeters. However, the limitation of DOT is the low resolution achievable. Hybrid imaging modality such as photoacoustic tomography can help to overcome the drawbacks of low penetration depth of pure optical imaging modalities and ballistic imaging modalities while achieve several centimeters detection depth using diffusive photons.

## 2.2 Ultrasound Imaging

Comparing with other clinical imaging modalities, ultrasound imaging is less expensive, which makes it widely used in diagnosis of a number of diseases. Due to its non-invasiveness, safety at low power level, flexibility and relatively good differentiation of soft tissues ultrasound has wide clinical application, both as a primary modality and as an adjunct to other diagnostic procedures.[13]

Compressional waves are those generated by the vibration of particles in the longitudinal direction, which is along the direction of propagation. Shear waves, also known as transverse waves, are produce by transverse motion of the particles. Because tissue has high water content, the simplification that ultrasound waves in the body are like waves propagating in liquids is often made. Hence, shear waves are not considered as fluid waves are of longitudinal type. The particles are displaced from their equilibrium state by a distance $u$ at a rate $v$ as the wave disturbance propagates through the medium. Such changes correspond to a local pressure disturbance $p$. For a propagation direction along the z-axis, the pressure wave equation is given by:

$$\frac{\partial^2 p}{\partial z^2} - \frac{1}{v_s{}^2}\frac{\partial^2 p}{\partial t^2} = 0 \qquad (2.12)$$

, where $v_s$ is the speed of sound in medium (about 1480 m/s in water) which is determined by its density $\rho$ and adiabatic compressibility constant $K$ as

$$v_s = \sqrt{\frac{1}{\rho K}} \tag{2.13}$$

Substitute equation 2.13 to 2.12, we can get wave equation in 3D space.

$$\nabla^2 p - \rho K \frac{\partial^2 p}{\partial t^2} = 0 \tag{2.14}$$

The specific acoustic impedance $Z$ of the medium is given by:

$$Z = \frac{p}{v} = \rho v_s = \sqrt{\frac{\rho}{K}} \tag{2.15}$$

Whenever an ultrasound wave goes from region 1 with certain acoustic impedance into a neighboring region 2 with a different one, a portion of the incident power is reflected at the boundary and the rest continues probing deeper interfaces. The angles of the reflected and transmitted waves can be calculated by Snell's law by:

$$\frac{sin\,\theta_i}{sin\,\theta_t} = \frac{v_{s1}}{v_{s2}} \tag{2.16}$$

And the reflection coefficient for the interface is given by:

$$R = \frac{p_r}{p_i} = \frac{\left(\frac{Z_2}{\cos\theta_t}\right) - \left(\frac{Z_1}{\cos\theta_i}\right)}{\left(\frac{Z_2}{\cos\theta_t}\right) + \left(\frac{Z_1}{\cos\theta_i}\right)} \tag{2.17}$$

As ultrasound propagates in tissue, its intensity will be attenuated due to tissue absorption and scattering. The attenuation is directly proportional to its frequency. The attenuation for most soft human tissue is between 1.35 and 1.68 $dB.cm^{-1}.MHz^{-1}$, while the value for bone is 3 to 10 $dB.cm^{-1}.MHz^{-1}$. For water, on the other hand, it is 0.002 $dB.cm^{-1}.MHz^{-1}$.[14] Hence, medical instrumentation typically only uses frequencies from 1 to 10MHz to accommodate for both high resolution and deep penetration.

The majority of diagnostic ultrasound imaging is performed in pulse-echo (PE) mode. In this mode, an ultrasound transducer generates acoustic pulses that propagate through human body. When the pulses reach mechanical inhomogeneities, a part of them is reflected back to the transducer. The pulse echo from a reflector at distance $z$ from the transducer arrives at $t = 2z / v_s$.

### 2.2.1 Ultrasound Transducer and Array

Ultrasound transducer is usually made of piezoelectric composite material which convert electrical signal into acoustic waves and vise versa. The fundamental resonance frequency of an ultrasound transducer is given by its thickness d and the speed of sound in the material by $f_0 = v_s / 2d$. The emitted acoustic pressure field is a function of the transducer aperture shape. For a rectangular aperture of b by h dimension in x and y respectively, the resultant beam profile in the far field is given by the following directional factor:

$$H(x, y, z) = sinc\left(\frac{bx}{\lambda z}\right) sinc\left(\frac{hy}{\lambda z}\right) \tag{2.18}$$

where $sinc(x) = sin(\pi x)/(\pi x)$ and $\lambda$ is the wavelength. Substituting $x/z = sin\varphi_x$ and $y/z = sin\varphi_y$ ,and plotting $H(\varphi_x, \varphi_y)$, we can get the shape of far field pattern in Figure 2.2 with the assumption that $h > b$. The directionality of the beam is given by

$$\phi_{xd} = \sin^{-1}\frac{\lambda}{b}, \phi_{yd} = \sin^{-1}\frac{\lambda}{h} \tag{2.19}$$

， which corresponds to the angular position of the first zero of the beam.

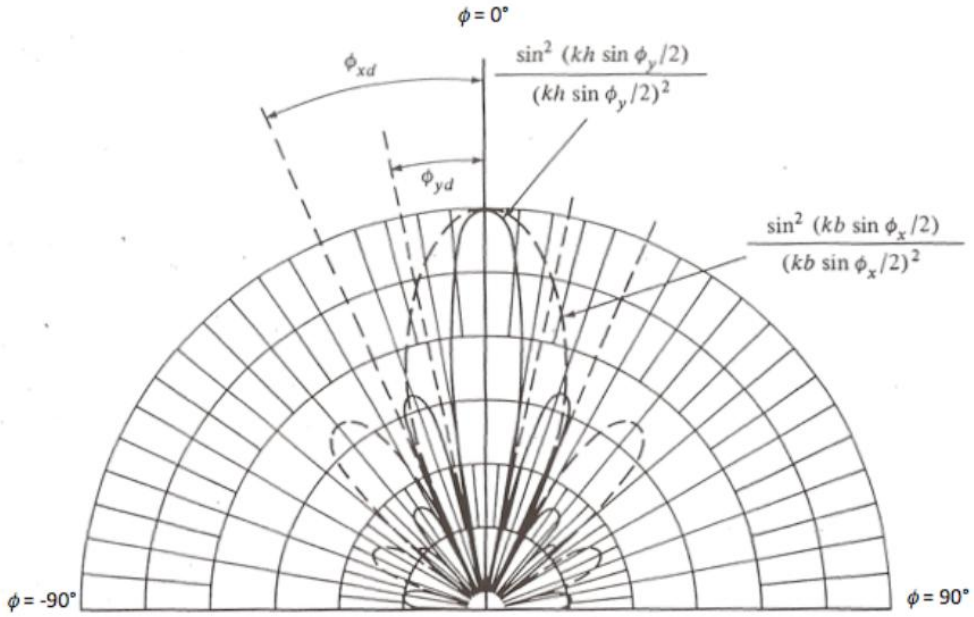


Figure 2.2 Far-field beam profile for a rectangular aperture of size b by h where b < h. The dash line corresponds to the observed pattern in x direction and the solid line to the pattern observed in y direction (Adapted from Reference 15).

The majority of the power is contained in the central (main) lobe of the pattern between the first zeros on either side of the central lobe. However, some power is also found in the side lobes neighboring the main lobe. It is important to note that the width of the main lobe increases linearly with z in the far-field region. In an effort to modify the profiles shown in Figure 2.2 an acoustic lens or direct shaping of the transducer is used to obtain optimum resolution at a single depth plane and its vicinity.

Ultrasound transducers are usually an assembly of multiple single elements. Elements are usually arranged as linear array or curvilinear array. Physically, the separation of the elements in linear arrays is greater than that of phase arrays, which makes phase arrays smaller than linear ones. Depending on the desired scanning mode (linear scan or sector scan), an array can work in linear array mode or phase array mode. In linear scan mode, sub-set of the array elements are used to form one scan line (beam) of the image which is normal to the surface of the transducer.

In sector scan mode, all of the elements are used to form the beam of certain direction and beam direction can be steered by dynamically change the focus points. Fan shape of scan lines are reformed into rectangular image via scan conversion (interpolation). In pulse echo mode, focusing are done in both transmission and receiving procedure. The calculation of delays for the beamforming of transvaginal probe needs to take the radius of probe into consideration.

When a number of elements in a transducer array are excited simultaneously and coherently, the effective aperture width $L_x$ is bigger than that of a single element $D_x$. The far-field divergence is much narrower. Due to the segmentation of the aperture, replica of the main beam, known as grating lobs, appear at $\phi_{gn}$ given by

$$\phi_{gn} = \sin^{-1}(\frac{n\lambda}{s}), n = \pm 1, \pm 2, \ldots \quad (2.20)$$

, where s is the separating distance between elements ( or pitch). It is important to note that as the pitch increase respect to the wavelength, grating lobes get closer to the main beam and increase in number.

### 2.2.2 Ultrasound Beamforming for PE Mode

In PE mode, there are two types of focusing: transmission focusing and receiving focusing. Take sector scan of phase array as an example, and we set the center of the array as origin of coordinate. Elements of the linear array are arranged alone y axis shown in Figure 2.3. For certain scan line (beam) in direction $\theta_i$ in the scan range from $\theta_{min}$ to $\theta_{max}$ with an interval of $(\theta_{max} - \theta_{min}) / (M - 1)$, where $M$ is the total scan lines in the scan range, we have

$$\theta_i = \frac{i * (\theta_{max} - \theta_{min})}{(M - 1)} + \theta_{min} \quad (2.21)$$

where $i$ is the index of scan line, starting from 0 to M-1. Assuming the focus distance is set as f, then the focus point coordinates are

$$x_f = f * \cos(\theta_i), y_f = f * \sin(\theta_i) \tag{2.22}$$

Usually the number of element in the phase array N is a power of 2, such as 128, 256. The coordinates of *ith* element are:

$$x_i = 0, y_i = \left(i - \frac{(N-1)}{2}\right) * s \tag{2.23}$$

where s is the pitch between two adjacent elements. Then the distance between each element and transmission focus $d_i$ can be calculated, from which the maximum distance $d_{max}$ can be found. The element corresponding to $d_{max}$ should transmit at first. So the delay for the transmission focusing of *ith* element can be calculated using the following formula:

$$delay(i) = (d_{max} - d_i) * \frac{f_t}{v_s} \tag{2.24}$$

where $f_t$ is the transmission frequency in *MHz* used by transmission circuit (e.g. FPGA), $V_s$ is the velocity of sound in water in $mm/\mu s$.

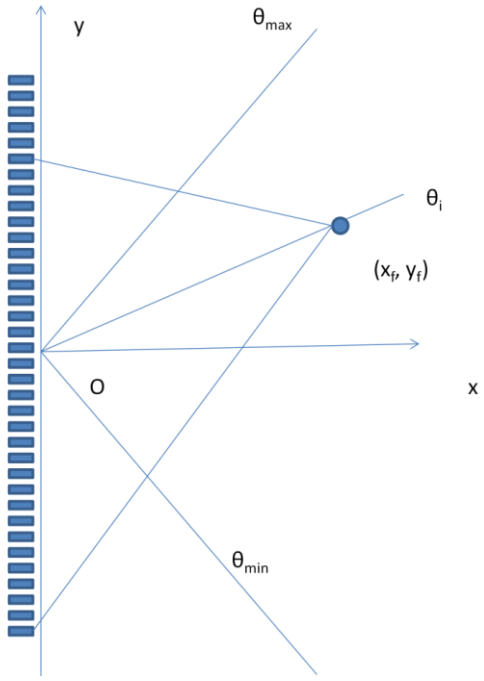


Figure 2.3 Illustration of transmission focusing in PE mode

Assuming there is a virtual element at the origin O, and then this virtual element (used as reference in receiving focusing delay calculation) will start pulsing at time point

$$T_0 = \frac{d_{max} - f}{v_s} \tag{2.25}$$

At time point $T_1 = d_{max} / V_s$, the emitted pulses from all elements arrive at focal point f, which serves as a point source for later wave propagation.

For any receiving focal point with a distance *fr* along the transmitting direction (beam direction) to origin O, its coordinates can be calculated in the similar way as equation 2.22. Assume there is an reflector at distance of *fr*, then the wave propagating from the transmission focal point *f* will arrive it at $T2 = T1 + (fr - f) / V_s$, the reflected waves can be viewed as another point source at *fr*. These reflected waves arrive at each element at different time points. The distance between each element $e_i$ and receiving focus *fr* , *dri*, can be calculated using their coordinates. Then the receiving wave arrives at:

$$TR_i = T2 + dr_i/v_s \tag{2.26}$$

The whole time flow is shown in Figure 2.4 and the delay of each element for beamforming can be calculated using equation 2.26 or equivalently using a simplified equation in the following:

$$delay(i) = \left(T_0 + \frac{2f_r}{v_s} + \frac{dr_i - f_r}{v_s}\right) * f_s \tag{2.27}$$

Note that equation 2.27 is for any receiving focus *j* in the beam, so it can be generalized;

$$delay(i,j) = \left(T_0 + \frac{2f_{rj}}{v_s} + \frac{dr_{ij} - f_{rj}}{v_s}\right) * f_s \tag{2.28}$$

where index *i* is for *ith* element, index *j* is for *jth* receiving focal point, $f_{rj}$ is the distance of *jth* receiving focal point from origin, $dr_{ij}$ is the distance of element *i* to focal point *j* . Then first term

in equation 2.28 is calculated when transmission delay calculation is conducted and the second term times $f_s$ is equal to index $j$, because $f_{rj} = \frac{j}{2fs} * vs$.

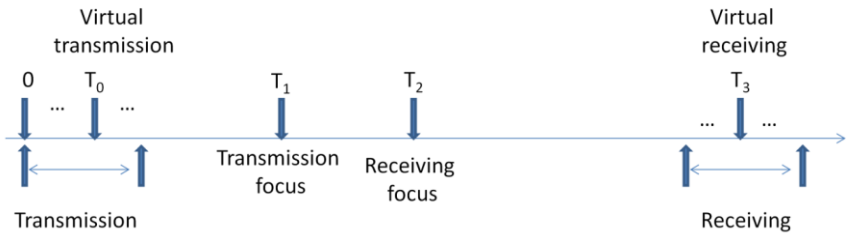


Figure 2.4 Time flow of PE mode beamforming. At time zero, the farthest element begins to transmit. At $T_0$, virtual element begins to transmit. At T1, waves from all elements focus and at T2, the waves from transmission focus reach receiving focus (reflector). The reflected waves arrive at each element at different time point. Note that T3 – T2 = T2 – T0 = $f_r/v_s$.

The transmission and receiving is more clearly demonstrated in the flowing chart, Figure 2.5 (a) and (b). The output of beamforming is the summation of the delayed signal from each element, where delay relies on the transmission focus, steering angle and sample frequency. Note that in PE mode, we need to steer the beam direction for every single beam. That means we need to repeat the previous calculation M times, where M is the number of beams. Given certain scan range from $\theta_{min}$ to $\theta_{max,}$ these transmission and receiving delays (coefficients) can be pre-calculated and stored in memory as a look-up table. This loop-up table method can promote the imaging speed by removing redundant coefficients calculation.

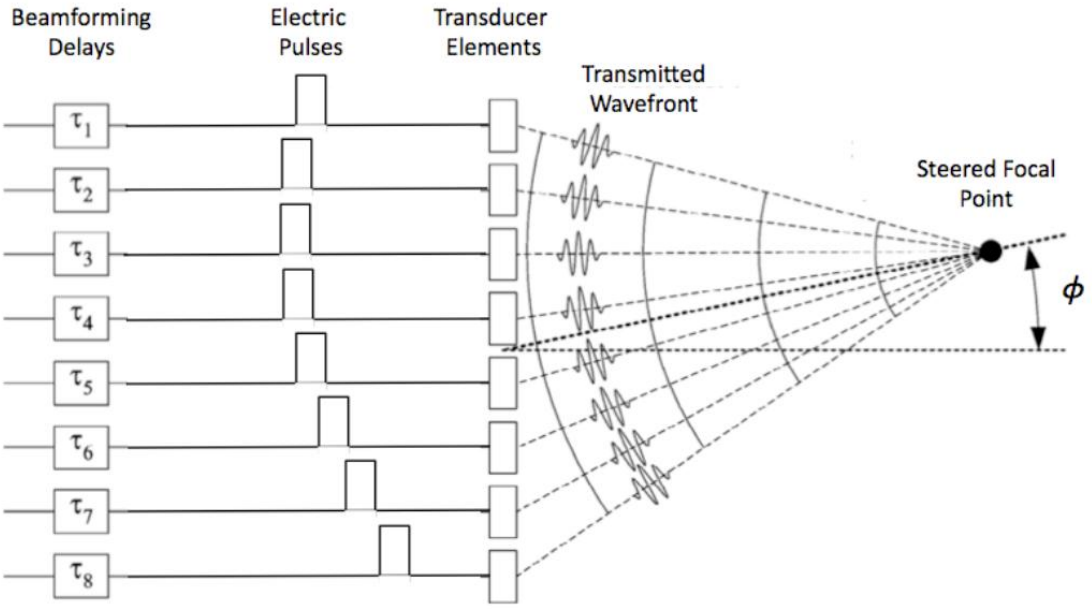


Figure 2.5(a) Transmission focusing and steering in PE mode (Adapted from Reference 16)

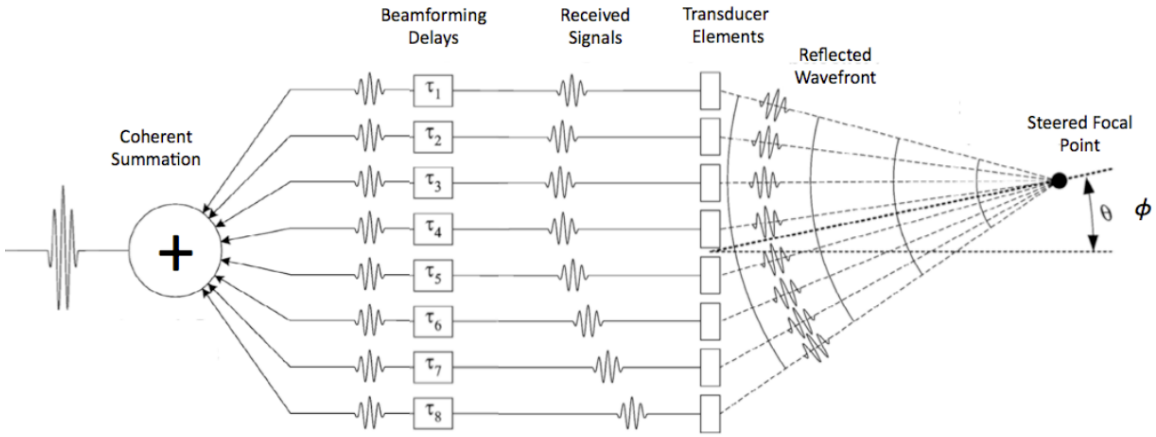


Figure 2.5 (b) Receiving beamforming of PE mode (Adapted from Reference 16).

## 2.3 Photoacoustic Generation and Reconstruction[8]

### 2.3.1 Photoacoustic Wave Generation

The motivation for photoacoustic imaging is to achieve high-resolution imaging of optical contrast deep in the quasi-diffusive or diffusive regime. This is achieved by ultrasonic detection of photoacoustic waves, which are generated by absorption of light from a pulsed laser.

The fractional volume expansion *dV/V* due to laser excitation is given by

$$\frac{dV}{V} = -\kappa p + \beta T \tag{2.29}$$

, where $\kappa$ is the isothermal compressibility, $\beta$ is the thermal coefficient of volume expansion and, $p$ and $T$ represent the pressure and temperature changes respectively. For the generation of photoacoustic waves, there are two time constraints in terms of laser pulses. Thermal relaxation time $\tau_{th}$ is the time constraints required for the temperature rise in the illuminated region of tissue to drop by a factor of $e^{-1}$ while stress relaxation time $\tau_s$ is the time constraint required for pressure rise to drop by $e^{-1}$. When the laser pulse width is much shorter than $\tau_{th}$ and $\tau_s$ , the fractional volume expansion is negligible and the local pressure rise immediately after the laser excitation pulse can be derived from wave equation 2.12 as:

$$p_0 = \frac{\beta}{\kappa \rho C_V} \eta_{th} A_e \tag{2.30}$$

, where $C_V$ denotes the specific heat capacity at constant pressure, $A_e$ is the specific optical absorption and $\eta_{th}$ is the percentage of laser energy that is converted to heat.

Optical absorption is the product of the absorption coefficient $\mu_a$ by the optical fluence $F$. Then, given the he heat capacity at constant pressure $C_P$, the Grueneisen parameter can be defined as:

$$\Gamma = \frac{\beta v_s^2}{C_p} \tag{2.31}$$

, and then the initial pressure $p_0$ can be expressed as

$$p_0 = \Gamma \eta_{th} \mu_a F \tag{2.32}$$

.The general photoacoustic equation can be derived as

$$(\nabla^2 - \frac{1}{v_s^2}\frac{\partial^2}{\partial t^2})p(\vec{r},t) = -\frac{\Gamma}{v_s^2}\frac{\partial H(\vec{r},t)}{\partial t} \tag{2.33}$$

$$H(\vec{r},t) = \eta_{th}\mu_a F(\vec{r},t) \tag{2.34}$$

the left hand of equation 2.33 is same as left hand side of wave equation 2.12 and the right hand side is the source term of wave equation. Note that this source term only depends on the first time derivative of optical absorption. Hence, only time variant illumination produces pressure waves. Then for a pulsed laser source of high peak power but very low duty cycle (~10 ns), which satisfies the thermal and stress confinement condition in biological tissue, the heating function can be expressed as $H(\vec{r},t) = \eta_{th}\mu_a H(\vec{r})\delta(t)$ and equation 2.33 is reformed as

$$(\nabla^2 - \frac{1}{v_s^2}\frac{\partial^2}{\partial t^2})p(\vec{r},t) = -\frac{p_0(\vec{r})}{v_s^2}\frac{d\delta(t)}{dt} \tag{2.35}$$

Using a Green function approach the forward solution for the photoacoustic wave equation can be obtained:

$$p(\vec{r},t) = \frac{1}{4\pi v_s^2}\frac{\partial}{\partial x}\left[\frac{1}{v_s}\int d\vec{r}'\, p(\vec{r}')\delta(t - \frac{|\vec{r} - \vec{r}'|}{v_s})\right] \tag{2.36}$$

This equation implies that the detected pressure at spatial location $\vec{r}$ and time t comes from sources over a spherical shell centered at $\vec{r}$ with a radius of $V_s t$, as shown in Figure 2.6.

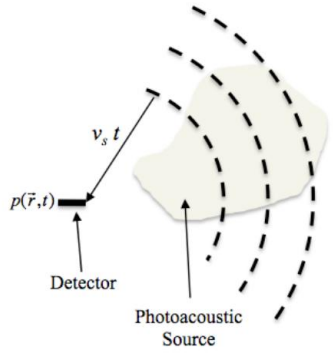


Figure 2.6 The photoacoustic waves detected by a point detector at a certain time t come from sources over a spherical shell centered at the detector position and a radius of $V_s t$ (Adapted from Reference 6).

### 2.3.2 Photoacoustic Reconstruction

There are several reconstruction algorithm developed to determine the absorption profile $A_e(\vec{r})$, such as delay-and-sum[3], Fourier-based method[17] and the precise back-projection method[5, 18]. The precise analytical solution of reconstruction problem is provided by the back-projection method in Reference 18. In this back-projection algorithm, the optical absorption profile for a location $\vec{r}$ in the imaging domain can be derived from measurements of the pressure on the surface $S_0$ using

$$A_e(\vec{r}) = \frac{2}{\Gamma(\vec{r})} \int_{\Omega_0} b\left(\overrightarrow{r_0}, t = \frac{|\vec{r} - \vec{r}'|}{v_s}\right) \frac{d\Omega_0}{\Omega_0} \tag{2.37}$$

$$b(\overrightarrow{r_0}, t) = p(\overrightarrow{r_0}, t) - t\frac{\partial p(\overrightarrow{r_0}, t)}{\partial t} \tag{2.38}$$

, where $\Omega_0$ represents the solid angle subtended by the measurement aperture and $b(\overrightarrow{r_0}, t)$ is the back-projection kernel. The factor $\frac{d\Omega_0}{\Omega_0}$ is the weight of signal from an element $dS_0$. Figure 2.7 is adapted from Reference 18 for the understanding of equation 2.37.

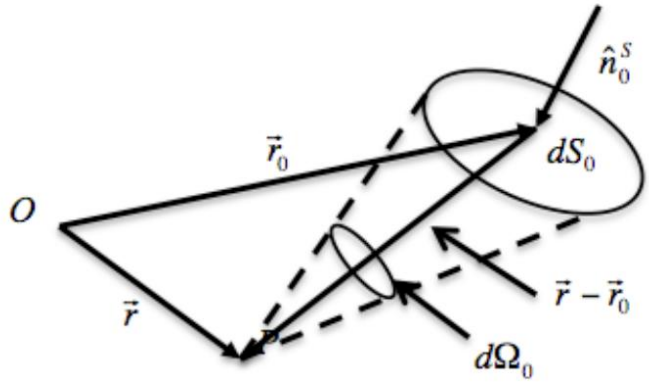


Figure 2.7 Reference diagram for the back-projection algorithm (Adapted from Reference 18).

This back-projection algorithm requires a closed measurement, which means a spherical measurement for 3D reconstruction and ring shape measurement for 2D reconstruction. It can be done by rotating single element or array based transducer around target.[4.5, 19-21] However, in clinical application, this tomographic configure is hard to implement, especially for ovary cancer detection because of limited measure aperture. Instead of precise back-projection algorithm, delay and sum algorithm is preferred. Because of the limited angle for receiving wave of an array, the reconstructed image is generally poorer than tomographic system. The advantage of array-based system and delay-and-sum algorithm is that it can be easily adapted conventional pulse-echo commercial system to provide co-registered ultrasound and photoacoustic images.

Actually, delay and sum algorithm can be viewed as a simplified back-projection algorithm if we equalize the weight $\frac{d\Omega_0}{\Omega_0}$ of each element and ignore the derivative term in equation 2.38. The only thing needed in delay-and sum algorithm is the correct delay to form each beam, which can be pre-calculated as look-up table for accelerating imaging reconstruction. These features of delay-and-sum algorithm make it easy to implement in a distributed computation environment, such FPGA or GPU. In this study, we just collect raw data and perform beamforming for PAT mode on PC side, because we need raw data for later advanced processing and diagnosis.

After beamforming, PAT following the same way as PE mode in terms of signal processing; it will be discussed in details in next chapter. At first, beam envelope is detected by Hilbert transform or base-band demodulation (Inphase-Quadrature demodulation). Then rectangular absorption map is obtained by interpolating envelopes of sector shape into the rectangular pixel locations.[22]If necessary, a logarithmic compression is conducted on the interpolated envelope and mapped to the normal integer pixel range. Note that, when co-registered mode is used, PAT image can't use the same color map of PE. In this work, we divide

the 256 color map terms into two halves, 0 to 127 are used for gray scale (dark to white) and 128 to 255 are the mapped from red(255, 0, 0) to yellow(255, 255, 0), in which only green term changes. In the co-registered image, PAT pixel will overwrite the PE pixel, if the corresponding interpolated envelope is greater than the threshold set by dynamic range or estimated system noise threshold from regions without photoacoustic signals.

# References


1. V.G. Andreev, A.A. Karabutov, S.V. Solomatin, E.V. Savateeva, V. Aleinikov, Y.V. Zhulina, R.D. Fleming and A. Oraevsky, "Optoacoustic tomography of breast cancer with arc-array transducer," Biomedical Optoacoustics 3916, 36-47 (2000).

2. G.J. Diebold, A.C. Beveridge and T.J. Hamilton, "The photoacoustic effect generated by an incompressible sphere," The Journal of the Acoustical Society of America (2002).

3. C.G. Hoelen and F.F. de Mul, "Image reconstruction for photoacoustic scanning of tissue structures," Applied optics 39(31), 5872-5883 (2000).

4. R.A. Kruger, W.L. Kiser, D.R. Reinecke, G.A. Kruger and K.D. Miller, "Thermoacoustic molecular imaging of small animals," Molecular imaging : official journal of the Society for Molecular Imaging 2(2), 113-123 (2003).

5. R.A. Kruger, P. Liu, Y.R. Fang and C.R. Appledorn, "Photoacoustic ultrasound (PAUS)--reconstruction tomography," Medical physics 22(10), 1605-1609 (1995).

6. C. Li and L.V. Wang, "Photoacoustic tomography and sensing in biomedicine," Physics in Medicine and Biology 54(19), R59-R97 (2009).

7. A. Oraevsky and A.A. Karabutov, "Ultimate sensitivity of time-resolved optoacoustic detection," Biomedical Optoacoustics 3916, 228-239 (2000).

8. L.V. Wang and H. Wu, Biomedical Optics: Principles and Imaging, John Wiley & Sons, Inc, Hoboken, NJ, (2007).

9. L.V. Wang, "Photoacoustic Imaging and Spectroscopy," 488 (2009).

10. X. Wang, Y. Pang, G. Ku, X. Xie, G. Stoica and L. Wang, "Noninvasive laser induced

photoacoustic tomography for structural and functional in vivo imaging of the brain," Nat Biotechnol 21(7), 803-806 (2003).

11. M. Xu and L. Wang, "Photoacoustic imaging in biomedicine," Rev Sci Instrum 77(4), 041101 (2006).

12. "http://omlc.ogi.edu/spectra/hemoglobin/index.html," (2010).

13. P.N. Wells, "Current status and future technical advances of ultrasonic imaging," IEEE Eng Med Biol Mag 19(5), 14-20 (2000).

14. A. Macovski, Medical Imaging Systems, Prentice-Hall, Inc, Englewood Cliffs, NJ, (1983).

15. D. A. Christensen, "Ultrasonic bioinstrumentation," 235 (1988).

16. J.A. Johnson, M. Karaman and B.T. Khuri-Yakub, "Coherent-array imaging using phased subarrays. Part I: basic principles," Ultrasonics, Ferroelectrics and Frequency Control, IEEE Transactions on 52(1), 37 - 50 (2005).

17. K.P. Köstli and P.C. Beard, "Two-dimensional photoacoustic imaging by use of Fourier-transform image reconstruction and a detector with an anisotropic response," Applied optics 42(10), 1899-1908 (2003).

18. M. Xu and L. Wang, "Universal back-projection algorithm for photoacoustic computed tomography," Physical review E, Statistical, nonlinear, and soft matter physics 71(1 Pt 2), 016706 (2005).

19 J. Gamelin, A. Aguirre, A. Maurudis, F. Huang, D. Castillo, L. Wang and Q. Zhu, "Curved array photoacoustic tomographic system for small animal imaging," Journal of biomedical optics 13(2), 024007 (2008).

20 J. Gamelin, A. Maurudis, A. Aguirre, F. Huang, P. Guo, L. Wang and Q. Zhu, "A real-time photoacoustic tomography system for small animals," Optics Express 17(13), 10489-10498 (2009).

21 K. Mehta, R. Lacewell, P.M. Henrichs and A.A. Oraevsky, "128-channel laser optoacoustic imaging system (LOIS-128) for breast cancer diagnostics," Proceedings of SPIE (2006).

22. Ultrasound Scan Conversion on TI's C64x+ DSPs,

http://www.ti.com/lit/an/sprab32/sprab32.pdf

# Chapter 3 Design and Implement of Real-time Co-registered Ultrasound and Photoacoustic Imaging System for Ovarian Cancer Detection

Photoacoustic imaging emerges as a promising imaging modality for deep tissue absorption imaging. It combines the high contrast of optical imaging and high resolution of ultrasound imaging. Meanwhile it has reasonable penetration depth if NIR light is used. However, as stated in chapter 2, for clinical cases, tomographic configuration is not applicable. Instead, we use array-based transducer and reconstruct light absorption based on limited receiving aperture using delay-and-sum algorithm.

To achieve the real-time imaging of ovary, several optimization methods are used in the design phase, including hardware and software acceleration. Each element of transducer has its own independent analog amplification circuit and Analog-to-Digital converter (ADC). Multiple FPGAs work in parallel to perform data acquisition and sub-beamforming using the delays pre-calculated in PC side. PAT raw data and PE beams are transferred to PC RAM for further processing via Ethernet cable or PCIe bus. PC side performs envelop detection, scan conversion, logarithmic compression and display. GUI for user interactive activities are also designed where envelope detection method, dynamic range and mask of artifact can be freely set by users.

## 3.1 Introduction

As we discussed in chapter 2, PAT has high ultrasound resolution while keeps high optical contrast. Optical absorption of biological tissue in the near-infrared region (NIR) is directly related to its blood hemoglobin content, which is the summation of oxygenated and deoxygenated hemoglobin concentrations. Abnormal growth of tumor cells requires a greater supply of nutrients and oxygen than normal tissue, which triggers rapid growth of a complex blood vessel network or tumor angiogenesis. Tumor angiogenesis is a functional marker of tumor

progression and metastasis. Thus, PAT is an excellent tool to image tumor angiogenesis development as well as tumor oxygenation when multiple optical wavelengths are utilized. The penetration depth of PAT is scalable with the central frequency and bandwidth of the ultrasound transducer as long as adequate light fluence can be delivered to the targets.[1] However, PAT images do not show optically non-absorbing structures of the tissue, which makes it difficult to correlate the absorption contrast with anatomical structures. Ultrasound, on the other hand, provides excellent anatomical structure information related to tissue acoustic impedance but lacks functional contrast in diagnosing early stage cancers [2]. Combining the two modalities is a logical extension of each modality alone because both use the same ultrasound detection front end circuits, and, more importantly, the combined modality provides complimentary information of tumor vasculature and tumor morphology, which are valuable for cancer detection and diagnosis as well as detection and diagnosis of other diseases [3-7]. Furthermore, the structural information provided by ultrasound imaging can be employed to improve the PAT image quality by incorporating more accurate models for acoustic propagation in PAT reconstruction .[8-10]

The first system of combined ultrasound and photoacoustic imaging was implemented by Niederhauser et al. in 2005 for vascular imaging; they reported the ability to alternately acquire and display the dual modality images side by side but not in a real-time interlaced scheme [11]. Another combined system for intravascular imaging was introduced by Sethuraman et al. in 2006, however, the data processing for co-registering the two modality images was done off-line [12]. Our group developed a co-registered ultrasound and photoacoustic 3-D imager in 2007, but the data acquisition speed was very low [6, 13]. In 2008, Kolkman et al. modified a commercial ultrasound unit to perform combined ultrasound and photoacoustic imaging; however, because they used the same commercial frontend of hardware-based delay-and-sum beamformer, it required a high laser pulse repetition rate (PRR) of 1 kHz, which made the laser radiation exceed the maximum permitted exposure (MPE) by the International Electrotechnical Commission (IEC). Moreover,

they obtained good frame rate in each modality alone, but the co-registration is not done in a real-time interlaced scheme [14]. Ermilov et al., developed two laser optoacoustic imaging systems in 2009; one of them could work in both optoacoustic and ultra-sound modes. However, this system required switching between optoacoustic and ultrasound data acquisition from a separate optoacoustic machine and a commercial ultrasound scanner, and real-time co-registration of the two images wasn't achieved[15]. Harrison et al. developed a real-time combined ultrasound and photoacoustic microscopy system in 2009 that interlaced the ultrasound and laser pulses for co-registered imaging. The system used a single mechanically scanned high-frequency ultrasound transducer with a unique light delivery probe to scan thin tissue samples[16].

In our design, FPGAs are used for front end data acquisition, control and sub-beamforming for PE mode. The whole system is based on modular design. Our transvaginal probe is a curvilinear probe with 6MHz center frequency and 80% bandwidth. The total 128 elements are arranged evenly on the arc with 8mm radius. The whole angular range covered by the 128 elements is 2.5568 radians. We assign independent analog front end circuit and ADC for each element and sample photoacoustic waves at 40MHz. In PE mode, the transmission frequency is set to be 100MHz. High voltage transformer is used for the pulse generation of PE mode, whose time sequences are controlled by module FPGAs.

For the data communication of FPGAs to PC, in our first version of PAT system, a DSP chip acts as data coordinator. In our improved design, DSP is replaced by an advanced FPGA with PCIe bus which allows us to reach data rate up to 2.5 Gbit/s. The PCIe bus allows DMA data transfer and lead to a reform in term of software structure. Multi-thread technique is implemented to accelerate data processing which almost doubles the frame rate comparing with single thread program.

## 3.2 DSP-based Ultrasound/Photoacoustic System [17]

This is our first version of real-time co-registered ultrasound/photoacoustic system. It is based on FPGA-DSP-PC structure designed for 64 elements array DAQ and data processing. The front end analog circuits include high voltage pulse generator for PE mode, Transmission/Receiving switch (T/R switch), filtering circuit and amplification circuit.[17] The overall block diagram of the system is shown in Figure 3.1. The system has a modular design that allows the number of channels to be easily upgraded as required in multiples of 16 channels. In this DSP-based system, there are only four 16-channels modules to fit a total of 64 element array configuration. Each module consists of five boards grouped together: a customized E-shaped board for 16-channel ultrasound transmission and reception (pre-amplification), and two commercial ultrasound 8-channel receiving boards connected through a customized adaptor board to a commercial FPGA digital data-capturing board (HSC-ADC-EVALCZ). The commercial ultrasound receiving boards contain a microchip (AD9272-65EBZ, Analog Devices Inc., Norwood, MA)[18], which has a programmable octal low-noise amplifier (LNA), variable gain amplifier (VGA), anti-aliasing filter (AAF), and analog- to-digital converter (ADC) with 40 MHz sampling frequency. The FPGA board contains a Virtex-4 Xilinx FPGA (Xilinx Inc., San Jose, CA), and a USB interface that allows interfacing with the receiving boards' microchips through a serial programming interface (SPI) link that controls the characteristics of the chip (gain, bandwidth, etc.). Users are allowed to configure the microchip for its gain, bandwidth to adapt to different types of transducer array (different center frequency, bandwidth, and different illumination condition). For example, for our 6MHz, 80%bandwidth transvaginal probe, the usual configuration is that: front end gain is set to be 15dB, variable gain amplification (VGA) gain is set to be 30 dB, low pass filter cutoff frequency is $flp = Fs/4.5 = 40/4.5 = 8.89$MHz,and high pass filter cutoff frequency is $flp/3.1 = 2.86$MHz. Also, the FPGA captures the octal low-voltage

differential signals (LVDS) of double data rate (DDR) transferring at 240 MHz from each receiving board. The block diagram of the 16-channel module is shown in Figure 3.3 [19, 20].

The modules are plugged into a motherboard that fans out the channels from all the modules to the ultrasound connector. The motherboard also serves as a common power supply and ground plane to all the modules. Each module is also connected through three ribbon cable assemblies to another adaptor board to allow a digital signal processor (DSP) board (TMS320C6455 DSK Module, Spectrum Digital Inc., Stafford, TX) to communicate back and forth with all the modules' FPGAs. Hence, the DSP board serves as a central coordinator between the modules, and it performs the necessary communication with the personal computer and user interface.

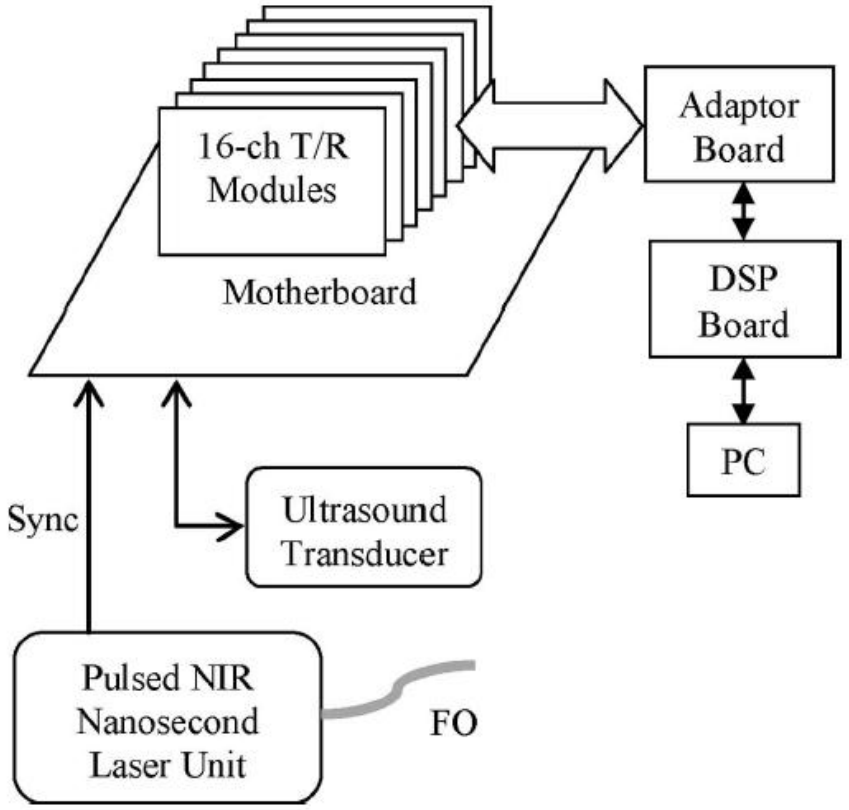


Figure 3.1 The overall block diagram of co-registered imaging system[17].

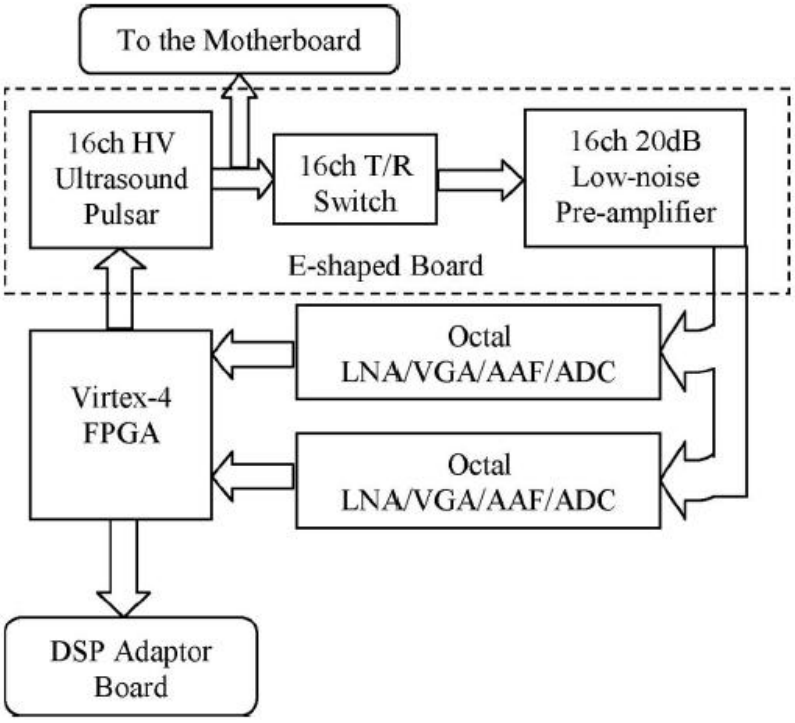


Figure 3.2 The block diagram of one 16-channel module[17].

### 3.2.1 Work Flow of PE/PAT DAQ

As we discuss in chapter 2, all the necessary PE transmission delay coefficients, PE/PAT beamforming coefficient and scan conversion coefficients are pre-calculated in PC software based on user's imaging parameters setting (PE or PAT or both, sector or linear or quasilinear scan, PE focus distance). After that, the PE delay coefficients are downloaded to the DSP board, which distributes them to the FPGAs of each module based on their attached channel order. These delays are the starting time of transmission. Module FPGAs use them to form a timing FIFO for transmission pulse generation. PE beamforming is done in two steps. At first, PE sub beamforming is done simultaneously in module FPGAs from its local 16 channel RF data to reduce the amount of data to be transferred to DSP chip. Then the sub-beamformed data from each module FPGAs are summed at DSP chip and transferred to PC via TCP/IP protocol. Note that the number of PA acquisition can be configured to enable averaging of PA signal for signal

to noise ratio (SNR) improvement. The beamforming of PAT mode is not done in module FPGAs. Instead PAT RF data are directly transferred to PC for processing and storage.

PC software controls the timing of DAQ and processing. After processing the previous data, it asks DSP to perform DAQ by providing necessary information, such as imaging mode. DSP uses its own memory to form a timing FIFO from PE delay coefficients and then transfer the timing FIFO to FPGAs by iterating through the entire scan line index. Once the delay coefficients are transferred to the FPGAs, the DSP triggers all of the module FPGAs to enable the transmission (Tx) FIFOs, and simultaneously starts filling the US receiving (Rx) FIFOs for acquiring PE A-lines until all the A-lines for forming an image frame are acquired. After PE DAQ is done, it waits for the synchronization pulse from the laser to start filling the Rx FIFOs again until the required imaging depth is covered, and this process is repeated for N averaging times while the RF data of the channels are transferred instantly to the DSP and accumulated. The whole DAQ follows a sequential manner. Once the DSP receives all of the PE and PA data, the whole data set for an image frame (both PE and PAT) will be transferred to the PC using a local area network (LAN) interface. Next, the PC will do PAT beamforming, PAT and PE envelope detection, and PE/PAT scan conversion. Finally, the dual-modality images will be co-registered and displayed in a single frame with different color scales.

Thus, the FPGA serves as a 16-channel processing unit that controls transmission, data acquisition from the receiving boards' ADCs, interfacing with the laser unit, preprocessing of the RF data, and 16-channel dynamic focusing of pulse-echo A-lines. Therefore, it is important that the FPGA code is properly designed to be reconfigurable to re-optimize the speed and usage of the available resources in each imaging mode.

### 3.2.2 FPGA Code Structure

A. Block gram

The overall block diagram of the FPGA code written in Verilog HDL is shown in Figure 3.4. It consists of a 16-channel LVDS DDR capture code that converts the ADC 240-MHz serial outputs to single-ended parallel outputs at 40 MHz (i.e., the sampling frequency). The RF data are preprocessed and then stored in a dual-port RAM block. The master controller manages the overall flow of the data and provides the reconfigurability of the code, which is eventually controlled by a few DSP control signals. The LVDS DDR ADC outputs are decoded to parallel single-ended outputs at 40 MHz. After that, the data stream is preprocessed and stored in the Rx FIFO/RAM when the appropriate control signals are received from the master controller. The master controller makes its decisions based on the laser synchronization and DSP control signals to control the Rx and Tx FIFOs, to enable/disable beamforming, and to change the DSP EMIF structure and memory size for reading and writing. The function of the main blocks is summarized in the remainder of this section.

B Preprocessing and Rx FIFO Storage

The RF data are preprocessed immediately before being stored in the dual I/O RAM blocks. The preprocessing includes digital filtering and bias cancellation. The dual port RAM block used for storage is RAMB16, which has 2 kB of memory if used as a dual-port RAM block. Several RAMB16 blocks are lumped together to form a RAM with more storage memory. The outputs from the ADCs are 12-bit quantized; and the length of each Rx FIFO is 4096; which corresponds to a depth of penetration (dp) calculated as dp = 4096 × (0.15 cm/μs) / 40 MHz = 15.36 cm, where the speed of sound is assumed to be 0.15 cm/μs. Note that this is for one-way travel of the ultrasound wave; however, for PE, 4096 FIFO length corresponds to half that distance, which is 7.68 cm. On the other hand, to form a co-registered frame, it's necessary that both images from PAT and PE have the same depth. Thus, for PAT, only the first 2048 values of

the FIFOs are considered, whereas all 4096 of the values are considered for PE. The Rx FIFO/RAM used for that purpose is shown in Figure 3.5.

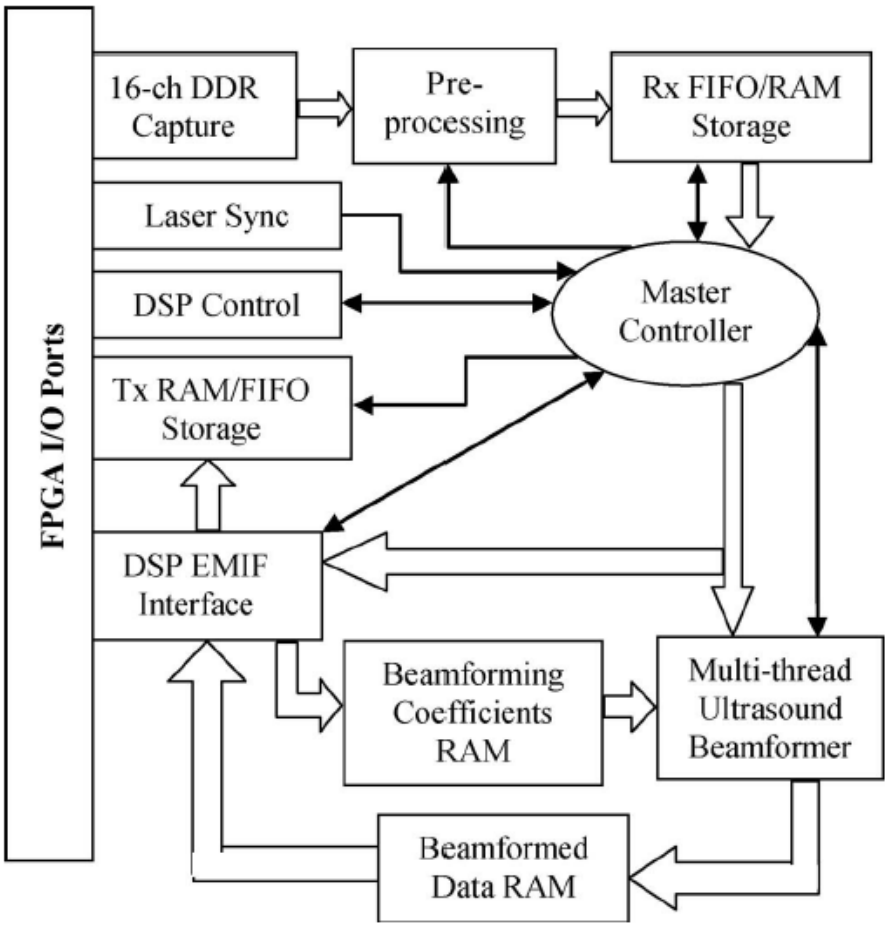


Figure 3.3 The overall block diagram of the FPGA code[17].

The ADC RF data are stored automatically at each rising edge of the sampling clock to the FIFO port, whereas these values can be randomly accessed with a reading address given by the DSP EMIF or the beamformer from the RAM port. The FIFO is made by generating the address automatically at each clock rising edge with a digital counter for the FIFO port of the dual-port RAM. The transmission (Tx) RAM/FIFO has similar structure but the reading and writing ports are reversed to allow feeding then transmitting.

C. EMIF Interface and Control of DSP

The DSP external memory interface (EMIF) includes the necessary scheme to communicate with the DSP board. The DSP address, data bus, and basic read/write control signals are connected with one 80-pin connector to each FPGA. The other DSP control signals are connected through two 40-pin connectors. Some of these signals are used for communicating with FPGAs based on the mode of imaging, acquisition and transmission, and reset. Also, some of the signals are used to inform the DSP about the laser pulse synchronization, the change of the wavelength of the laser, and whether the beamforming RAM is ready from the FPGAs. The DSP EMIF data bus and address lines are also connected to the master controller, which decides where to connect them based on the mode of imaging by digital multiplexers. In PE mode, the DSP writes the beamforming delay coefficients of 1024 focusing points distributed over 7.68 cm depth. The value of the coefficient is basically the address of each channel to be accessed in the Rx FIFO/RAM for each focusing point. The DSP also writes the Tx FIFO binary values for a length of 1024 to be transmitted out at 100 MHz clock speed. After the beamforming is done, the DSP reads the beam-line output from the beamforming RAM. In PAT mode, the DSP only reads the RF data directly from the Rx FIFOs, where only the first 2048 values from each channel Rx FIFO/RAM are accessed.

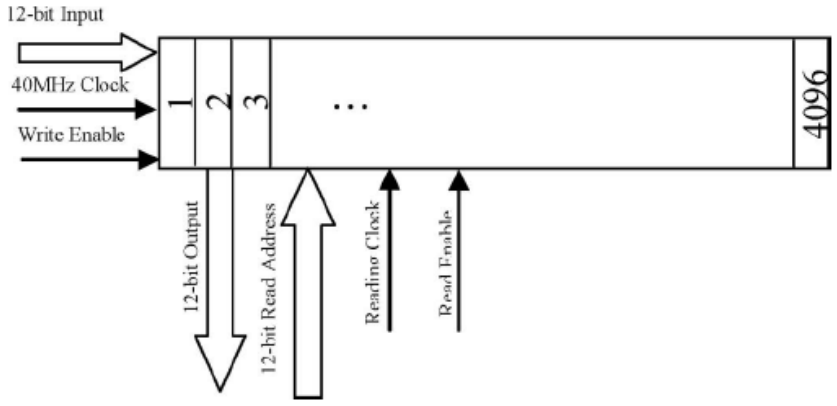


Figure 3.4 The block diagram of the receive (Rx) first-in, first-out (FIFO)[17].

D. Multi-Thread Ultrasound Beamformer

The delay-and-sum beamforming of acquired RF data for PE mode are done within the FPGA for the local 16 channels. The method of our beamforming is similar to Reference 17, except that we use only coarse delay coefficients because our ADC sampling frequency is reasonable compared with the transducer frequency. In addition, we directly access the value of the RF data from the Rx FIFO with the required delay corresponding to a linear function of the address (e.g., 3000 address value at 40 MHz sampling frequency corresponds to 3000/40 MHz = 75 μs delay). This address is precalculated in the PC and then transferred to the DSP, which feeds it to each FPGA at the beginning of each A-line acquisition. The beamformer code iteratively accesses the Rx FIFO/RAM of each channel for each focusing point with the corresponding precalculated address; and then sums all of the accessed values and stores them in the beamformed data RAM. However, because we want the beamformer output to have the same length of the Rx FIFO (4096), 3072 more points are added between the 1024 focusing points by interpolation. The beamformer performs the fetching of addresses for different channels and interpolates the three other points between each pair of focusing points in an overlapping fashion to reduce the total time needed. Forty-four steps are required to calculate the value of the beam at a certain focusing point and its three neighboring points; they are repeated 1024 times. With a 50-MHz processing clock, we achieve 44 × 1024/50 MHz = 901 μs per beam-line. If 100 beam-lines per frame are used, it's 90 ms per frame. If higher speed is needed, a 100 MHz processing clock can be used, and 45 ms per frame can be achieved, which corresponds to a maximum frame rate of 22 fps. If more speed is needed, it's also possible to truncate the three points in between each two focusing points that will shrink the number of steps down to 20 and provide more than 60 fps maximum frame rate (no other delay factors considered in this calculation). The other three points between each two focusing points are calculated by interpolating addresses between the two focusing points' addresses as follows:

$$A_{inc} = \frac{A_4 - A_0}{4}, A_{i+1} = A_i + A_{inc} \quad (3.1)$$

where Ainc is the address increment step between the points, A0 is the preceding focusing point address, A4 is the next focusing point address, i = 0, 1, 2, 3.

The beamformer does 1024 iterations, each of 44 steps (6-bit counter). Thus, four beamformed data points are stored in the end of each round. After finishing 1024 (10-bit counter) iterations, the total number of stored beam points is 4096 in the beamformed data RAM and a beamforming ready flag is raised. The DSP starts reading the beamformed data RAM once it receives the flag. The block diagram of the multi-thread beamformer is summarized in Figure 3.6.

The beamforming is done in pulse-echo mode only to reduce the amount of data to be transferred from each FPGA board by a factor of 1/16 for each beam-line; this is not done for PA mode because there is much less data to transfer. However, it would be easy to extend the idea of the pulse-echo beamformer to PA mode, and to have both of them done using the same FPGA code if higher PA processing speed is needed.

E. Master Controller and Reconfigurability

Most of the interconnections between different blocks are controlled by the master controller, which is eventually controlled by the DSP control signals. The master controller tries to organize both imaging processes in a very accurate manner using the precise timing and control capabilities of the FPGA. Based on the DSP signal for the mode of imaging, the master controller restructures the functions of the FPGA and its storage handling. In PAT mode, the Rx FIFO/RAM length is reduced to 2048 and the output of the Tx RAM/FIFO is disabled and replaced by zero value. The FPGA triggers the DSP by an elongated laser synchronizing pulse and makes sure that it receives the trigger by handshaking. Then, the Rx RAMs for 16 channels are lumped together and made directly accessible by the DSP board as one RAM.

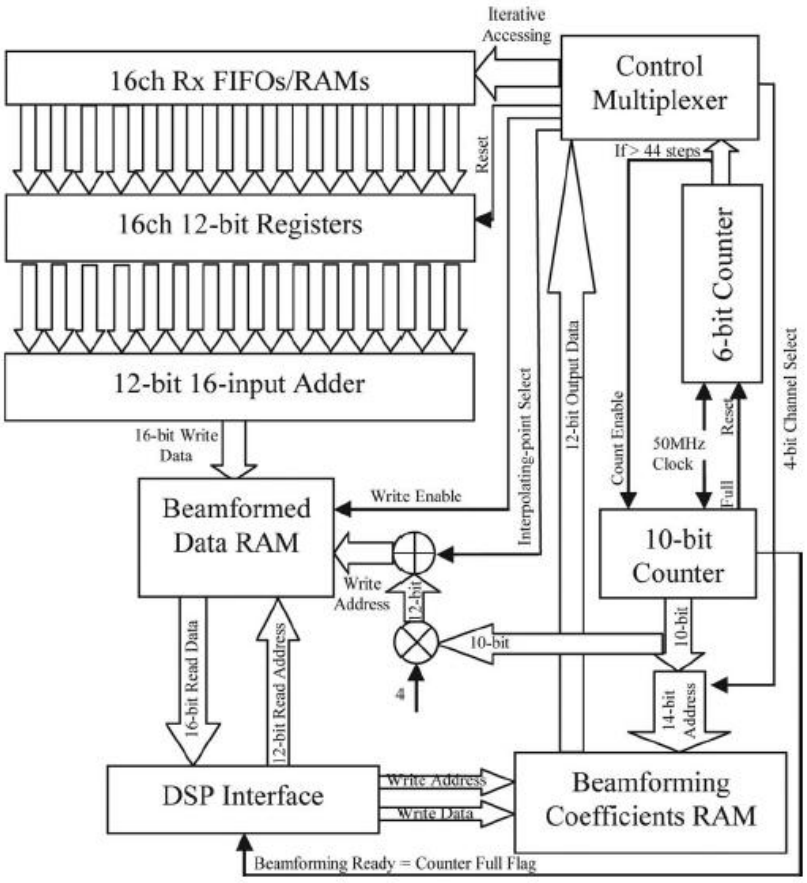


Figure 3.5 The block diagram of the beamforming code.

On the other hand, in PE mode, the Tx RAM/FIFO, beamformer, and the beamformed data RAM are enabled. The DSP triggers the FPGA after writing to the Tx RAM/ FIFO and the beamforming coefficients RAM to start beam acquisitions. Time-division multiplexing (TDM) is done to allow acquisition of the PE data while the laser is still pulsing. The master controller checks the laser synchronization pulse and how far it is from the DSP trigger. If the laser pulse is more than 0.2 ms (4096/40 MHz) away (to ensure that the generated photoacoustic signal from the running laser is not interfering with the pulse echo signals), the master controller starts shifting out the values of the Tx FIFO and at the same time storing the received RF data to the Rx FIFOs. Otherwise, it will wait to ensure that the required delay is achieved. If, by coincidence, the acquisition is started but the laser pulse comes before the acquisition is finished, the master

controller will reset the Rx storage and restart the acquisition once the laser pulse is at least 0.2 ms away. Figure 3.7 shows the block diagram of the TDM scheme.

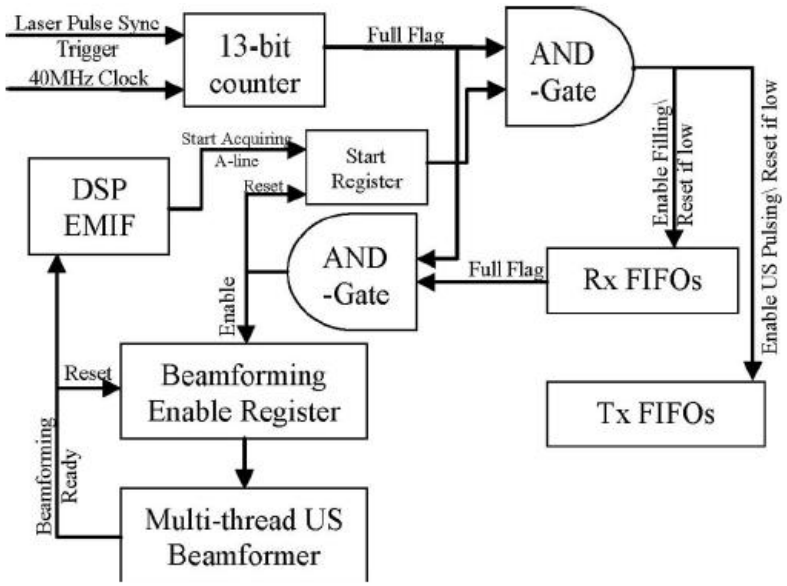


Figure 3.6 Block diagram of the time-division multiplexing (TDM) scheme for acquiring the pulse-echo (PE) A-lines while the laser is pulsing to ensure no photoacoustic (PA) interference. Note that the 12-bit counter starts counting when it is triggered by the laser synchronizing pulse until it is full, then it waits until the next laser pulse, when it resets and starts counting again[17].

Note that the TDM scheme is important because the Nd:Yag laser pump is self-triggering at 15 pulses per second and its manufacturer doesn't guarantee stable output pulse energy if an external trigger is used with a lower pulse repetition rate (because, in that case, the pulsing must be shut off during PE acquisition). It would also be more difficult to electro-optically shut off the laser output than using the TDM scheme. Note also that if the PE signal contrast is very high, the PA interference won't be noticed without the TDM. Nevertheless, if the PA target contrast is very high and the PE contrast is very low, the PA interference will definitely show up randomly in the PE image when the PE acquisition is done close to the laser pulse. However, with the TDM scheme, it is guaranteed that the PA interference won't interfere with the PE acquisition.

### 3.2.3 DSP Code Structure

DSP works as data coordinator of the whole system. It accepts necessary coefficient for transmission focusing and PE beamforming from PC and distributes them to module FPGAs at first. It controls the timing of DAQ in both PE and PAT mode. Although the FPGA processor has TMD inside its code, the PE DAQ and PAT DAQ are still done in a sequential manner. (It becomes a real TMD in our second version of system, where PE DAQ is done in the interval of laser pulses while PAT DAQ is synchronized with laser trigger). After running, DSP is waiting for PC to get the PE mode transmission coefficient and then PE mode beamforming coefficient. PE Tx coefficients are arranged in a two dimensional array as integer [*scanlines*][*elements*], where *scanlines* is the total beams/scan lines in the range of scanning, *elements* is the current used elements in the probe. Note that *elements* is not necessary equal to the total elements of the probe since we can use part of element only. On the other hand beamforming coefficients are arranged as a similar 3D array as integer [scanlines][receivingfocus][ element]. To form the receiving focal point *j* on the scan line *i*, we need pick up the coef[i][j][k] th value of kth element data and sum them up, k = 0, 1,… N-1, N is the current used elements. There is enough memory inside DSP to hold the timing FIFO of each element for every scan line and sub-beamforming coefficients for each module FPGAs. After this, the main code enters into a while loop, where it monitors the command sending by PC side. There are three types of commands to communicate with PC: CMD_NOP, CMD_RUN and CMD_STOP; CMD_NOP is performed when PC and DSP is idle. CMD_STOP is sent by PC side to stop current sampling and subbeamforming. CMD_RUN will get DSP into working loop where imaging mode and other parameters are also sent to conduct necessary operation. When command is CMD_RUN, PC side will send an integer which is decoded as imaging mode and PAT average times. The high 16bit is decoded as imaging mode, and the low 16bit is the PAT average times if the imaging mode is PAT or Coregistered (COREG) mode. In PAT mode, DSP will set the imaging mode for module FPGAs and do the PAT DAQ by

the required average times. Because the data format for the raw data transfer is short integer (16bit) and the ADC is a 12bit, only up to 2^4 = 16 times is available. The PAT data averaging is not directly conducted in DSP code. In DSP code, raw data are simply summed up.

PE mode needs to steer the beam direction. In PE mode, DSP switches the imaging mode to PE and then iterate DAQ and beamforming for all the scan line directions. Note that for every scan line, the Tx FIFO is sent by DSP via the EMIF interface. EMIF 16bit bus is enough for our up to 4096 receiving focuses. The sub-beamformed data is accumulated at DSP memory, DSP continue the beamforming by simply adding them up. Then the beamformed data is sent to PC by blocks. In COREG mode, in this first version system, we just simply do DAQ for PE before PAT DAQ and sent both PE beamformed data and PAT raw data to PC. In this mode, DSP must clear the timing FIFO before switching to PAT mode. Through the simple TCP/IP communication between PC and DSP, DSP code can work in three imaging mode for different probes. The only thing DSP needs is the Tx coefficients, beamforming coefficients and the command in while loop.

Note that the Ethernet cable in this configuration must be the cross-over Ethernet cable. At the same time, PC and DSP must be assigned different IP address. DSP IP is assigned as 168.192.1.12 while PC side can use 168.192.1. X, where X can be any number between 1 to 255, except 12. IP 168.192.1.0 is used as gateway. PC side configuration can be easily set from control panel ->internet connection->Properties->TCP/IP.

### 3.2.4 PC Program for DSP-based System

PC program is built with Microsoft Visual Studio. GUI design is based on the dialog based MFC frame work. A class called PATExpSetup is built for the coefficient calculation and storage. It can pre-calculate PE Tx delay coefficients, PE/PAT beamforming coefficient and PE/PAT scan conversion coefficients. The communication with DSP is done by TCP/IP socket. Data received from DSP is processed in sequential manner using FFT based method. There are

several subroutines for PE and PAT data processing: PAT beamforming, PE/PAT envelope detection, PE/PAT scan conversion and PE/PAT image fusing (coregisration). Three options are provided in the envelope detection subroutines: Hilbert transform, base-band demodulation and absolute value followed low pass filter. After getting beam envelopes, light absorption at pixels location are estimated via bilinear interpolation.[22] Usually these interpolation will be mapped logarithmically (sometimes, linearly) to pixel values, where pixel value 255 is the highest envelopes and 0 means the threshold set by dynamic range or system noise estimated from non-region-of-interest.

A) Envelope detection

Hilbert transforms are used extensively for analysis and processing in passband communication systems. let *x(t)* have the Fourier transform *X(ω)*. The Hilbert transform of *x(t)* will be denoted by $\hat{x}(t)$ and its Fourier transform by $\hat{X}(\omega)$. The Hilbert transform is defined by the integral

$$\hat{x}(t) = x(t) \otimes \frac{1}{\pi t} = \frac{1}{\pi} \int_{-\infty}^{\infty} \frac{x(\tau)}{t-\tau} d\tau \tag{3.2}$$

where $\otimes$ represents (linear) convolution. Thus, the Hilbert transform of a signal is obtained by passing it through a filter with the impulse response:

$$h(t) = \frac{1}{\pi t} \tag{3.3}$$

The discrete-time Fourier transform (DTFT) of *h(t)* is :

$$H(\omega) = -\mathrm{j}.\,\mathrm{sgn}(\omega) = \begin{cases} -\mathrm{j}, & \text{for } \omega > 0 \\ 0, & \text{for } \omega = 0 \\ \mathrm{j}, & \text{for } \omega < 0 \end{cases} \tag{3.4}$$

Therefore in frequency domain,

$$\hat{X}(\omega) = X(\omega)H(\omega) = \big(-\mathrm{j}.\,\mathrm{sgn}(\mathrm{w})\big)\mathrm{X}(\omega) \tag{3.5}$$

The analytic signal associate with *x(t)* is

$$x_+(t) = x(t) + j\hat{x}(t) \tag{3.6}$$

The Fourier transform of $x_+(t)$ is

$$X_+(\omega) = 2X(\omega)u(\omega) = \begin{cases} 2\mathrm{X}(\omega) & \text{for } \omega > 0 \\ \mathrm{X}(0), & \text{for } \omega = 0 \\ 0, & \text{for } \omega < 0 \end{cases} \tag{3.7}$$

It has only one side of spectrum. Negative frequencies are vanished. For a finite length signal, *x[n]*, PE or PAT beams in our application, Reference 24 presents an algorithm for the estimation of analytic signal $x_+[n]$ with the help of FFT. It calculates the FFT of input sequence, replaces those FFT coefficients that correspond to negative frequencies with zeros, and calculates the inverse FFT of the result.

step 1 : calculate the FFT of *x[n]*, n = 0, 1, …N-1, and store the result in *X[n]*, where *X[n]* is complex array.

step 2 : For n = 0 and n = N/2, keep it unchanged. For n = 1, 2, N/2 – 1, there positive frequencies coefficient are doubled and then set all the coefficient for n = N/2 + 1,…, N/2 – 1 to zeros, these frequencies are negative.

step 3: perform inversed FFT on the result from step 2 and store the result in $x_+[n]$. At this time, $x_+[n]$ is a complex array, the real part of $x_+[n]$ is exactly same as x[n], while the imaginary part of $x_+[n]$ is the Hilbert transform of *x[n]*, which is donated as $\hat{x}[n]$.

step 4 : calculate the envelop signal from the following formula:

$$E(n) = \sqrt{x[n]^2 + \hat{x}[n]^2} \tag{3.8}$$

where *E(n)* is the envelop signal.

Theoretically, Hilbert transform can get the best approximation of original signal's envelop. However, it keeps all the frequencies in original signal. The beam signal from delay-and-sum algorithm usually are affected by system noise, especially for PAT signal because of its low SNR, so envelop estimated from Hilbert transform often presents unwanted noise in the image domain. Alternatively, base band demodulation method is preferred in practical application.

The beamformed signal can be viewed as a band-limited signal with center frequency at the oscillation frequency of transducer *f0*. Because it is a real signal, it can be shifted to DC by multiplying it with complex signal $exp(-jw_0t)$, $w_0 = 2\pi f_0$. Then a low pass filter can be used to remove other frequencies but the frequencies in the relative bandwidth of transducer. The corresponding result is the complex envelop of the original signal (beam). The real and imaginary part of the result is called in-phase signal and quadrature signal respectively. The difference between analytic signal and complex envelop is that analytic signal is centered at $f_0$ while complex envelop is down shifted to zero. So the envelop can be calculated from the in-phase and quadrature signal. In-phase and Quadrature (IQ) demodulation is illustrated in Figure 3.7.

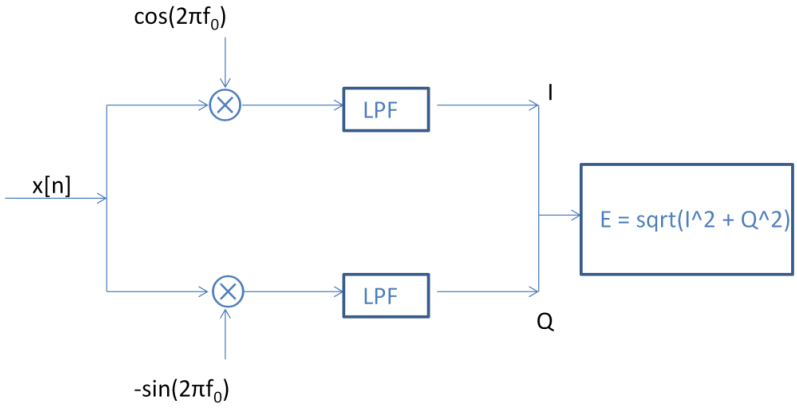


Figure 3.7 Illustration of In-phase/Quadrature method for envelope detection. Low pass filters cover the bandwidth of beam signal.

There is another simple but not accurate envelope detection method called ABSLP where ABS means absolute value and LP is low pass filter. In the early stage of ultrasound machine, this method was used and now it is out of date.

B) FFT based acceleration.

No matter which envelop detection method we uses, we'd better use FFT based processing to accelerate PE/PAT imaging speed. Real time is quite critical in clinical application. Here, two tricks are used for the further simplification of processing. Since the beam signal are all real-valued, we can fully use this feature to reduce the time consumption of signal processing.

Assume we have a subroutine for FFT computation of complex input array of length N, the output array is also a complex array of length N. We can simplify the FFT computation of two real input arrays *x1[n]* and *x2[n]* by just one complex FFT.

Case one: fill x1[n] into the real part of input array and imaginary parts are left zero, n = 0, 1, …, N-1, then the FFT of x1[n] is symmetric:

$$X1(k) = X1^*(N-k), k = 0, 1, \dots, N-1 \quad (3.9)$$

The real part of X1(k) has even symmetry about the N/2 point, and imaginary part of X1(k) has odd symmetry about N/2 point.

Case two: fill x2[n] into the imaginary part of input array and real parts are left zero. Then FFT of x2[n] is anti-symmetric:

$$FFT[jx2(n)] = X2(k) = -X2^*(N-k), k = 0, 1, \dots, N-1 \quad (3.10)$$

The real part of X2(k) has odd symmetry about the N/2 point, and imaginary part of X2(k) has even symmetry about N/2 point.

Case three: pack x1[n] in real part of input array and x2[n] in the imaginary part of input array and take the FFT of y[n] = x1[n] + jx2[n].Then

$$\mathrm{Y[k]} = \mathrm{X1[k]} + \mathrm{X2[k]} \tag{3.11}$$

Substitute k with N-k and take the conjugate of both sides of equation 3.11, we can get:

$$\mathrm{Y^*[N-k]} = \mathrm{X1^*[N-k]} + \mathrm{X2^*[N-k]} \tag{3.12}$$

Using equation 3.9 to 3.12, we can have

$$\begin{aligned} X1(k) &= \frac{Y[k] + \mathrm{Y^*[N-k]}}{2} \\ X2(k) &= \frac{Y[k] - \mathrm{Y^*[N-k]}}{2} \end{aligned} \tag{3.13}$$

Note that *X2[k]* is the FFT of *jx2[n]*, we should divide it by j to get the true FFT of x2[n];

$$X2\_true(k) = \frac{Y[k] - \mathrm{Y^*[N-k]}}{2j} \tag{3.14}$$

In this way, we can get the FFT of two real input arrays by using one single complex FFT subroutine.

(C) Application of circular convolution

The length of linear convolution of two input array x1[n] and x2[n] is length(x1) + length(x2) – 1; In the IQ demodulation method, LPF is used to filter unwanted frequencies besides the bandwidth of transducer. The beam length is 4096 for PE beam and 2048 for PAT beam. Take PAT as an example, if we use a linear convolution method, we need to append 2048 zeros to the end of beam and 2048*2 – length(LPF) to the end of filter coefficients to get a fast implementation of filtering. After that, we need to cut 2048*2 – (2048 + length(LPF) -1) zeros at

the end of filtering result. This operation involves memory reallocation, zero padding and cutoff zeroes. In theory, it is correct and not efficient in practical application. One fact that the PAT beams or PE beams have very high amplitude points near the transducer face because of light absorption by transducer itself and for ovary cancer detection, the 1cm vaginal muscles wall is meaningless, we usually cutoff these parts of beam by setting them to zeros. This fact allows us to directly use circular convolutions to implement the LPF in IQ envelop detection. Theoretically, there are two time domain overlaps with length equal to length (LPF) – 1 in the beginning of convolution and the end of circular convolution. For the overlap in the end of convolution, it is about 7.7 cm and in most cases, light from delivery fiber is hard to get there. Almost no signal can be retrieved from there. We can just simply set this overlap to zeros. In short, we can just do length (beam) of FFT for LPF coefficients and beams, multiply them in frequency domain and do reversed FFT for the result. Note that we need to shift the circular convolution by the group delay of LPF, which is equal to *(length(LPF) – 1) /2*. In our application, *length(LPF)* is selected to be an odd integer.

(D) Scan conversion for PE and PAT beams.

Scan conversion can be viewed as two dimensional interpolations. For pixels outside of fan shape region, they are set to black. For pixels inside the fan shape, it must be surrounded by four nearest points on two consecutive beams.[25]

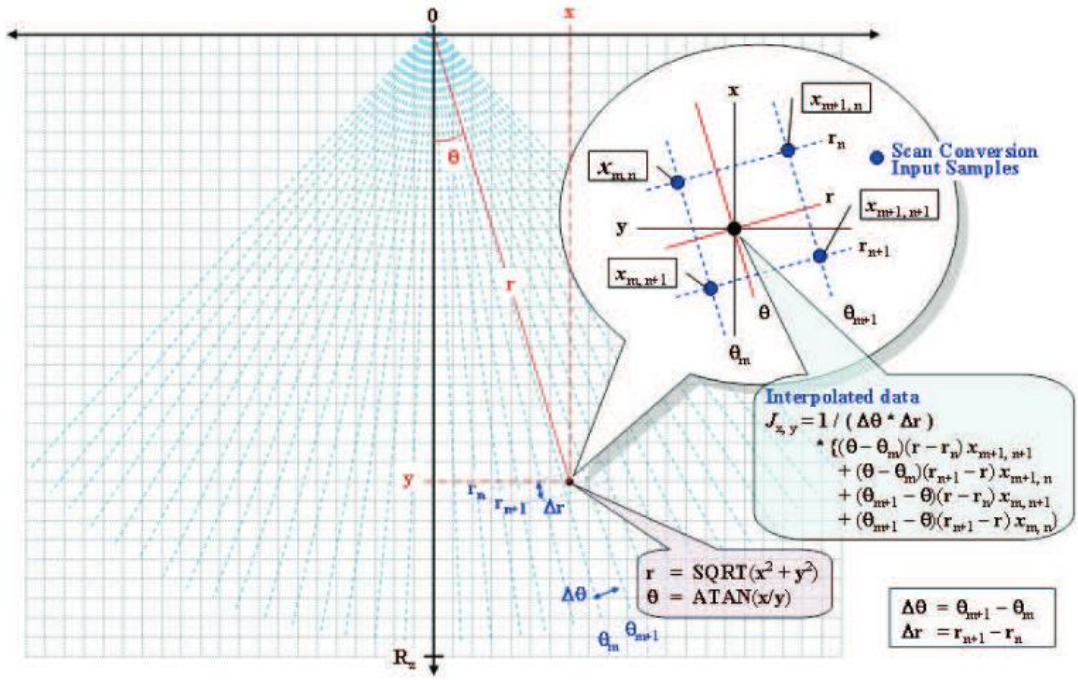


Figure 3.8 Scan Conversion Using Bilinear Interpolation for Sectored Image [25]

The pixel coordinate is (r, θ), and the four nearest points are Xm_n($r_n$, $\theta_m$), Xm_n+1($r_{n+1}$, $\theta_m$), Xm+1_n($r_n$, $\theta_{m+1}$) and Xm+1_n+1($r_{n+1}$, $\theta_{m+1}$). The coefficient of point Xm_n is ($r_{n+1}$ – r)*( $\theta_{m+1}$- θ)/(( $r_{n+1}$ - $r_n$)*( $\theta_{m+1}$-$\theta_m$)). The geometrical meaning is the ratio of the area of rectangle with left top as (r, θ) and right bottom as Xm+1_n+1($r_{n+1}$, $\theta_{m+1}$) over the area of rectangle with left top as Xm_n($r_n$, $\theta_m$) and right bottom as Xm+1_n+1($r_{n+1}$, $\theta_{m+1}$). The coefficients of the other three points can be calculated in a similar way. The sum of these four coefficients is equal to one. Then the interpolated envelope at the pixel is the summation of the products of coefficient and envelope at four points, see Figure 3.8.

(E) Logarithmic compression and display

Because of the limited dynamic range of human eyes, PE and PAT interpolated envelopes need a logarithmic compression to map the original data into a range acceptable by human eyes. For PAT, if the dynamic range of original data is small enough (less than 20log10(256) = 48dB),

the logarithmic compression is not necessary. In that case, linear mapping is used. After logarithmic compression, the result needs to be mapped the pixel value of Bitmap. For PE images, the colormap of the Bitmap is gray scale, range from RGB(0,0,0) to RGB(255, 255, 255). Same colormap can be used for pure PAT mode. For Coregistered mode (COREG), the 256 items in colormap are divided into two halves: 0 ~127 are gray scale and 128 ~255 are changed from RGB(255, 0, 0) to RGB(255, 255, 0) with only Green component changing. For the same pixel, if PAT envelop of that pixel is larger than the threshold set by PAT dynamic range or system noise, then PAT pixel value will overwrite the underlying PE values.

### 3.2.5 Oxygen Saturation Estimation

The model for oxygen saturation (SO2) estimation is introduced in Reference 26 to Reference 28. In polar coordinates, the model starts by defining the photoacoustic pressure P(r, θ, λ) at each point (r, θ) away from the array transducer center, after being detected by the system and spatially resolved by beamforming, as

$$P(r,\theta,\lambda) = C_0(r,\theta)F_0(\lambda)F(r,\theta,\lambda)\Gamma(r,\theta)\mu_a(r,\theta,\lambda) \quad (3.15)$$

, where $\mu_a$ is the absorption coefficient at each pixel point in the tissue (1/cm) for each wavelength $\lambda$. $F_0$ is the laser output energy per pulse (in joules) at each wavelength, $F$ is the normalized fluence distribution for each wavelength at each point in the imaging plane. $\Gamma$ is the dimensionless Grüneisen coefficient for each point in the tissue and $C_0$ is another normalization factor for each point (r, θ ) in the imaging plane; which depends mainly on the photoacoustic impulse response of the tissue at each point (r, θ) convolved with the transducer impulse response and the temporal profile of the laser pulse. $F(r, \theta, \lambda)$ can be approximated as wavelength-independent function $F(r, \theta)$ in the NIR wavelength range, because the wavelength-dependent tissue scattering change in that window is small, and the wavelength-dependent absorption of the tissue is limited to small targets such as vessels, whereas most of the tissue has approximately the

water absorption, which is almost constant over that wavelength window.26-29 So the normalized photoacoustic pressure by the laser energy per pulse $F_0(\lambda)$ can be approximated as

$$\begin{aligned} P_{normalized}(r,\theta,\lambda) &= \mathrm{C_0(r,\theta)F(r,\theta,\lambda)\Gamma(r,\theta)\mu_a(r,\theta,\lambda)} \\ &= C(\mathrm{r},\theta)\mu_\mathrm{a}(\mathrm{r},\theta,\lambda) \end{aligned} \tag{3.16}$$

, where *C* varies at every point in the sample but is independent of wavelength as long as the target is fixed with respect to the illumination and ultrasound detection.

Therefore, for each point in our imaging plane (r, θ ), we must solve a set of equations defined as

$$\begin{bmatrix} P_{normalized}(\lambda_1) \\ P_{normalized}(\lambda_2) \\ P_{normalized}(\lambda_3) \\ \vdots \\ P_{normalized}(\lambda_4) \end{bmatrix} = \begin{bmatrix} \varepsilon_{HbO2}(\lambda_1) & \varepsilon_{Hb}(\lambda_1) & 1 \\ \varepsilon_{HbO2}(\lambda_2) & \varepsilon_{Hb}(\lambda_2) & 1 \\ \varepsilon_{HbO2}(\lambda_3) & \varepsilon_{Hb}(\lambda_3) & 1 \\ & \vdots & \\ \varepsilon_{HbO2}(\lambda_4) & \varepsilon_{Hb}(\lambda_4) & 1 \end{bmatrix} \begin{bmatrix} C' * [HbO2] \\ C' * [Hb] \\ C' * K \end{bmatrix} \tag{3.17}$$

where $\varepsilon_{HbO2}$ and $\varepsilon_{Hb}$ are molar extinction coefficients of the oxy-hemoglobin and deoxy-hemoglobin as a function of the wavelength λ, respectively; The conversion between extinction coefficients and absorption coefficients is shown in Reference 30 as:

$$\mu_a = (2.303)\varepsilon * (x\ g/liter)/(64{,}500\ g\ Hb/mole) \tag{3.18}$$

where *x* is the number of grams per liter. A typical value of *x* for whole blood is *x* =150 g Hb/liter. So $C'$ = C/ (2.303 * x * 64500), and x = 150 g Hb/liter. *K* is the y-intercept, which represents the absorptions of water and other tissue constituents; all are assumed to be constant over the wavelength window used. Because we have more equations than variables, some optimization method can be used to get a more stable solution of *[HbO2]* and *[Hb]* for the estimation of $S_{O2}$. Oxygen saturation can be estimated from following equation:

$$S_{O2} = \frac{C' * [HbO2]}{C' * [HbO2] + C' * [Hb]} = \frac{[HbO2]}{[HbO2] + [Hb]} \tag{3.19}$$

The least square error of between left side and the right side of equation 3.17 can be solved by common optimized method using data from multiple wavelengths, such as gradient descent or Newton's method. Note that there are several constraints for this minimization problem. For example, [HbO2] and [Hb] are positive and the absorption of Hb and HbO2 should be much larger than term C'K.

$$\begin{gathered} e = \|P_{normalized} - WX\|^2 \\ s.t.: X > 0 \\ \varepsilon_{HbO2}(\lambda) * [HbO2](\lambda) + \varepsilon_{Hb}(\lambda)[Hb](\lambda) \gg 1 \end{gathered} \tag{3.20}$$

, where *W* is the first matrix on the right side equation 3.17, *X* is the second matrix on the right side of equation 3.17.

More practically, we can ignore the absorption of water and other constituents. Equation 3.17 can be simplified to:

$$\begin{bmatrix} P_{normalized}(\lambda_1) \\ P_{normalized}(\lambda_2) \\ P_{normalized}(\lambda_3) \\ \vdots \\ P_{normalized}(\lambda_4) \end{bmatrix} = \begin{bmatrix} \varepsilon_{HbO2}(\lambda_1) & \varepsilon_{Hb}(\lambda_1) \\ \varepsilon_{HbO2}(\lambda_2) & \varepsilon_{Hb}(\lambda_2) \\ \varepsilon_{HbO2}(\lambda_3) & \varepsilon_{Hb}(\lambda_3) \\ & \vdots \\ \varepsilon_{HbO2}(\lambda_4) & \varepsilon_{Hb}(\lambda_4) \end{bmatrix} \begin{bmatrix} C' * [HbO2] \\ C' * [Hb] \end{bmatrix} \tag{3.21}$$

, and the constraint in equation 3.20 is just $s.t.: X > 0$. Note in practical calculation, we divide interpolated envelop by the light intensity of laser measured by photodiode or separate single element ultrasound probe visa PA effect at each wavelength to get the normalized pressure. $S_{O2}$ then is calculated pixel by pixel using the optimization method. In practical calculation, It is possible that at certain pixel, the interpolated envelop at certain wavelength may be lower than noise threshold. So at least data at two wavelengths are needed to calculate $S_{O2}$, otherwise we

just set it as zero (not for calculation). The $S_{O2}$ map can also be registered with PE image but shown with different color map.

## 3.3 Real-time US/PAT System Based on PCIe Transfer

In 3.2, a slower version of US/PAT system is shown in detail. It has ultrasound, PAT and Coregistered modes. The delay coefficients for ultrasound mode transmission and sub-beamforming / beamforming are transmitted from PC via cross-over Ethernet cable at the very beginning of program. These coefficients can be used for three imaging modes. In PAT, no transmission is needed. For each frame, PC notifies DSP which imaging mode it will run in next frame. DSP decodes this command and do DAQ for the corresponding imaging mode and transfers data to PC for further processing after this frame DAQ is done. However, there are some bottlenecks in this design, especially in terms of data transfer. When DSP needs to switch imaging mode, it needs to adjust logical level of certain GPIO (General Purpose Input-Output) register on DSP board to notify module-FPGAs. For the timing of ultrasound mode, the value of timing FIFO is transmitted to each FPGA by EMIF (External Memory Interface). This procedure is relatively slow. On the other hand, the data transfer via Ethernet cable is another bottleneck. Ideally, the data transfer rate of Ethernet cable can reach up to 100Mbps (bit per second). If we put all the processing units (beamforming, envelop detection, scan conversion) to FPGAs and just transfer PE/PAT images for display, the TCP/IP socket can handle it. However, we need to transfer raw data (Radio-frequency data) to PC side for further analysis meanwhile we don't have enough manpower to put processing unit to FPGAs. In this second version of ultrasound/PAT system (PE/PAT system), an advanced FPGA board is introduced in order to solve the data transfer problem. This FPGA board provides faster data communication between module FPGAs using LVDS and integrate PCIe protocol as an IP core which provides up to 2.5 Gbps data transfer rate. Furthermore, the PCIe protocol is DMA based protocol which allows us to accelerate imaging program by using multithreads technique in C++ program.

### 3.3.1 PCIe Transfer Protocol

PCI Express (Peripheral Component Interconnect Express), officially abbreviated as PCIe, is a high-speed serial computer expansion bus standard designed to replace the older PCI, PCI-X, and AGP bus standards. PCIe has numerous improvements over the older standards, including higher maximum system bus throughput, lower I/O pin count and smaller physical footprint, better performance scaling for bus devices, a more detailed error detection and reporting mechanism (Advanced Error Reporting, AER), and native hot-plug functionality. More recent revisions of the PCIe standard provide hardware support for I/O virtualization.[31]

Its format specifications are maintained and developed by the PCI-SIG (PCI Special Interest Group), a group of more than 900 companies that also maintain the conventional PCI specifications. PCIe 3.0 is the latest standard for expansion cards that is in production and available on mainstream personal computers.

The PCIe used in our Virtex V FPGA board (Xpress LX110T by PLDA, San Jose, California) is generation 2 with 8 lanes. The data transfer can reach to 2.5 Gbps, which can satisfy our application. More importantly, this data transfer is DMA based transfer and makes the multi-threads valuable for this US/PAT Coregistered imaging system.

### 3.3.2Multi-threads Technique[32]

In computer architecture, multithreading is the ability of a central processing unit or a single core in a multi-core processor to execute multiple processes or threads concurrently, appropriately supported by the operating system. This approach differs from multiprocessing, as with multithreading the processes and threads have to share the resources of a single or multiple cores: the computing units, the CPU caches, and the translation lookaside buffer (TLB).

Where multiprocessing systems include multiple complete processing units, multithreading aims to increase utilization of a single core by using thread-level as well as instruction-level parallelism. As the two techniques are complementary, they are sometimes combined in systems with multiple multithreading CPUs and in CPUs with multiple multithreading cores.

Two major techniques for throughput computing are multiprocessing and multithreading. If a thread gets a lot of cache misses, the other threads can continue taking advantage of the unused computing resources, which may lead to faster overall execution as these resources would have been idle if only a single thread was executed. Also, if a thread cannot use all the computing resources of the CPU (because instructions depend on each other's result), running another thread may prevent those resources from becoming idle. If several threads work on the same set of data, they can actually share their cache, leading to better cache usage or synchronization on its values.

There are three types of multithreading:

(1)Block multithreading

The simplest type of multithreading occurs when one thread runs until it is blocked by an event that normally would create a long-latency stall. Such a stall might be a cache miss that has to access off-chip memory, which might take hundreds of CPU cycles for the data to return. Instead of waiting for the stall to resolve, a threaded processor would switch execution to another thread that was ready to run. Only when the data for the previous thread had arrived, would the previous thread be placed back on the list of ready-to-run threads.

Conceptually, it is similar to cooperative multi-tasking used in real-time operating systems, in which tasks voluntarily give up execution time when they need to wait upon some type of the event. This type of multithreading is known as block, cooperative or coarse-grained multithreading.

The goal of multithreading hardware support is to allow quick switching between a blocked thread and another thread ready to run. To achieve this goal, the hardware cost is to replicate the program visible registers, as well as some processor control registers (such as the program counter). Switching from one thread to another thread means the hardware switches from using one register set to another; to switch efficiently between active threads, each active thread needs to have its own register set. For example, to quickly switch between two threads, the register hardware needs to be instantiated twice.

Additional hardware support for multithreading allows thread switching to be done in one CPU cycle, bringing performance improvements. Also, additional hardware allows each thread to behave as if it were executing alone and not sharing any hardware resources with other threads, minimizing the amount of software changes needed within the application and the operating system to support multithreading.

This type of multithreading is used in our US/PAT system design.

(2) Interleaved multithreading

The purpose of interleaved multithreading is to remove all data dependency stalls from the execution pipeline. Since one thread is relatively independent from other threads, there's less chance of one instruction in one pipe stage needing an output from an older instruction in the pipeline. Conceptually, it is similar to preemptive multitasking used in operating systems; an analogy would be that the time slice given to each active thread is one CPU cycle.

This type of multithreading was first called barrel processing, in which the staves of a barrel represent the pipeline stages and their executing threads. Interleaved, preemptive, fine-grained or time-sliced multithreading are more modern terminology.

In addition to the hardware costs discussed in the block type of multithreading, interleaved multithreading has an additional cost of each pipeline stage tracking the thread ID of the instruction it is processing. Also, since there are more threads being executed concurrently in the pipeline, shared resources such as caches and TLBs need to be larger to avoid thrashing between the different threads.

(3) Simultaneous multithreading

The most advanced type of multithreading applies to superscalar processors. Whereas a normal superscalar processor issues multiple instructions from a single thread every CPU cycle, in simultaneous multithreading (SMT) a superscalar processor can issue instructions from multiple threads every CPU cycle. Recognizing that any single thread has a limited amount of instruction-level parallelism, this type of multithreading tries to exploit parallelism available across multiple threads to decrease the waste associated with unused issue slots.

To distinguish the other types of multithreading from SMT, the term "temporal multithreading" is used to denote when instructions from only one thread can be issued at a time.

In addition to the hardware costs discussed for interleaved multithreading, SMT has the additional cost of each pipeline stage tracking the thread ID of each instruction being processed. Again, shared resources such as caches and TLBs have to be sized for the large number of active threads being processed.

In current program, the multithreading is implemented in semaphore because it is a typically example of producer-consumer problem in computer science.[33] In computer science, particularly in operating systems, a semaphore is a variable or abstract data type that is used for controlling access, by multiple processes, to a common resource in a concurrent system such as a multiprogramming operating system. A trivial semaphore is a plain variable that is changed (for

example, incremented or decremented, or toggled) depending on programmer-defined conditions. The variable is then used as a condition to control access to some system resource.

A useful way to think of a semaphore as used in the real-world systems is as a record of how many units of a particular resource are available, coupled with operations to safely (i.e., without race conditions) adjust that record as units are required or become free, and, if necessary, wait until a unit of the resource becomes available. Semaphores are a useful tool in the prevention of race conditions; however, their use is by no means a guarantee that a program is free from these problems. Semaphores which allow an arbitrary resource count are called counting semaphores, while semaphores which are restricted to the values 0 and 1 (or locked/unlocked, unavailable/available) are called binary semaphores.

When used to control access to a pool of resources, a semaphore tracks only how many resources are free; it does not keep track of which of the resources are free. Some other mechanism (possibly involving more semaphores) may be required to select a particular free resource.

The paradigm is especially powerful because the semaphore count may serve as a useful trigger for a number of different actions. The success of the protocol requires applications follow it correctly. Counting semaphores are equipped with two operations, historically denoted as P and V. Operation V increments the semaphore S, and operation P decrements it.

The value of the semaphore S is the number of units of the resource that are currently available. The P operation wastes time or sleeps until a resource protected by the semaphore becomes available, at which time the resource is immediately claimed. The V operation is the inverse: it makes a resource available again after the process has finished using it. One important property of semaphore S is that its value cannot be changed except by using the V and P operations.

A simple way to understand wait and signal operations is: Wait: If the value of semaphore variable is not negative, decrements it by 1. If the semaphore variable is now negative, the process executing wait is blocked (i.e., added to the semaphore's queue) until the value is greater or equal to 1. Otherwise, the process continues execution, having used a unit of the resource. Signal: Increments the value of semaphore variable by 1. After the increment, if the pre-increment value was negative (meaning there are processes waiting for a resource), it transfers a blocked process from the semaphore's waiting queue to the ready queue.

Producer/consumer problem

In the producer-consumer problem, one process (the producer) generates data items and another process (the consumer) receives and uses them. They communicate using a queue of maximum size N and are subject to the following conditions:

The consumer must wait for the producer to produce something if the queue is empty.

The producer must wait for the consumer to consume something if the queue is full.

The semaphore solution to the producer-consumer problem tracks the state of the queue with two semaphores: emptyCount, the number of empty places in the queue, and fullCount, the number of elements in the queue. To maintain integrity, emptyCount may be lower (but never higher) than the actual number of empty places in the queue, and fullCount may be lower (but never higher) than the actual number of items in the queue. Empty places and items represent two kinds of resources, empty boxes and full boxes, and the semaphores emptyCount and fullCount maintain control over these resources.

The binary semaphore useQueue ensures that the integrity of the state of the queue itself is not compromised, for example by two producers attempting to add items to an empty queue

simultaneously, thereby corrupting its internal state. Alternatively a mutex could be used in place of the binary semaphore.

The emptyCount is initially N, fullCount is initially 0, and useQueue is initially 1. The producer does the following repeatedly:

produce:

P(emptyCount)

P(useQueue)

putItemIntoQueue(item)

V(useQueue)

V(fullCount)

The consumer does the following repeatedly

consume:

P(fullCount)

P(useQueue)

item ← getItemFromQueue()

V(useQueue)

V(emptyCount)

In our US/PAT system, two threads are created to handle front end DAQ and back end data processing respectively. They run simultaneously and accelerate the whole imaging speeding by doing DAQ and data processing on front end FPGAs and CPU in parallel. The saved time compared with traditional sequential DAQ and processing is the smaller of the DAQ time and processing time.

### 3.3.3 System Design of PE/PAT System Based on PCIe Transfer

The first version US/PAT system used an Ethernet cable for data transfer and a digital signal processor (DSP, TI6455) for data coordination. The speed of the system was on average 1

frame per second (max 3 fps) and the number of channels was only 64. The DSP was used to form the pulse-echo transmit (Tx) timing first-in-first-out (FIFO) and to perform beamforming after fetching analog-to-digital converter (ADC) data from module FPGAs. The interface between DSP and module FGPAs is an external memory interface (EMIF) of the DSP chip, and the data transfer rate was low. Another bottleneck was the low-data transfer rate of the Ethernet cable (limited to 100 Mbps). Thus, the low-data transfer rate among module FPGAs, DSP, and PC limited the imaging frame rate. To solve the low-data transfer rate problem, we have used PCIe and low-voltage differential signaling (LVDS) tracks in our design. PCIe (up to 2.5 Gbps) has been used for data transfer between PC and Virtex 5 FPGA inside the PCIe board, which has served as a data coordinator. The LVDS between the PCIe board and module FPGAs has solved the problem of communications among different FPGAs. As a result, a 15 fps imaging frame rate has been achieved which is only limited by our laser repetition frequency.

This second version of US/PAT real-time system is designed to work in three different imaging modes: US mode, PAT mode, and Coregistered (COREG) mode. It requires different modules to perform data acquisition, transfer, and processing with negligible switch latency between the different imaging modes. From a hardware perspective, the real-time system mainly consists of a front-end analog circuitry, 8-module FPGAs, a PCIe card (Xpress LX110T by PLDA, San Jose, California), and a PC (Figure 3.9). The front-end analog circuitry and 8-module FPGAs work together to perform US transmission focusing, data sampling, and US receiving subbeamforming. The PCIe card works as a data coordinator. It obtains transmission and receiving beamforming delay profiles, calculated according to user's imaging setting (transmission focus, number of scan lines, and angular scan range) from the PC. It then distributes the delay coefficients to the memories of each module corresponding to its attached 16 channels. Once sub-beamforming is done in each module FPGA, the FPGA on the PCIe card continues US beamforming and envelope detection. The resulting beam envelopes are transferred to the PC for

scan conversion and display. For the PAT mode or Coregistered mode, the PCIe card directly transfers the PAT radio frequency (RF) data to the PC. The PC software performs PAT delay-and-sum beamforming, envelope detection, and scan conversion. Furthermore, the PC software graphics user interface allows user interaction for data storage and dynamic range selection for display with different color scales according to each imaging mode.

The real-time system features 128 parallel channels, each of which has its own transmit/receive (Tx/Rx) circuitry along with ADC sampling at 40 MHz. It is a modular design (Figure 3.10), where the front-end circuits of each set of 16 channels are grouped into one module that is plugged into a slot in the system motherboard. The transmission of every channel is controlled by the module FPGA using a Tx timing FIFO memory. Furthermore, ADC data are also captured by the module FPGA and stored in another Rx FIFO memory. US sub-beamforming of every 16-channel group is done by each module FPGA that features 2500 beam lines per second. US sub-beamforming data as well as PAT RF data from each module are collected by the Virtex-5 FPGA-based PCIe card plugged into the PC. All module FPGAs are connected to the PCIe card through another customized adapter board that uses LVDS tracks to achieve the ultrafast transfer rate. Here, each module FPGA has two pairs of dedicated one-way LVDS tracks single-edge pumped at 100 MHz and features a transfer speed of 200 Mbps per module. The modules are connected to the adapter board, and the adapter board is connected to the PCIe card. The PCIe card forms the final US beam from the sub-beamforming data, then stores it in an 8k × 64 bit FIFO. After that, envelope detection is done by taking the absolute value followed by low-pass filtering. PAT RF data are captured and stored in a 32k × 64 bit FIFO inside the PCIe card. The speed of communication between the PCIe card and the PC can reach up to 2.5 Gb ⁄ s, which adds a negligible latency to the overall acquisition time.

Each module FPGA has two embedded quad-data-rate static random access memory (SRAM) chips which can be freely accessed by the PC through general purpose register

input/outputs (GPIO) of the PCIe card. In the initialization stage, the PC transfers the time delay profiles for US transmission focusing and receiving beamforming to module FPGA's SRAMs via the PCIe card. In every acquisition cycle, the PC program informs the PCIe card of the index of the active scan line through GPIOs. Each module FPGA temporarily stores the Tx and Rx coefficients of the active scan line in its internal cache memory (Figure 3.11). The Tx coefficients of the active scan line contain the starting time for pulsing to each element, where a logical algorithm is used to construct the timing profile of every pulse for every element and store it to the Tx timing FIFOs.

US sub-beamforming is done within each module FPGA by fetching the data from all 16 channels of the Rx FIFOs/RAMs while realigning and adding (delay and sum). A 50-MHz clock is used for beamforming, which allows forming the beam for one scan line in 102.4 μs for 4096 Rx FIFO points (sampled at 40 MHz, allowing a 7.7 cm maximum imaging depth for US pulse-echo). However, since the internal cache of the FPGA has to be filled with the Tx and Rx coefficients, and the formed beam has to be sent to the PCIe card, the total time needed for the beam envelope data to reach the PC is 400 μs or 2.5k lines/s. For an image with 100 scan lines, after adding the scan conversion latency, the best frame rate achieved for US only imaging is 20 fps. In the PAT mode or Coregistered mode, the DAQ must be synchronized with the trigger from the laser system. The trigger wire is attached to the PCIe card which keeps checking the status of the trigger signal. The PC program waits for this trigger and sets the imaging mode register to the PAT mode. The FPGA structure can be switched from the PAT mode to the US mode in a fraction of a microsecond. Both PAT and US data acquisition is done between the two laser pulses, which is valuable in that it keeps the US image free from laser lamp coherent noise. With this optimization scheme, 15 fps in both PAT and Coregistered modes have been achieved and this frame rate is only limited by our laser repetition frequency.

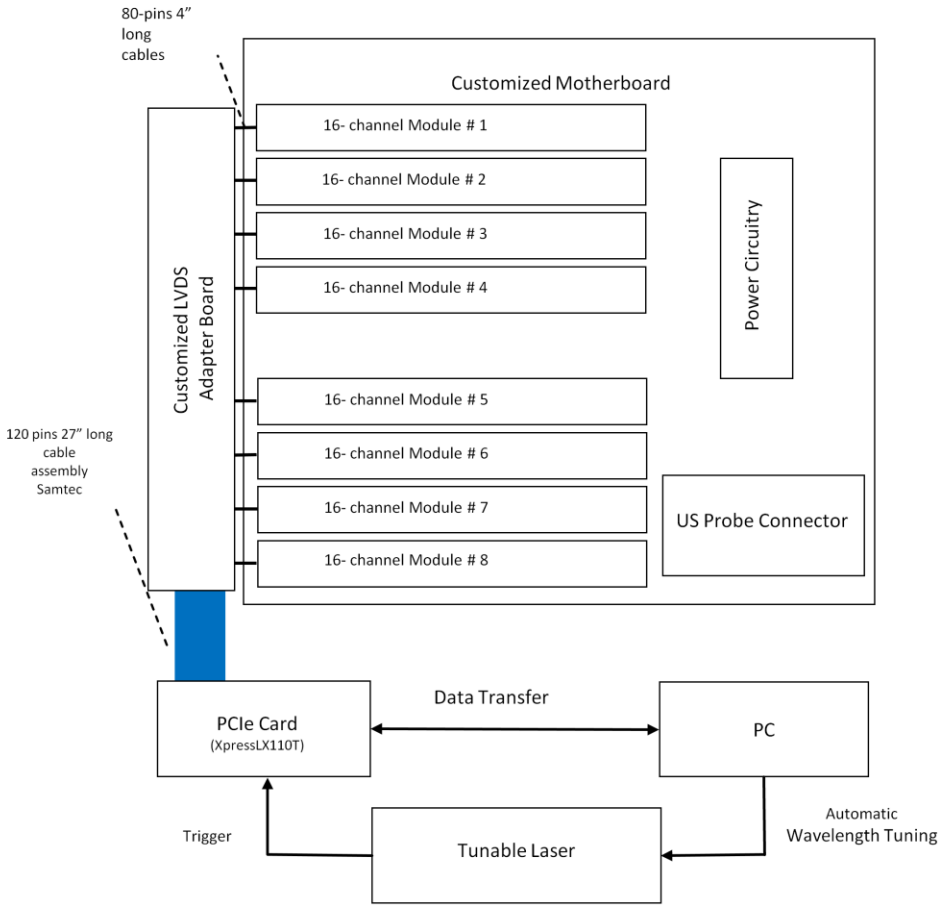


Figure 3.9 The overall block diagram of the coregistered pulse-echo ultrasound (US)/PAT system. Each 16-channel module consists of five boards: a custom-built 16-channel Tx pulsars and Rx preamplifier board, two commercial 8-channel US-receiving boards, a Virtex-4 FPGA board for digital capturing and reconfigurable subprocessing, and a customized adapter PCB board. The adapter PCB connects the ADC signals of the two receiving boards to one module FPGA board and also connects the Tx control signals from the module FPGA to the Tx pulsars. Eight modules are plugged into the motherboard, which fans out all the 128 channels from the modules to the US probe connector.

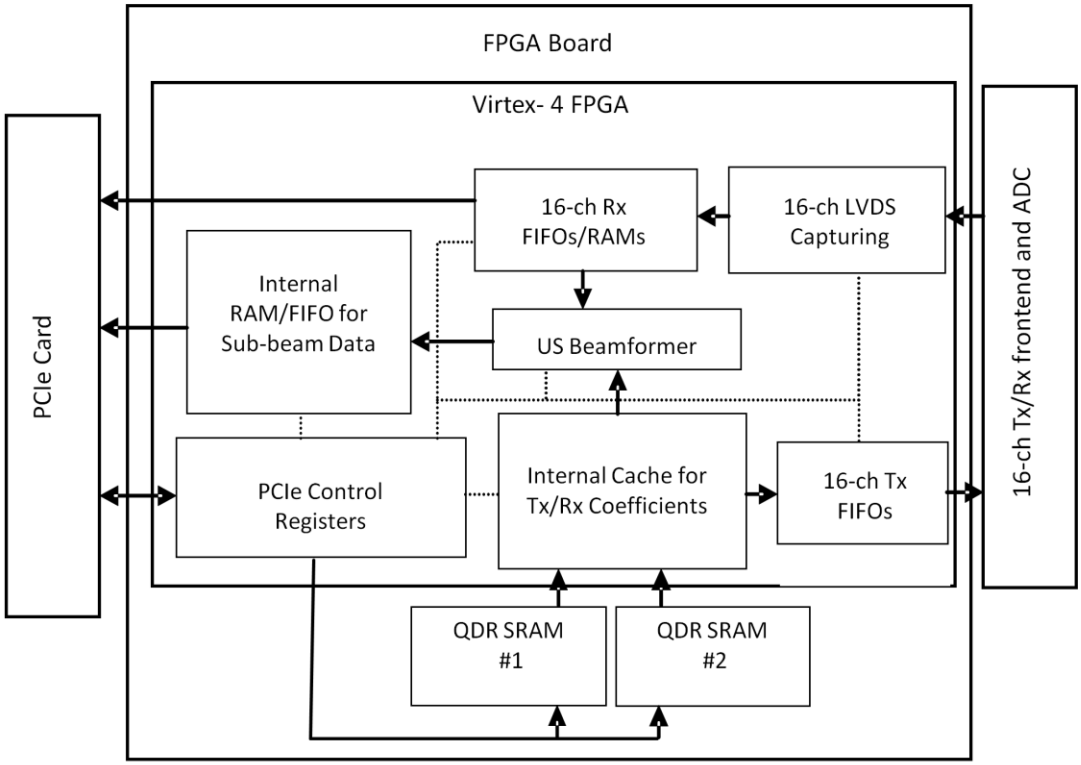


Figure 3.10 The block diagram of the internal structure of the module FPGA processor.

## 3.4 Automatic Wavelength Tuning

In clinical application, it is critical that we finish PAT DAQ as quick as possible. Previous sections have already introduced the techniques details to increase our imaging frame rate. It is helpful to co-register US and PAT images and to reduce the motion artifacts caused patient's inspiration. Meanwhile, we wish to get more information by using multiple laser wavelengths, such as oxygen saturation level inside tissues. This requires us to tune the laser to certain wavelength as fast as possible. The laser in this second version of US/PAT system is a tunable-wavelength Ti:Sapphire (Symphotics TII, LS-2211, Camarillo, California) optically pumped by a Q-switched Nd:YAG (Symphotics TII, LS-2134) , which delivers 20-ns pulses at a 15-Hz repetition rate with 20 mJ/pulse at the imaging wavelength of 750 nm. Aside the main part

of laser system, it has an accessory part to control the transmitting wavelength via a serial port. This wave length control unit is based on a microcontroller which communicates with PC by a serial port. PC can send the destination wavelength which is encoded in an integer index to microcontroller where this index is decoded to actual wavelength tuning. In most cases, the useable wavelength range for tissue photoacoustic imaging is from 700 to 900nm. We calibrate the laser system with spectrometer to set up an <index, wavelength> map by discrete wavelengths, such as 700nm to 900nm with 5 nm intervals. After getting this <index, wavelength> map, a polynomial interpolation is conducted to estimate the index of every integer wavelength from 700 to 900 nm to get a denser map. This new map is hard-coded in our C/C++ GUI program. In this way, the PAT program is able to tune the wavelength to any integer wavelength with a high accuracy and low latency. In clinical application, we usually don't need any fractional wavelength but integer wavelength. If a fractional wavelength is needed, a linear interpolation of its two nearest neighbor's wavelengths is used to estimate the index for the specific fractional wavelength. Table 3.1 lists index for wavelength from 689 nm to 946nm.

Table 3.1 Mapping of microcontroller index to laser wavelength (688nm to 947nm)

| λ | index | λ | index | λ | index | λ | index |
|---|---|---|---|---|---|---|---|
| 688 | 1940 | 753 | 7735 | 818 | 12139 | 883 | 15424 |
| 689 | 2067 | 754 | 7810 | 819 | 12195 | 884 | 15472 |
| 690 | 2192 | 755 | 7900 | 820 | 12250 | 885 | 15521 |
| 691 | 2313 | 756 | 8010 | 821 | 12303 | 886 | 15569 |
| 692 | 2431 | 757 | 8141 | 822 | 12357 | 887 | 15617 |
| 693 | 2545 | 758 | 8283 | 823 | 12410 | 888 | 15663 |
| 694 | 2654 | 759 | 8422 | 824 | 12463 | 889 | 15710 |
| 695 | 2758 | 760 | 8544 | 825 | 12516 | 890 | 15755 |
| 696 | 2856 | 761 | 8642 | 826 | 12569 | 891 | 15799 |
| 697 | 2948 | 762 | 8720 | 827 | 12623 | 892 | 15842 |
| 698 | 3033 | 763 | 8782 | 828 | 12677 | 893 | 15883 |
| 699 | 3112 | 764 | 8830 | 829 | 12731 | 894 | 15923 |
| 700 | 3184 | 765 | 8869 | 830 | 12786 | 895 | 15961 |
| 701 | 3250 | 766 | 8902 | 831 | 12842 | 896 | 15998 |
| 702 | 3312 | 767 | 8933 | 832 | 12898 | 897 | 16033 |

| | | | | | | | |
|---|---|---|---|---|---|---|---|
| 703 | 3369 | 768 | 8966 | 833 | 12954 | 898 | 16069 |
| 704 | 3423 | 769 | 9004 | 834 | 13012 | 899 | 16109 |
| 705 | 3475 | 770 | 9049 | 835 | 13069 | 900 | 16155 |
| 706 | 3530 | 771 | 9103 | 836 | 13128 | 901 | 16212 |
| 707 | 3599 | 772 | 9165 | 837 | 13186 | 902 | 16276 |
| 708 | 3694 | 773 | 9235 | 838 | 13244 | 903 | 16345 |
| 709 | 3824 | 774 | 9312 | 839 | 13301 | 904 | 16415 |
| 710 | 4000 | 775 | 9396 | 840 | 13357 | 905 | 16483 |
| 711 | 4222 | 776 | 9488 | 841 | 13411 | 906 | 16546 |
| 712 | 4443 | 777 | 9585 | 842 | 13464 | 907 | 16603 |
| 713 | 4609 | 778 | 9686 | 843 | 13515 | 908 | 16655 |
| 714 | 4713 | 779 | 9787 | 844 | 13564 | 909 | 16702 |
| 715 | 4770 | 780 | 9884 | 845 | 13611 | 910 | 16745 |
| 716 | 4799 | 781 | 9973 | 846 | 13657 | 911 | 16784 |
| 717 | 4816 | 782 | 10051 | 847 | 13703 | 912 | 16820 |
| 718 | 4840 | 783 | 10118 | 848 | 13750 | 913 | 16854 |
| 719 | 4887 | 784 | 10175 | 849 | 13797 | 914 | 16885 |
| 720 | 4976 | 785 | 10225 | 850 | 13847 | 915 | 16914 |
| 721 | 5119 | 786 | 10270 | 851 | 13899 | 916 | 16943 |
| 722 | 5295 | 787 | 10311 | 852 | 13954 | 917 | 16971 |
| 723 | 5469 | 788 | 10351 | 853 | 14013 | 918 | 16998 |
| 724 | 5608 | 789 | 10391 | 854 | 14075 | 919 | 17027 |
| 725 | 5710 | 790 | 10434 | 855 | 14141 | 920 | 17055 |
| 726 | 5781 | 791 | 10481 | 856 | 14208 | 921 | 17084 |
| 727 | 5830 | 792 | 10535 | 857 | 14276 | 922 | 17114 |
| 728 | 5866 | 793 | 10595 | 858 | 14342 | 923 | 17144 |
| 729 | 5898 | 794 | 10660 | 859 | 14407 | 924 | 17175 |
| 730 | 5932 | 795 | 10729 | 860 | 14468 | 925 | 17206 |
| 731 | 5979 | 796 | 10799 | 861 | 14524 | 926 | 17238 |
| 732 | 6045 | 797 | 10870 | 862 | 14576 | 927 | 17270 |
| 733 | 6129 | 798 | 10939 | 863 | 14623 | 928 | 17303 |
| 734 | 6223 | 799 | 11007 | 864 | 14666 | 929 | 17336 |
| 735 | 6318 | 800 | 11070 | 865 | 14706 | 930 | 17370 |
| 736 | 6408 | 801 | 11131 | 866 | 14744 | 931 | 17404 |
| 737 | 6483 | 802 | 11190 | 867 | 14779 | 932 | 17439 |
| 738 | 6540 | 803 | 11247 | 868 | 14813 | 933 | 17474 |
| 739 | 6608 | 804 | 11303 | 869 | 14846 | 934 | 17510 |
| 740 | 6688 | 805 | 11358 | 870 | 14878 | 935 | 17546 |
| 741 | 6778 | 806 | 11414 | 871 | 14911 | 936 | 17583 |
| 742 | 6874 | 807 | 11471 | 872 | 14945 | 937 | 17620 |
| 743 | 6972 | 808 | 11530 | 873 | 14980 | 938 | 17658 |

| | | | | | | | |
|---|---|---|---|---|---|---|---|
| 744 | 7070 | 809 | 11590 | 874 | 15017 | 939 | 17696 |
| 745 | 7165 | 810 | 11652 | 875 | 15056 | 940 | 17734 |
| 746 | 7256 | 811 | 11714 | 876 | 15098 | 941 | 17773 |
| 747 | 7341 | 812 | 11777 | 877 | 15141 | 942 | 17813 |
| 748 | 7420 | 813 | 11840 | 878 | 15186 | 943 | 17853 |
| 749 | 7491 | 814 | 11902 | 879 | 15232 | 944 | 17893 |
| 750 | 7554 | 815 | 11964 | 880 | 15279 | 945 | 17934 |
| 751 | 7613 | 816 | 12024 | 881 | 15327 | 946 | 17975 |
| 752 | 7671 | 817 | 12082 | 882 | 15375 | 947 | 18017 |

Wavelength tuning thread

As mentioned in previous sections, there are two threads created for DAQ and data processing respectively. When we start the wavelength tuning, especially automatically scan from one wavelength (e.g., 740nm) to another wavelength (e.g., 830nm) with certain interval (e.g., 10nm), a third thread is created for the controlling of program. It works by simulating user's manual input: At first, it acquires current index (wavelength), then pause both DAQ and processing threads, tune the wavelength to the starting wavelength, 740nm, in this case. It sleeps the program for a while (2s) then continues the suspended DAQ and processing threads. After finishing DAQ and processing at one wavelength for preset frames (e.g., 10 frames), wavelength tuning thread will pause DAQ and processing threads again and change the index to go to next wavelength. This procedure is repeated until the end wavelength is reached. In this way, we can scan multiple wavelengths in a short period with minimal human inputs, which will help to reduce the influence of patient motion during the scan.

## 3.5 Laser Energy Fluctuation Compensation

Though the difference of two adjacent laser pulses is almost negligible, as time goes by, there may be a shift in the trend of laser pumped energy even though we don't tune the wavelength of transmitting laser. Meanwhile, when we tune laser's wavelength, the pump energy

also changed. The change of pump energy caused by stability of laser system or wavelength tuning should be compensated when we do quantitive analysis of PAT data, for example, $S_{O2}$ calculation. The interpolated envelope of certain frame at certain pixel should be divided by the laser pump energy of the same frame before we use it for $S_{O2}$calculation. There are two main methods to record the pump energy of laser pulses: (1) photodiode (2) secondary single element ultrasound probe using PA effect. Laser pulses can be split into two parts (95% and 5%). The small portion can be measured either directly by photodiode or indirectly by a single element ultrasound transducer with same or similar center frequency of the US transducer for PE and PAT imaging. In most cases, the 5% beam is hard to be completely coupled into the small receiving rectangle of photodiode because of its wide beam width. In our real-time PE/PAT system, we choose the second solution: single element ultrasound transducer. The main transducer is based on element array and it is used for measurement of photoacoustic waves from our target tissue. One single element with big enough receiving aperture ultrasound transducer is used to measure the energy of this 5% portion of laser pulses. This 5% laser pulsed is shined on the surface of the single element transducer which will cause this single element transducer to generate photoacoustic signals. With appropriate amplification and filtering circuits, the integrated photoacoustic energy can be calculated by integrating the generated PA wave forms. Ideally, this single element transducer should have the same acoustic properties as the element in the array of main transducer (center frequency, bandwidth). In terms of DAQ, single element ultrasound transducer has a big advantage over the photodiode solution. The laser pulse width of the laser system is about 15 ns. To acquire the waveform of this laser pulse width, we need a very high sampling frequency (GHz) to capture its wave form. The single element ultrasound transducer converts laser to ultrasound and its own bandwidth limits the frequency of receiving wave form. Usually the clinical ultrasound transducer's center frequency is less than 10MHz; 100MHz sampling frequency is fast enough for ultrasound DAQ. In the real-time PE/PAT system, we

choose the single element transducer to compensate laser pumped energy because of the big receiving aperture of and less costly DAQ.

## 3.6 Imaging Probe

In terms of light delivery, it is important that we can deliver as much as possible light into tissues and keeps the fluence as uniform as possible. To get high SNR PAT signal, we wish to tune the input energy as high as possible. However, it is not practical in clinical case. There is a maximum permissible exposure (MPE) at certain wavelength. For example, the MPE at 750nm is 25mJ/cm$^2$ according to ANSI standard[34]. On the other hand, we also wish the fluence be as uniform as possible. On average, the thickness of vagina muscle wall between ultrasound transducer to ovary is about 1cm. This muscle wall can act as a natural optical diffusive plate which scatters input photons. So the input pattern of illumination is not necessarily uniform at the surface of human skin. Reference 35 shows the first version of probe design for ovarian cancer detection. The probe consists of 36 fibers of 200 micron core diameter each that are distributed around a commercial transvaginal ultrasound transducer, and housed in a protective shield (Figure 3.11).

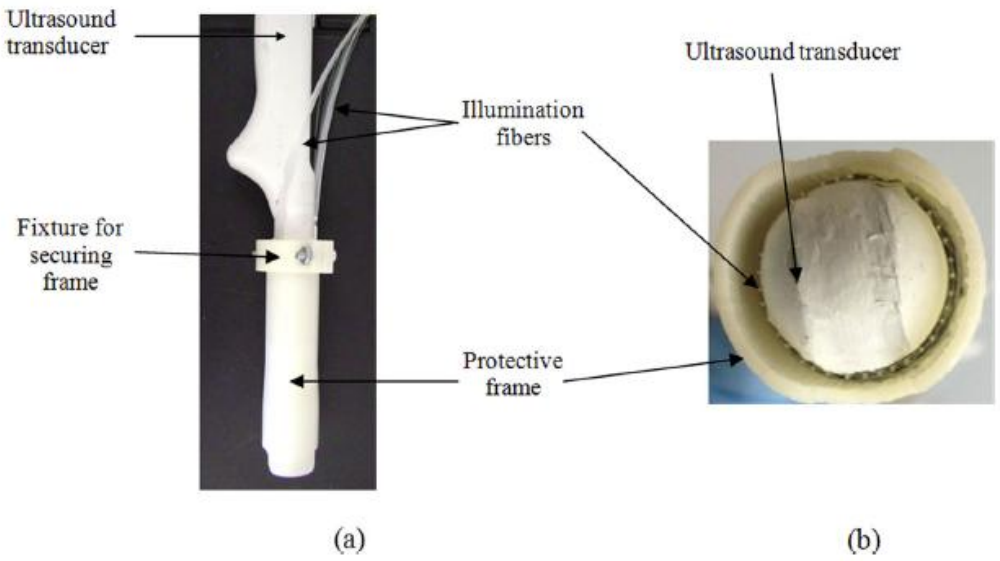


Figure 3.11 (a) Photograph of the side-view of the prototype coregisterd PE/PAT imaging probe. (b) Photograph of the bottom-view of the same probe showing the ultrasound transducer, illumination fibers, and protective cover (adapted from Reference 35).

The light fluence delivered by the probe on the tissue surface is about 17 mJ/cm$^2$, and is below the MPE of 24 mJ/cm2 at the 750 nm wavelength used for imaging. Mento Carlo simulation shows after 1cm the fluence is almost uniform. In order to evaluate this effect quantitatively, Reference 35 defined a Merging factor (M) as following:

$$M = (\text{MaxFluence} - \text{CenterFluence}) / \text{MaxFlence}.$$

This factor, M, is calculated for each depth using different source configurations and the result is shown in Figure 3.12. It can be seen that M approaches zero when the beam of different sources merged in the center. It is clear that the beams merge faster by increasing the number of sources.

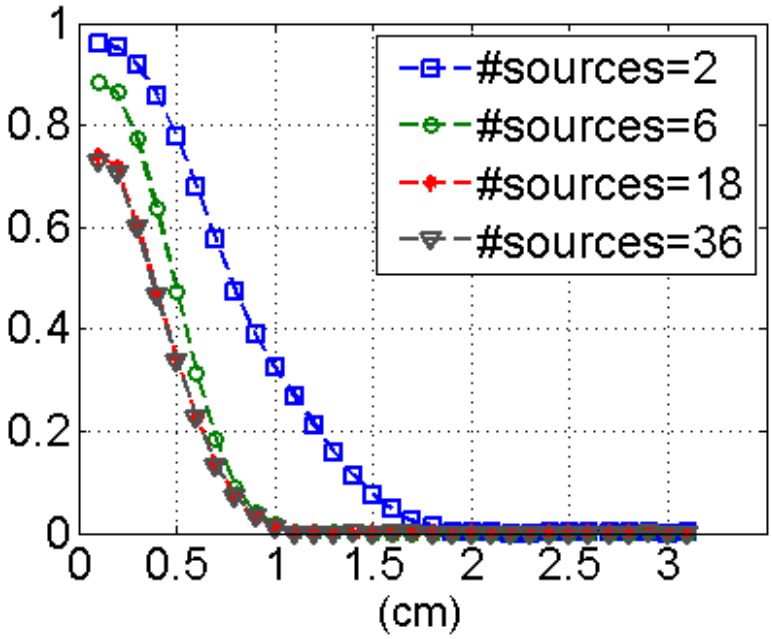


Figure 3.12 Calculated Merging factor versus depth (adapted from Reference 35).

However, because of the complexity of this probe design, it is quite easy to break these fiber bundles. To overcome this pitfall and improve the light delivery efficiency, Reference 36 gives us an alternative design. In this design, instead of fiber bundles, only four multi-mode optical fibers are used. The coupling efficiency between laser system and optical fibers is improved by using a lens-array based configuration. The lens array consists of four cylindrical lenses that couple the laser beams into four 1-mm-core multi-mode optical fibers with optical coupling efficiency of ~87%. The feasibility of the lens array was investigated by simulating the lenses and laser beam profiles using Zemax. The lens array design was first performed by simulating four cylindrical lenses in Zemax. In order to split a laser beam into four spots, two cylindrical lenses were vertically placed in front and the other two horizontally arranged behind (rotated 90°) with respect to the front lenses, as shown in Figure 3.13(a). In the experimental setup of the PAT imaging, the laser light propagates through the single homemade lens array that consists of four cylinder lenses (12.5mm H x 25mm L x 150mm FL Cylinder Lens VIS-NIR

Coating, Edmund Optics PCX). The lens array splits the incoming incident light into four beams. Each beam is then directed to couple into a 1mm-core optical fiber with a numerical aperture (NA) of 0.48. The optical coupling efficiency is determined from the ratio of the measured total energy output from the four fibers to the total energy incident at their input end faces, and is ~87%. The illumination fibers are then affixed to a compact photoacoustic/ultrasound imaging probe. The inner surface of the sheath and the outer surface of the ultrasound transducer are covered with an aluminum material having a reflection coefficient of 85% at 750nm for high-intensity light output. The laser source delivered 20ns pulses at 15Hz repetition rate with 20mJ/pulse at the imaging wavelength of 750nm.

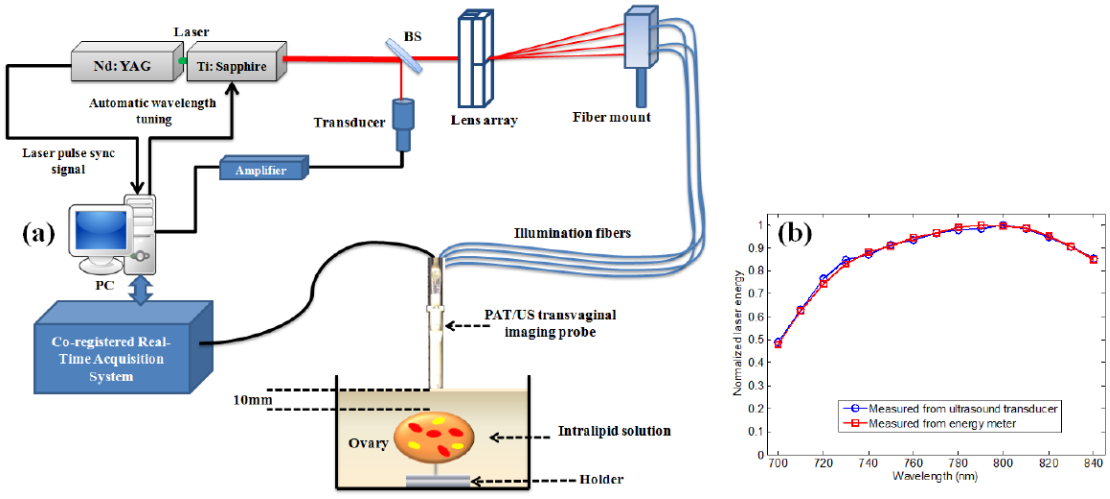


Figure. 3.13. (a) Experimental setup for *ex vivo* co-registered photoacoustic/ultrasound imaging. (b) Normalized laser output energy measured with single element ultrasound transducer and energy meter[36].

## 3.7 Result

### 3.7.1 Result of DSP-based US/PAT System

1) Phantom experiment of ink tube

We imaged a polyethylene tubing with a 0.58 mm inner diameter fixed to a plastic frame forming three parallel segments with a separation of approximately 1 cm, as shown in Figure 3.14; A 1.3-MHz 64-channel phased-array ultrasound transducer was placed facing the open side of the

frame. Both the frame and the transducer were immersed in a calibrated intralipid solution of 0.03 $cm^{-1}$ absorption coefficient and 6 $cm^{-1}$ reduced scattering coefficient at a depth of 1 cm, where the laser beam was expanded over the tubing area, as shown in Figure 3.14. Initially, the tubing was empty and only the ultrasound image (gray scale) showed acoustic contrast. At this point the photoacoustic image (color scale) showed no contrast because the tubing was almost transparent to light. Next, a black Indian ink was injected into the tubing, as shown in Figure 3.14, and the superimposed photoacoustic images revealed local optical contrast of each segment, one by one, as more ink was injected. For this experiment, the photoacoustic signal was averaged 7 times with the 15-Hz laser tuned at a wavelength of 740 nm; the achieved speed with this number of averages is around 0.5 co-registered frame/s.

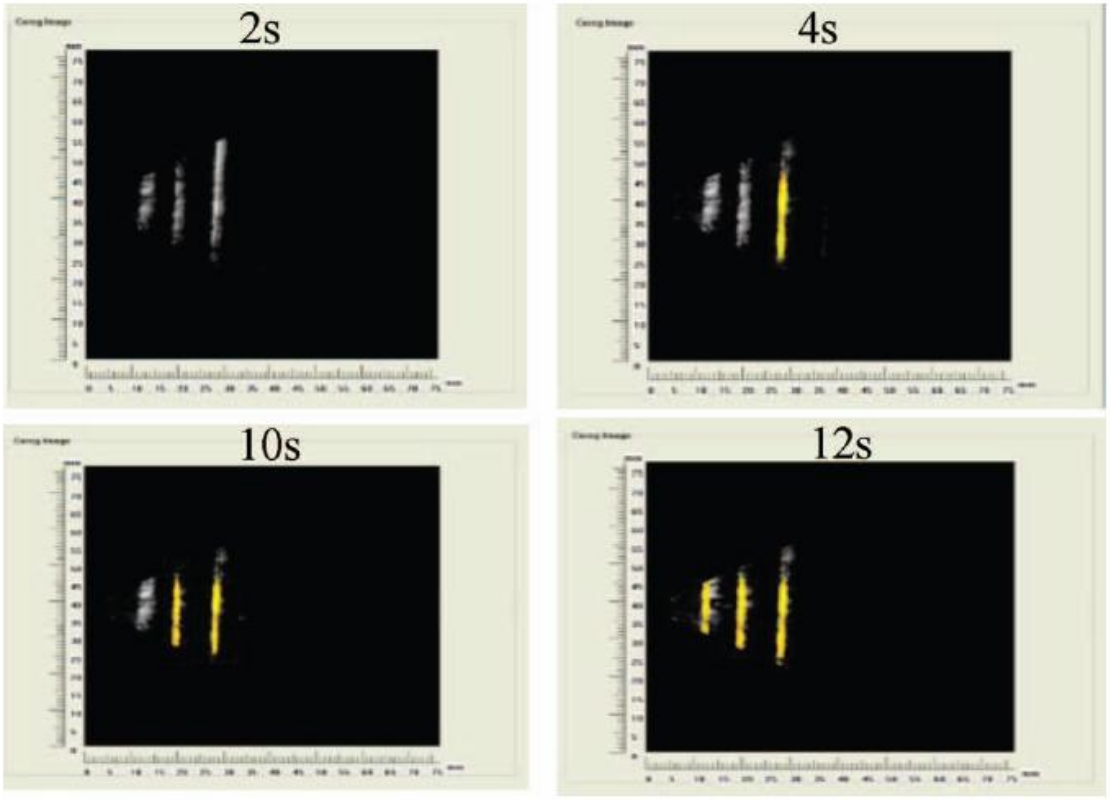


Figure 3.14 The dynamics of filling the tubing phantom with ink[17].

There is another phantom experiment in Reference 35, which is imaging of polyethylene tubing filled with the blood of a mouse that mimicked a blood vessel. The tube had inner and outer diameters of 0.86 mm and 1.27 mm respectively. All the images were taken at a depth of 1cm below the transducer, in intralipid solution having 4 $cm^{-1}$ scattering coefficient and 0.02 $cm^{-1}$ absorption coefficient. Figure 3.15 shows in log-scale the photoacoustic images of the blood-filled tube and is displayed using 15 dB dynamic range. The two lines seen are the front and back of the tube. The photoacoustic signal in the time-domain from a cylindrical object like the tube shows up as a characteristic "N-shape" pulse, when picked up with a very wide-band ultrasound transducer. However, because the transducer that we used had a limited bandwidth, only the two positive and negative peaks of the N-shape pulse is observed. These peaks correspond to the two lines that are seen in the photoacoutic image of the tube. The image in Figure 3.15(a) was taken with only intralipid layer between the tube and the probe. The maximum signal-to-noise ratio (SNR) for this image is 27, whereas the mean is 21. This is compared to the image obtained when a piece of chicken breast layer of about 1 cm thickness was used to cover the entire front face of the probe (Figure 3.15(b)). It is seen that the tube is clearly visible with the addition of the chicken layer. The maximum SNR dropped to 22, and mean SNR to 14, after placement of the chicken layer. "Maximum SNR" in this context is defined as the highest SNR that was obtained among the 64 acquired RF channel data from the transducer elements, and the "mean SNR" refers to the SNR averaged over all the 64 RF data.


Figure 3.15 Photoacoustic images of the polyethylene tubing filled with blood. (a) is the image with only intralipid layer, (b) is the same image but with about 1 cm chicken breast layer covering the front of the probe[35].

2) Mouse Experiment with Dynamics of ICG Injection

The *in vivo* imaging capability of the 64 channel DSP-based system is demonstrated using a mouse tumor model grown in the right mammary pad[17]. A water bath was placed between the tumor and the ultrasound transducer as a coupling medium. The laser beam illuminated the tumor through the coupling medium from one side of the ultrasound transducer, as shown in Figure 3.16. The system gain was also set to 50 dB, and both PE and PAT parts of the images were normalized to their own peaks with 40 dB dynamic range. All experiments were performed under anesthesia by the inhalation of 1.5% to 2% isoflurane. The animal protocol was approved by the Institutional Animal Care and Use Committee of University of Connecticut. Two sets of experiments were performed. In the first set of experiments, tumor uptake and dye wash out time was monitored for about 80 min after injection of ICG, which is an optical contrast agent. The dye concentration is 100 μM, and the illumination was done at 740 nm, which matches the peak absorption of the dye. In about 5 to 6 min, the maximum photoacoustic signal in the tumor area was increased by about 70 to 80% and areas of the tumor showed more filling. Figure 3.17 shows the normalized maximum photoacoustic signal,

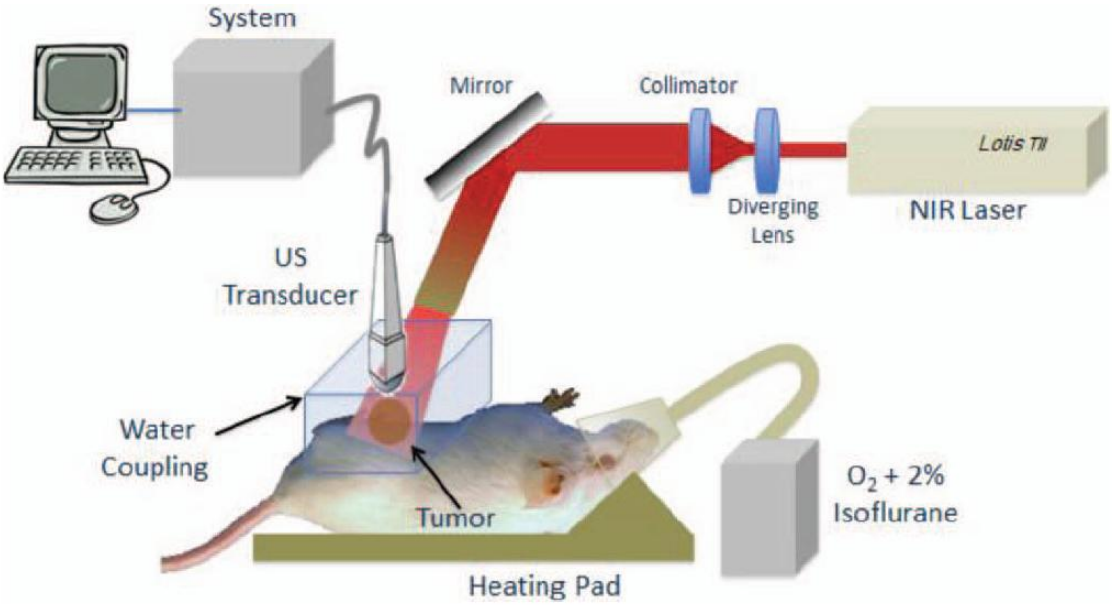


Figure 3.16 Mouse experiment setup[17].

which is normalized to the maximum PAT signal just before the injection, from the tumor area. The maximum PAT signal gradually increased in the first 3.5 min after injecting ICG, after that, it started to wash out slowly from the blood stream. The fluctuations in the PAT signal are likely due to the cardiovascular dynamics of the mouse. Furthermore, Figure 3.18 shows how the area of the tumor is more filled with the photoacoustic contrast 3.5 min after injection compared with the image before injection. It is noted that the laser pulse energy was monitored during the imaging process to compensate for the drift of the laser energy per pulse. The compensation was done by adding a transparent flat piece of glass in the path of the laser beam at about 30 °angle of incidence, which reflected a small fixed percentage of the laser light beam to an energy meter. The energy meter output was recorded and pre-calibrated with phantom experiments such that the peak PAT signal is proportional to the energy of the laser pulse (with ± 10% maximum uncertainty over 2 h period), and then synchronized with the PC acquisition software. Note also that the mouse temperature was assumed to be constant because a heating pad was used throughout the experiment.

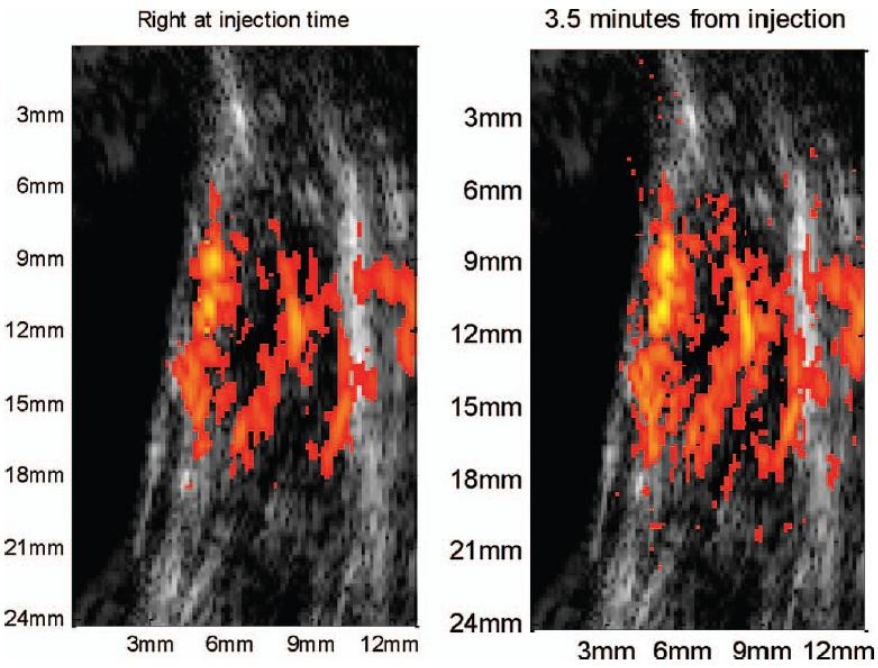


Figure 3.17 (left) The co-registered images at injection time, and (right) 3.5 minutes after injection; the photoacoustic tomography (PAT) parts of the images were normalized to the same value with 20 dB dynamic range[17].

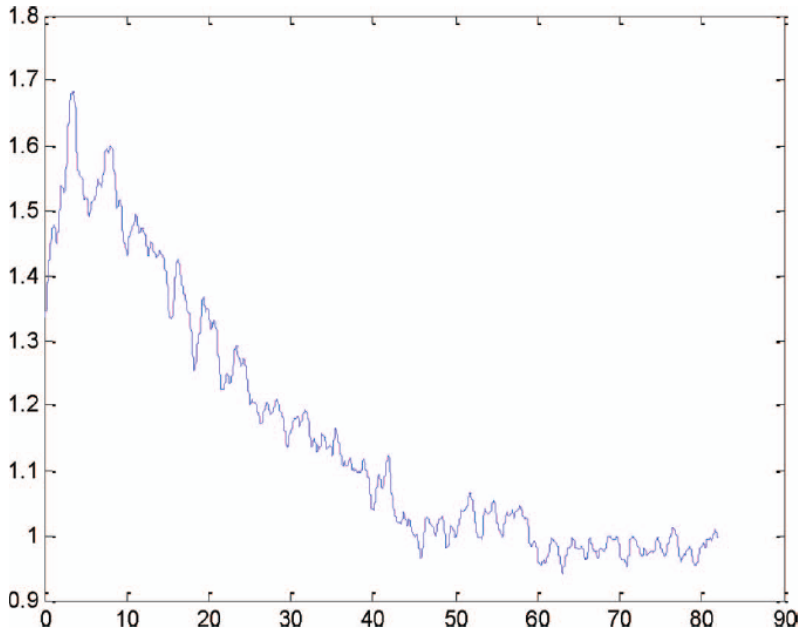


Figure 3.18 The maximum photoacoustic signal in tumor area right after injection of Indocyanine green (ICG) of 100 μM concentration, normalized to the maximum photoacoustic signal at the time of injection[17].

In the mouse model experiments, the wavelength of the laser was manually scanned from 705 to 835 nm during a 30-s *in vivo* imaging session. Shown in Figure 3.19 are two images selected at 745 and 835 nm, and the corresponding co-registered image showing the percentage of oxygen saturation of the blood hemoglobin within the tumor area. The model for oxygen saturation approximation is introduced in section 3.2.4. It is computed with gradient descent parametric fitting totaling 14 measurements from 705 to 835 nm with about a 9-nm step.

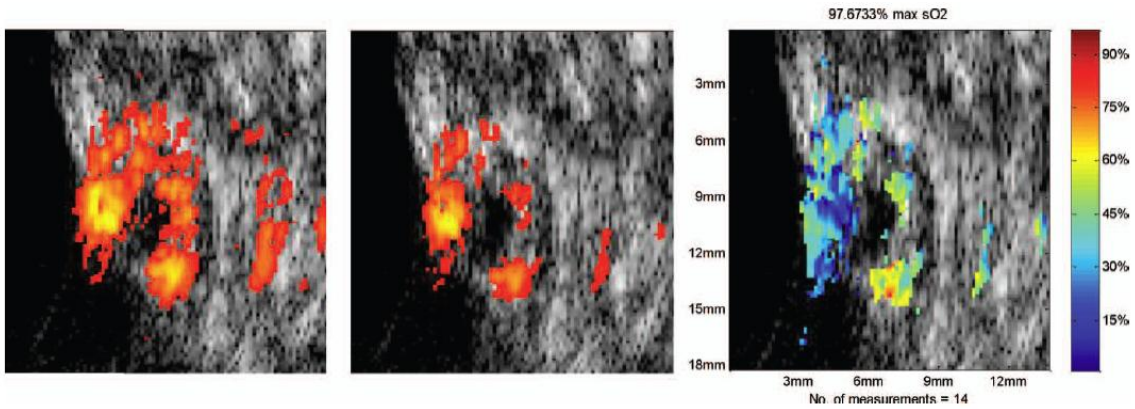


Figure 3.19 Co-registered photoacoustic tomography (PAT) images selected at (left) ~745 nm, and (middle) ~835 nm, showing different light absorption distributions over the tumor area. (right) The co-registered oxygen saturation image shows higher blood oxygen saturation at the edge compared to the core area. The actual image size is 1.8 × 1.35 cm.[17]

3) ex-vivo ovary experiment

To avoid possible violation of data use, ex-vivo ovary experiment is not shown in this dissertation. For more details, readers are encouraged to read Reference 35.

## 3.7.2 Result of PCIe-based System[37]

There are three sets of experiments performed on the PCIe-based US/PAT system. The first set of experiments was performed on a thin black thread to obtain the system lateral resolution and axial sensitivity. The second set of experiments was conducted using a tumor-

bearing mouse to demonstrate the real-time imaging capability of the system. The third set of experiments was performed on ex-vivo malignant and normal ovaries to demonstrate the diagnostic imaging capability of the system. The ovaries were freshly excised after an oophorectomy at the UCONN Health Center. Note that the light delivery system for mouse experiment was still the fiber bundle configuration in Reference 35 (Figure 3.20).

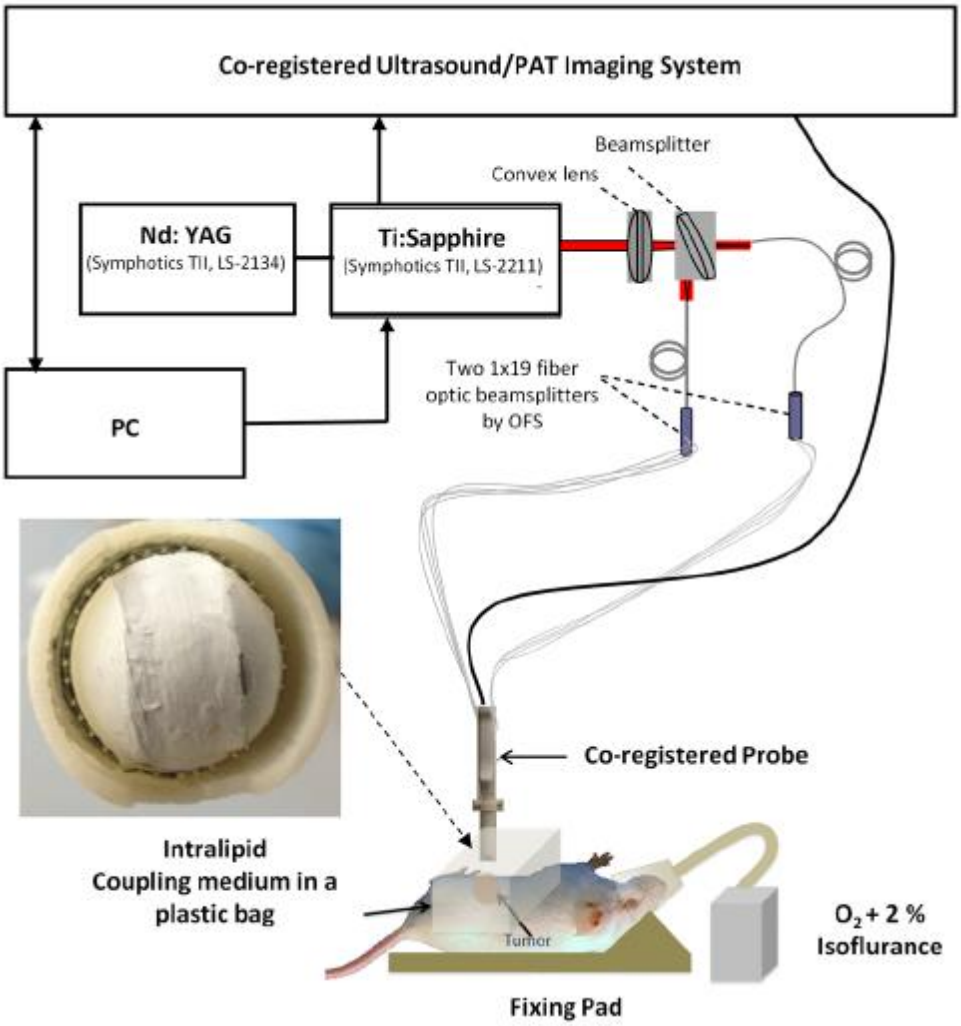


Figure 3.20 Light delivery system and experimental setup of *in vivo* tumor-bearing mouse.

To obtain the lateral resolution of the PCIe-based system, a 100-μm diameter black thread was placed in a water tank at a 30-mm depth with its orientation perpendicular to the

imaging plane. The lateral profiles of pulse-echo US and PAT were measured and are shown in Figure 3.21(a). Additionally, the maximum amplitude of the beam envelope in the PAT mode was recorded and the system noise was estimated from the root mean square value of the beam envelope when laser transmission was disabled. SNR or sensitivity of the black thread was calculated by 20*log10(max PAT envelope/system noise). By varying the distance between the black thread and the probe surface from 1 to 6.25 cm with an interval of 2.5 mm, the SNR at each depth is calculated and the curve is shown in Figure 3.21(b). The SNR dropped about 24 dB from 1 to 6 cm.

Since there is no theory for wideband transducer arrays, narrowband theory is used for the lateral resolution estimation.[38, 39] For a pulse-echo mode, the narrowband theory indicates that the beam profile follows a $\mathrm{sinc}^2(Dx/\lambda z)$ pattern in the lateral direction, where D is the effective size of the transducer in the lateral direction x, $\lambda$ is the US wavelength, and z is the depth. In the PAT mode, the lateral beam profile is given by a *sinc* function because of one-way reception only. Note that the 65 nearest elements were used in the beamforming, which resulted in an effective transducer array size D of 9.56 mm. The measured lateral resolutions of both pulse-echo and PAT modes agree well with theoretical values. From theory, full widths at half maximums of lateral beam profiles are 1.37 degrees in pulse-echo and 1.86 degrees in the PAT mode, while the measured values are 1.56 and 2.01 degrees, respectively.

The imaging setup for the *in vivo* animal experiment is shown in Figure 3.20. A calibrated intralipid of 0.03 $\mathrm{cm}^{-1}$ absorption coefficient and 3 $\mathrm{cm}^{-1}$ reduced scattering coefficient was placed in a plastic bag and used as a coupling medium. The tumor-bearing mouse was under anesthesia by inhalation of 1.5% isoflurane. The animal protocol was approved by the Institutional Animal Care and Use Committee of the University of Connecticut.

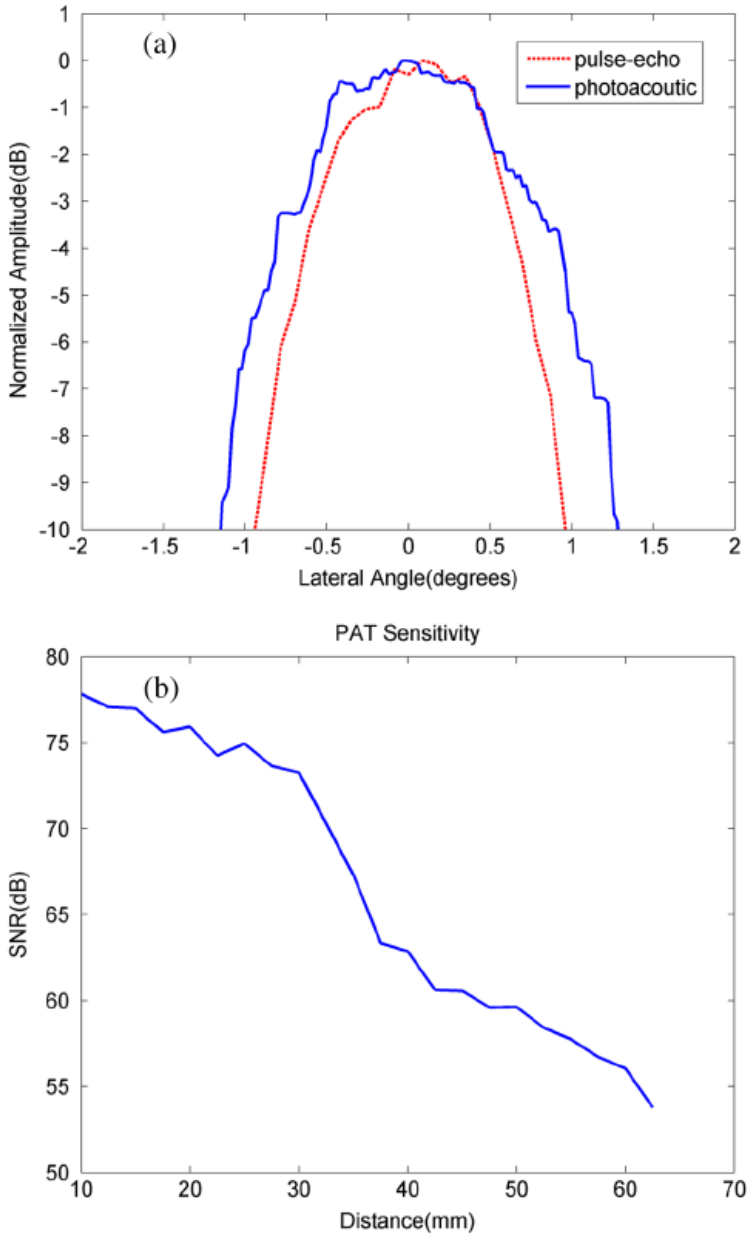


Figure 3.21 (a) Lateral profiles of pulse-echo US and PAT measured from a 100-μm black thread. (b) Axial sensitivity or SNR of PAT mode.

US imaging was performed first, and the real-time images (Real-time ultrasound scan for quick tumor area identification of tumor-bearing mouse [URI: http://dx.doi.org/10.1117/1.JBO.19.7.076020.1].) were used to locate the tumor area at 20 fps. Once the tumor area was identified, the Coregistered US/PAT scan was performed. Video 2(Real-time co-registered US/PAT scan of mouse tumor

area in5 fps [URI: http://dx.doi.org/10.1117/1.JBO.19.7.076020.2].) shows the Coregistered images and demonstrates the real-time imaging capability of the system while scanning the tumor area at 5 fps (averaging PAT acquisitions of three laser pulses). To guide the readers, white circles in both movies are included to mark the tumor area. For better visualization of the tumor vasculature content, all PAT images in Video 2 were normalized to the peak of the PAT beam envelopes of all frames during the scan procedure and are shown with a 15-dB dynamic range. The US images were shown with a 40-dB dynamic range. The wavelength used was 750 nm. In the second part of the experiment, the computer-controlled tunable Ti:Sapphire laser was used to obtain 10 PAT acquisitions at each wavelength from 745 to 835 nm with a 10-nm step size. After that, the co-registered US and oxy-saturation ($S_{O2}$) image was formed, where the $S_{O2}$ value was estimated from the relative ratio of oxy-hemoglobin to the total-hemoglobin concentrations, pixel-by-pixel , using the models developed in 3.2.4.Note that the measurements are constructed from the PAT value at each pixel normalized by the laser energy per pulse as measured at each wavelength. Also, the defined model assumes that the fluence profile over the imaging plane does not change over the selected wavelength window. The probe output optical energy was measured during data acquisition at each wavelength and used to compensate the PAT measurements before $S_{O2}$ estimation. Figure 3.22 shows the co-registered US/PAT images at 745, 805, and 835 nm wavelengths along with the resulting co-registered $S_{O2}$ image estimated from all 10 PAT wavelengths. Note that the tumor closer to the tissue surface appears to have a lower $S_{O2}$ as compared to the inside; this observation is quite similar to what we observed in a previous study.[17] Skin, in general, has higher absorption at lower wavelengths due to higher deoxygenated hemoglobin content and thus lower $S_{O2}$.

In the third set of experiments, a malignant and a normal ovary were imaged *ex vivo*. Each ovary was mounted on a supporting frame made of a transparent thin optical fiber net and was submerged inside a calibrated intralipid tank of 0.03 $cm^{-1}$ absorption coefficient and 4.0 $cm^{-1}$

reduced scattering coefficient. The ovary was located about 10-mm deep from the probe surface. The PAT signals of the ovaries were weaker than that of the black thread, thus an average of 64 laser pulses was used to improve the quality of images which reduced the PAT image rate to about 4 s per frame. To avoid possible violation of data use, images of ex-vivo ovarian tissues is not shown in this dissertation. For more details, readers are encouraged to read Reference 37.

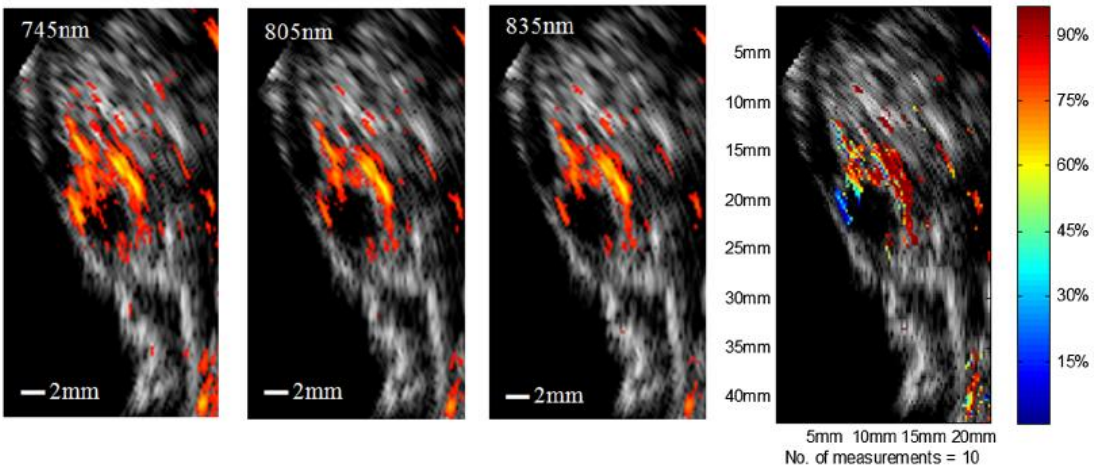


Figure 3.22 The first three images from left are coregistered US/PAT at different wavelengths (indicated in the upper left corners), the first image from right is a coregistered US/$S_{O2}$ image obtained using gradient descent estimation from 10 PAT acquisitions at 10 different wavelengths. US images are in grayscale and the tumor is shown as a round hypoechoic region. The PAT absorption images (first three) and $S_{O2}$ image are shown in color. The right color bar is the $S_{O2}$ scale.

## 3.8 Summary

This chapter is a combination of all the materials related to our real-time co-registered US/PAT system. Section 3.1 introduces the system development in other groups and the necessity of building our own US/PAT system and real-time capability. There were two versions of US/PAT system built in our lab. The first version, introduced in section 3.2 was based on DSP chip and Ethernet cable for data communication. The front end circuits for ultrasound

transmitting and receiving are controlled by module FPGAs which is responsible for transmitting time FIFO construction and ultrasound/PAT DAQ. In this version, PE and PAT mode are not fully synchronized. Co-registered mode is simply a sequential PE plus PAT mode. The data communication between modules FPGAs and DSP chip is via EMIF while DSP chip has Ethernet cable to transfer data to PC using TCP/IP sockets. In this section, advanced signal processing for ultrasound and PAT mode is discussed, which includes FFT based Hilbert transform, In-phase and Quadrature demodulation, circular convolution and acceleration of real number FFT. The model for oxygen saturation estimation is explained in 3.2.4 in details using least square root error fitting. To overcome the slow data transfer rate in our first version of US/PAT system, section 3.3 discuss some methods to promote the speed of imaging rate, which includes PCIe DMA data transfer, multi-threads technique and its implementation in C++ program (semaphore and producer/consumer problem). Section 3.4 formally introduces the design of the second version of US/PAT system which keeps the lower level module FPGAs designs, accelerate the data transfer rate between module FPGAs and PCIe FPGA by LVDS and solve the bottleneck of bulk data transfer between PCIe FPGA and PC. In lower level, the co-registered mode is optimized in which PE mode and PAT mode are done in a TDM fashion. In PC code, based on the DMA nature, multi-thread technique (producer/consumer model and semaphore) is implemented which allows PC and front end FPGAs to work in parallel. Section 3.4 presents the way to automatically control the wavelength of laser system, the third thread – wavelength tuning thread and its interaction with the previous sampling and processing threads. Section 3.5 introduces two methods to compensate long term laser pump energy trend shift: (1) photodiode (2) single element US transducer with big receiving aperture (PA effect). This compensation is necessary for long term PAT imaging (e.g., monitoring performance of contrast dye) and oxygen saturation level estimation. Two versions of imaging probe designs are simply introduced in section 3.6: fiber bundles and 4 fibers configuration. The latter one has better light delivery efficiency while fluence is under the MPE requirement so it is currently used for clinic data

collection. Results of two systems are shown in 3.7.1 and 3.7.2 respectively, including phantom experiment and mouse model. Section 3.7.2 also presents the later resolution and sensitivity of PAT mode of our second US/PAT system.

Currently, the first version of US/PAT system can achieve 1 (max 3 ) frame per second on average while the second one can hit 20 fps and 15 fps in PE mode and Coregistered mode respectively with reasonable dense beams (91 beams in 120 degrees). This real time capability makes it valuable to get the microvessel distribution for in-vivo ovary tissues in hand-holding situation because the motion artifacts are almost negligible when the imaging rate is 15 fps. The system also can perform automatic wavelength tuning to estimate $S_{O2}$ level using least square error fitting. The RF data and intermediate result in the reconstruction phase carry useful information for diagnosis of ovary tissue. It is possible to extract features from these data and develop model to aid the diagnosis of ovary tissue, which will be discussed later.

## References


1. L . V. Wang, "Ultrasound-mediated biophotonic imaging: A review of acousto-optical tomography and photoacoustic tomography," Dis. Markers, vol. 19, no. 2–3, pp. 123–138 (2003)

2. J. L. Prince and J. M. Links, Medical Imaging Signals and Systems. Upper Saddle River, NJ: Pearson Prentice Hall, ch. 10 and 11(2006).

3. S . Y. Emelianov, S. R. Aglyamov, J. Shah, S. Sethuraman, W. G. Scott, R. Schmitt, M. Motamedi, A. Karpiouk, and A. Oraevsky, "Combined ultrasound, optoacoustic and elasticity imaging," Proc. SPIE, vol. 5320, pp. 101–112(2004).

4 S . Y. Emelianov, S. R. Aglyamov, A. B. Karpiouk, S. Mallidi, S. Park, S. Sethuraman, J. Shah, R. W. Smalling, J. M. Rubin, and W. G. Scott, "Synergy and applications of combined ultrasound,

elasticity, and photoacoustic imaging," in IEEE Ultrasonics Symp., pp. 405–415 (2006).

5 S . A. Ermilov, T. Khamapirad, A. Conjusteau, M. H. Leonard, R. Lacewell, K. Mehta, T. Miller, and A. A. Oraevsky, "Laser optoacoustic imaging system for detection of breast cancer," J. Biomed. Opt., vol. 14, no. 2, art. no. 024007, (Mar./Apr ,2009).

6 A . Aguirre, P. Guo, J. Gamelin, S. Yan, M. Sanders, M. Brewer, and Q. Zhu, "Co-registered 3-D ultrasound and photoacoustic imaging system for ovarian tissue characterization," J. Biomed. Opt., vol. 14, no. 5, art. no. 054014 (2009).

7. A . Aguirre, Y. Ardeshirpour, M. Sanders, M. Brewer, and Q. Zhu, "Potential role of co-registered photoacoustic and ultrasound imaging in ovarian cancer/ detection and characterization," Transl. Oncol., vol. 4, no. 1, pp. 29–37 (2011).

8. X. L. Deán-Ben, V. Ntziachristos, and D. Razansky, "Statistical optoacoustic image reconstruction using a-priori knowledge on the location of acoustic distortions," Appl. Phys. Lett., vol. 98, no. 17, art. no. 171110 (Apr. 2011).

9. D . Modgil and P. J. La Rivière, "Image reconstruction in photoacoustic tomography with variable speed of sound using a higherorder geometrical acoustics approximation," J. Biomed. Opt., vol. 15, no. 2, art. no. 021308 (Mar. 2010).

10. B. T. Cox, S. Kara, S. R. Arridge, and P. C. Beard, "k-Space propagation models for acoustically heterogeneous media: Application to biomedical photoacoustics," J. Acoust. Soc. Am., vol. 121, no. 6, pp. 3453–3464 (2007).

11. J. J. Niederhauser, M. Jaeger, R. Lemor, P. Weber, and M. Frenz, "Combined ultrasound and optoacoustic system for real-time highcontrast vascular imaging in vivo," IEEE Trans. Med. Imaging, vol. 24, no. 4, pp. 436–440 (Apr. 2005).

12. S . Sethuraman, S. R. Aglyamov, J. H. Amirian, R. W. Smalling, and S. Y. Emelianov, "Development of a combined intravascular ultrasound and photoacoustic imaging system," in Proc. SPIE Photonics West, vol. 6086, pp. F1–F10 (2006).

13. P. Guo, J. Gamelin, S. Yan, A. Aguirre, and Q. Zhu, "Co-registered 3-D ultrasound and photoacoustic imaging using a 1.75D 1280-channel ultrasound system," Proc. SPIE, vol. 6437, art. no. 643713 (2007).

14. R . G. M. Kolkman, P. J. Brands, W. Steenbergen, and T. G. van Leeuwen, “Real-time in vivo photoacoustic and ultrasound imaging,” J. Biomed. Opt., vol. 13, no. 5, art. no. 050510 (Sep./Oct. 2008).

15. S . A. Ermilov, M. P. Fronheiser, H.-P. Brecht, R. Su, A. Conjusteau, K. Mehta, P. Otto, and A. A. Oraevsky, “Development of laser optoacoustic and ultrasonic imaging system for breast cancer utilizing handheld array probes,” Proc. SPIE, vol. 7177, art. no. 717703 (2009).

16. T. Harrison, J. C. Ranasinghesagara, H. Lu, K. Mathewson, A. Walsh, and R. J. Zemp, “Combined photoacoustic and ultrasound biomicroscopy,” Opt. Express, vol. 17, no. 24, pp. 22041–22046 (Nov. 2009).

17 . Alqasemi U., Li H., Aguirre A. and Zhu Q., "FPGA-based Reconfigurable Processor for Ultrafast Interlaced Ultrasound and Photoacoustic Imaging", IEEE Transaction on Ultrasonic, Ferroelectrics and Frequency Control ,59(7):1344-53(Jul ,2012)

18. Octal LNA/VGA/AAF/ADC and Crosspoint Switch: AD9272, Rev. C, Analog Devices, Inc., Norwood, MA,2007.

19. Evaluating the AD9272/AD9273 for Ultrasound Systems: Evaluation Board User Guide, UG001, Rev. 0, Analog Devices, Inc., Norwood, MA, 2009.

20. High Speed Converter Evaluation Platform: HSC-ADC-EVALC, Rev. 0, Analog Devices, Inc., Norwood, MA, 2007.

21. http://www.fftw.org/

22. Ultrasound Scan Conversion on TI’s C64x+ DSPs, http://www.ti.com/lit/an/sprab32/sprab32.pdf

23. https://en.wikipedia.org/wiki/Hilbert_transform

24. Marple, S. L. "Computing the Discrete-Time Analytic Signal via FFT." *IEEE Transactions on Signal Processing*. Vol. 47, pp. 2600–2603 (1999)

25. Ultrasound Scan Conversion on TI’s C64x+ DSPs, http://www.ti.com/lit/an/sprab32/sprab32.pdf

26.J. Laufer, C. Elwell, D. Delpy, and P. Beard, “In vitro measurements of absolute blood oxygen saturation using pulsed near-infrared photoacoustic spectroscopy: Accuracy and resolution,” Phys. Med. Biol., vol. 50, no. 18, pp. 4409–4428(2005).

27. X. Wang, Y. Pang, G. Ku, X. Xie, G. Stoica, and L. V. Wang, “Noninvasive laser-induced photoacoustic tomography for structural and functional in vivo imaging of the brain,” Nat. Biotechnol., vol. 21, no. 7, pp. 803–806 (Jul. 2003).

28. L . V. Wang, X. Wang, G. Ku, X. Xie, and G. Stoica, “High-resolution spectroscopic photoacoustic tomography for non-invasive functional imaging of small-animal brains in vivo,” in Second Asian and Pacific Rim Symp. Biophotonics, pp. 246–247(2004).

29. V. Tuchin and T. Optics, Light Scattering Methods and Instruments for Medical Diagnosis, 2nd ed., Bellingham, WA: SPIE Press(2000).

30. http://omlc.org/spectra/hemoglobin/index.html

31. https://en.wikipedia.org/wiki/PCI_Express

32. https://en.wikipedia.org/wiki/Multithreading_%28computer_architecture%29

33. https://en.wikipedia.org/wiki/Semaphore_%28programming%29

34. American National Standard for the Safe Use of Lasers, ANSI Z136 (Laser Institute of America, Orlando, Florida, 2007), pp. 1–2007.

35. P. D. Kumavor, U. Alqasemi, B. Tavakoli, H. Li, Y. Yang, X. Sun, E. Warych, and Q. Zhu, "Co-registered pulse-echo/photoacoustic transvaginal probe for real time imaging of ovarian tissue," J. Biophotonics 6(6-7), 475–484 (2013).

36. Hassan S. Salehi, Tianheng Wang, Patrick D. Kumavor, Hai Li, and Quing Zhu, "Design of miniaturized illumination for transvaginal co-registered photoacoustic and ultrasound imaging", Biomedical Optics Express, Vol. 5, Issue 9, pp. 3074-3079 (2014)

37. Umar Alqasemi, Hai Li, Guangqian Yuan, Patrick Kumavor, Saeid Zanganeh, and Quing Zhu, "Interlaced photoacoustic and ultrasound imaging system with real-time co-registration for ovarian tissue characterization", J Biomed Opt.;19(7):76020. doi: 10.1117/1.JBO.19.7.076020(Jul , 2014)

38. A. Aguirre et al., "Coregistered three-dimensional ultrasound and photoacoustic imaging system for ovarian tissue characterization," J. Biomed. Opt. 14(5), 054014 (2009).

39. J. L. Schwartz and B. D. Steinberg, "Ultrasparse, ultrawideband arrays," IEEE Trans. Ultrason. Ferroelectr. Freq. Control 45(2), 376–393 (1998).

# Chapter 4 Photoacoustic Imaging Enhanced by Indocyanine Green-conjugated Single-wall Carbon Nanotubes

Chapter 3 solved the real-time capability of US/PAT imaging system so it is convenient for physicians to detect patient ovaries using hand-held probe. However, usually the signal to noise (SNR) ratio of ovarian tissue is low and there is a necessity to develop contrast agent for photoacoustic imaging. In this chapter, a photoacoustic contrast agent that is based on bis-carboxylic acid derivative of Indocyanine Green (ICG) covalently conjugated to single-wall carbon nanotubes (ICG/SWCNT) is presented. Covalently attaching ICG to the functionalized SWCNT provides a more robust system that delivers much more ICG to the tumor site. The detection sensitivity of the new contrast agent in a mouse tumor model is demonstrated *in vivo* by our custom-built photoacoustic imaging system. The summation of the photoacoustic tomography (PAT) beam envelope, referred to as the "PAT summation," is used to demonstrate the post-injection light absorption of tumor areas in ICG- and ICG/SWCNT-injected mice. It is shown that ICG is able to provide 33% enhancement at approximately 20 min peak response time with reference to the pre-injection PAT level, while ICG/SWCNT provides 128% enhancement at 80 min and even higher enhancement of 196% at the end point of experiments (120 min on average). Additionally, the ICG/SWCNT enhancement was mainly observed at the tumor periphery, which was confirmed by fluorescence images of the tumor samples. This feature is highly valuable in guiding surgeons to assess tumor boundaries and dimensions *in vivo* and to achieve clean tumor margins to improve surgical resection of tumors.

## 4.1 Introduction

Indocyanine green (ICG) is a photosensitive dye with considerable absorption and fluorescence in the near-infrared (NIR) wavelength region.[1] It has negligible toxicity, and the U.S. Food and Drug Administration has approved its use for ophthalmic imaging, assessment of

cardiac output, and hepatic function.[2,3] ICG's desirable optical characteristics have motivated many studies, which utilize it as a sensitizer for photo-thermal therapy of tumors,[4] photodynamic therapy,[5] tissue welding,[6]estimation of burn depth,[7] and imaging vascularization and blood flow within breast tumors, skin, and the brain.[8–11] However, ICG is cleared rapidly from the bloodstream, and its total concentration decreases with a half-life on the order of 2 to 4 min.[12] Previous studies indicate that ICG exhibits nonspecific binding to blood proteins, such as albumin and high-density lipoproteins, and is finally eliminated from the general circulation by the renal system and the liver.[13,14] To overcome ICG's rapid circulation kinetics, other investigators developed several strategies, such as encapsulating it within poly(lactic-co-glycolic acid) or micelles, embedding it within a lipid suspension, and through noncovalent interaction with nanoparticles.[15–20]

It has been demonstrated that developing a delivery system for ICG that provides efficient dye loading increases the utility of ICG for diagnostic and therapeutic applications.[21] Within the family of nanomaterials, there is a great interest in the use of carbon-based nanostructures for various biomedical applications.[22] Carbon nanotube (CNT) has emerged not only as a new alternative and efficient transporter of therapeutic molecules, but also as an optical imaging agent owing to its strong optical absorption in the NIR region.[23] Drugs, antibodies, and nucleic acids could functionalize as single-wall CNTs (SWCNTs) to prepare an appropriate system for delivering the cargos to the cells and the organs. Additionally, the broad absorption spectrum of SWCNTs provides a wide range of optical wavelengths for imaging. The narrow absorption spectra of a number of contrast agents have restricted their use to a particular wavelength.[24,25]

Photoacoustic tomography (PAT) is an emerging modality that provides optical absorption contrast of biological tissues at ultrasound resolution.[26–29] In PAT, a short-pulsed laser beam is used to illuminate the tissue. Upon absorption of the light by the tissue, ultrasound waves are generated due to thermoelastic expansion. An array-based ultrasound transducer is used to receive the generated photoacoustic waves, which are used to reconstruct the images that show the light absorption distribution of the tissue. If the laser illumination has a wavelength within the NIR window from 600 to 900 nm, the tissue absorption is mainly due to hemoglobin, while water and other tissue constituents (e.g., fat) have low absorption. Furthermore, light scattering in NIR region is lower than that in the visible wavelength range allowing for deeper tissue penetration.[30] This makes PAT imaging in the NIR region an excellent tool to reveal the complex vasculature distribution or angiogenesis of tumors.

In order to enhance the contrast of PAT, several research groups have explored the use of exogenous ICG or CNT individually. Pramanik et al. used pure SWCNT as a contrast agent for photoacoustic mapping of the sentinel lymph node (SLN).[31] They successfully imaged the SLN *in vivo* with high contrast-to-noise ratio and good resolution. They showed that SWCNTs had a wideband optical absorption and generated PAT signals over a wavelength range of 740 to 820 nm. Thus, by tuning the light illumination wavelength to this region, the imaging depth can be maximized. Kim et al. used ICG-embedded nanoparticles that are incorporated with a cancer-specific target as a contrast agent for PAT.[17] Embedding ICG in nanoparticles improved the stability of ICG in aqueous solution as compared with free ICG. Their initial *in vitro* characterization results showed a high contrast and high efficiency for the agent to bind to prostate cancer cells. Further studies by Rajian et al. used perfluorocarbon emulations to encapsulate ICG, and keep it optically stable for use as a contrast agent for optical imaging.[32] The study by Wang et al. have found an effective application of Protamine-functionalized SWCNTs for stem-cell labeling and for *in vivo* Raman/magnetic resonance/photoacoustic triple-modal

imaging.[33] Their work revealed that SWCNTs with appropriate surface functionalization have the potential to serve as multifunctional nanoprobes for stem-cell labeling and multimodal *in vivo* tracking.

There are few reports in the literature that describe the use of CNT as a carrier of ICG for enhancing photoacoustic contrast. Recently, de la Zerda et al. reported a new sensitive CNT agent for photoacoustic imaging and demonstrated the performance of the agent in mice.[34] This contrast agent is based on attaching ICG to the surface of the nanotubes through $\pi - \pi$ stacking interactions. Additionally, this agent is conjugated with cyclic Arg-Gly-Asp (RGD) peptides to molecularly target the alpha(v)beta(3) integrins, which are associated with tumor angiogenesis.

In this chapter, we present a novel photoacoustic contrast agent that is based on bis-carboxylic acid derivative of ICG[35] covalently conjugated to the SWCNT (ICG/SWCNT). Using ICG/SWCNT as a contrast agent exhibits a much higher peak absorbance compared with plain SWCNTs. The performance of the new contrast agent in mouse tumor models is demonstrated *in vivo* using our custom-built co-registered ultrasound and photoacoustic imaging system.[36] Both ultrasound pulse-echo (PE) image and PAT image of the mouse are captured and stored throughout the experiments to provide the tumor morphology and light absorption distribution longitudinally. It is known that ultrasound probes tumor mechanical contrast and provides tumor morphology, while the PAT maps tumor angiogenesis and provides tumor functional information. Co-registered PE/PAT imaging is an excellent tool to diagnose ultrasonically identified lesions based on lesion vascular contrast provided by PAT. Post-processing of the PAT data shows approximately two times higher enhancement of ICG/SWCNT than ICG. This is further validated by fluorescence images of the excised tumor samples.

## 4.2 Materials and Methods

### 4.2.1 Functionalizing SWCNT

In the functionalization process, Pristine SWCNTs (Sigma-Aldrich, St. Louis, Missouri) were first immersed in a mixture of H2SO4 (98 vol %) and HNO3 (68 vol %) (3∶1) exposed to the ambient atmosphere. The SWCNTs were then immersed in an ultrasound bath (500 W) for 2 h. The chloridric acid was then added to the solution with slow agitation, followed by ammonium hydroxide until the solution was neutralized. The resulting solution was then filtered with a 0.22-mm cellulose acetate membrane. The SWCNTs were washed several times with deionized water to a pH of 5.5. The residue was dried in an oven at 60℃ for 18 h to obtain carboxylated CNTs(SWCNTs-COOH). Reaction of thionyl chloride with carboxyl-contained SWCNT (CNT–COOH) gave carbonyl chloride groups-functionalized SWCNTs (SWCNT-COCl), which is the intermediate product for further chemical functionalization. The SWCNT-COCl was treated with triethylenetetramine to generate SWCNT-NH2.[37]

### 4.2.2 Bis-Caboxylic Acid-ICG/SWCNT

Bis-caboxylic acid-ICG was covalently attached to amino-functionalized SWCNT via the conversion of the bis-caboxylic acid-ICG to the corresponding acid chloride using oxalyl chloride. Details that concern the preparation of our bis-caboxylic acid-ICG, referred to as ICG in the rest of the article, can be found in Reference 38. The acid chloride ICG was not isolated, but immediately treated with the amino-functionalized SWCNT (SWCNT-$NH_2$), heated in toluene at reflux for 1 h, and then stirred for an additional 5 h. The mass ratio of ICG to functionalized nanotube used was 3:1. The unbound ICG was removed from the solution through a 100-kDa centrifuge filter (millipore tube), followed by six washes with water. The unbound ICG compound passed through the filter dissolved in the water, while the insoluble SWCNT-bound

ICG remained. Covalent attachment was confirmed through Raman, ATR-IR spectroscopy, and TGA (data are not presented here). Absorption spectra of plain SWCNT and ICG/SWCNT were acquired from 600 to 800 nm in 1-mm cuvettes using the UV-Vis spectrometer (Varian Analytical Instruments, Walnut Creek, California). The spectra were acquired at a scan speed of 125 nm $min^{-1}$.

## 4. 2.3 Cell Line, Mice, and Histology

Our 4T1 Luc cells were regularly cultured at 37 ℃ with 5% CO2 in RPMI 1640 medium (Gibco, Grand Island, New York), supplemented with 10% FBS, 50 U⁄mL penicillin/streptomycin, 2 mM L-glutamine, and 1 mM pyruvate. The 4T1 Luc cells were passed three times in a T75 flask (BD Biosciences, Bedford, Massachusetts) prior to this study, and the confluency was 70% to 80%. *In vivo* experiments were performed using a murine tumor model (4T1 mammary cancer cells grown in Balb/c mice). The animal protocol was approved by the Institutional Animal Care and Use Committee of University of Connecticut. 4T1 breast cancer cells (1 × 105) were injected into the lower right mammary fat-pad of 7-week old Balb/c female mice. The experiments were performed when the tumor sizes reached approximately 6 to 8 mm in diameter and 2 to 3 weeks post-inoculation. All experiments were performed under anesthesia by the inhalation of 1.5% isoflurane. A dose of 100 μL of 100 μM ICG dye and ICG/SWCNT was injected in each mouse using retro-orbital injection technique.

For histology, after overnight fixation in 4% paraformaldehyde, the tumor samples were dehydrated progressively through 30%, 50%, 70%, 90%, and 100% ethanol, and then placed in OCT embedding medium (Tissue-Tek, Torrance, California). Tumor samples were sectioned at 10 μm on a cryostat (Leica CM3050S, Leica Microsystems, Nussloch, Germany), and stored at −20 ℃.

## 4. 2.4 Imaging Experiments

A total of 10 mice were imaged by our co-registered PE/PAT imaging system.[36] A Ti:Sapphire (Symphotics TII, LS-2134, Camarillo, California) laser optically pumped with a Q-switched Nd:YAG laser (Symphotics-TII, LS-2122) delivered 15 Hz, 20-ns pulses at 755-nm wavelength. The energy density of the laser beam was kept at 8 $mJ/cm^2$, which is under the ANSI-specified energy limit of 24 $mJ/cm^2$. The laser beam was coupled into a 1-mm core multimode fiber using a converging lens, as shown in Figure 4.1. The light exiting from the fiber then passed through intralipid to homogenize the beam before illuminating on the tumor area. The intralipid also served as the coupling medium between the transducer and mouse tumor. Before imaging, the mice were shaved and placed in supine position on a heating pad. The intralipid bag was placed between the mouse and a linear ultrasound transducer of 6-MHz center frequency and 80% bandwidth (W.L. Gore and Associates, Inc., Newark, Delaware). The central 64 channels of this 128-channel linear ultrasound transducer were used by the system. To monitor the effect of ICG or ICG/SWCNT injection on the absorption within the tumor area, co-registered PE/PAT images and the corresponding radio frequency (RF) data or transducer data were acquired for up to 80 min for the ICG group and 80 to 165 min (120 min on average) for the ICG/SWCNT group. Five mice were injected with ICG and the other five with ICG/SWCNT. Ideally, monitoring for an extended period of time is required to obtain complete tumor wash-out characteristics of ICG/SWCNT group. However, such monitoring would require the mice to be under anesthesia for an extended period of time. The studies had to be terminated after 80 to 165 min, due to animal study constraints.

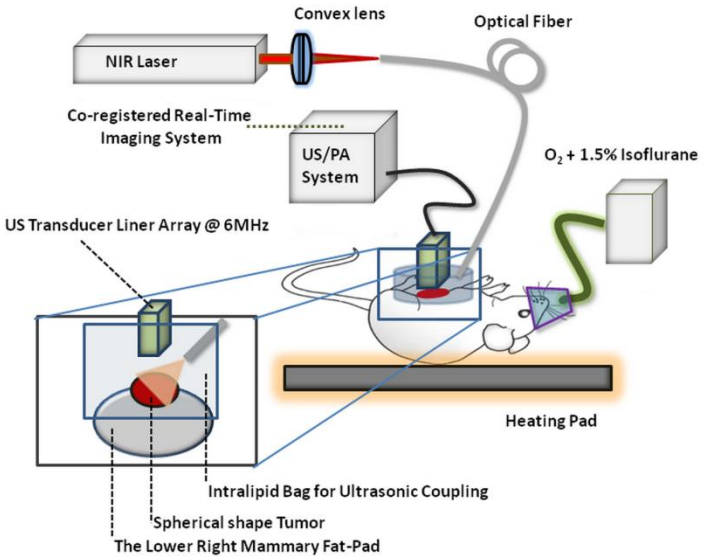


Figure 4.1 *In vivo* ultrasound and photoacoustic tomography (PAT) imaging setup.

### 4.2.5 Image Reconstruction and Data Processing

The imaging system was capable of capturing and storing RF data, and then forming and storing co-registered PE/PAT images at a maximum rate of 3 frames per second.[36] In mouse experiments, we averaged the RF data over seven times to achieve a better signal-to-noise ratio (SNR), and thus the corresponding imaging rate is about 2.5 seconds per frame. Both PE and PAT images were formed using standard delay-and-sum beam-forming algorithm.[39,40] The envelopes of the beam data were interpolated via scan conversion to each pixel, followed by a logarithmic dynamic range compression. Each PE image was normalized to its own maximum and displayed at 45-dB dynamic range. The PAT images were normalized to the maximum PAT beam envelope, referred as the PAT reference, of all image frames. In this article, SNR is defined as SNR = 20 * $\log_{10}$[ peak envelope of signal /mean(peak envelope of noise)]. PAT dynamic range was set to be the same as SNR to maximize the visualization of the light absorption. In mouse experiments, for the regions several centimeters away from tumor sites, there was no PAT signal due to limited light penetration. Therefore, we have used the averaged peak envelopes of the

photoacoustic beams in these regions as our system noise thresholds. The variations of system noise thresholds from different mouse experiments were very small, and we used the mean value of them to distinguish PAT signals from tumors. The co-registered PE/PAT image was an 8-bit BMP file. The lower half of its color map was gray scaled and was assigned to the PE part, while the upper half was color-coded (red to yellow) and was assigned to the PAT counterpart, as shown in Figure 4.3. Because the shape of the tumors was approximately round, a circular window was chosen, depending on the tumor structure and size information in PE image, to closely define the tumor area for computing PAT summation signal. For each mouse, the summation of PAT beam envelope higher than system noise threshold was computed within the chosen window for each frame and used to estimate the total tumor uptake and wash-out profiles for each experiment.

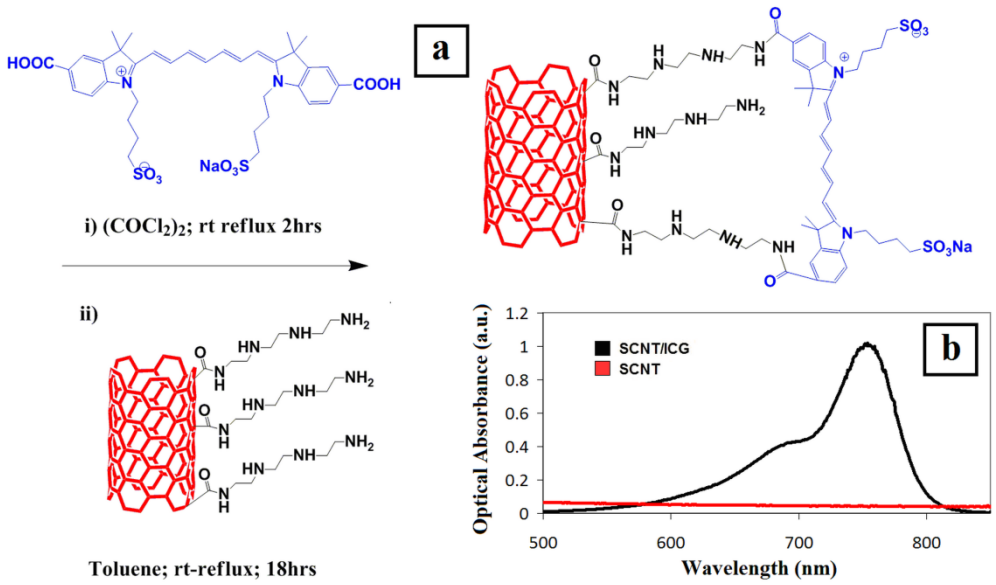


Figure 4.2 (a) Chemical structure of the prepared bis-caboxylic acid-indocyanine green (ICG) covalently attached to an amino-functionalized single-wall carbon nanotube (SWCNT). ICG unit can bind to single CNT through amide bonds or it can bind to two carbon nanotubes through the bridge by forming amide bonds on both ends. (b) Optical absorbance spectrum of the bis-aboxylic acid-ICG covalently attached to an amino-functionalized SWCNT.

To compensate for the laser energy drifting and fluctuations throughout the long experiment, 3% of the output laser energy was split using a beam splitter. This small portion of

light was coupled into a photodiode (PDA10A, ThorLabs, Newton, New Jersey), and the temporal profile of the laser pulse was measured and recorded by a DAQ board (CS22G8, DynamicSignals, Lockport, Illinois) at 1-GHz sampling rate. For each PAT frame, seven sets of PAT RF data and the corresponding photodiode output of the laser pulses were synchronously acquired and averaged by the imaging system to increase PAT SNR. Beam envelope of each PAT frame was divided by the average laser pulse peak before it was used to compute a PAT summation signal (compensated PAT summation). This method was verified by imaging fixed absorption phantoms for over 2 h. Verification experiments were repeated 10 times, and the standard deviation in the compensated PAT summation signal was in the range of ±10% of its mean. The reconstructed PAT beam envelope showed the initial pressure distribution in the imaging plane, which is a product of the Grüneisen coefficient, local light fluence, and light absorption coefficient.[41] We assumed that the Grüneisen coefficient and local light fluence did not change much with time in each pixel location after the laser energy compensation, and the change in the PAT beam envelope was proportional to the light absorption coefficient. The change in the light absorption coefficient in turn was due to the hemoglobin contrast and injected dyes in our experiments. Consequently, the change in the PAT beam envelope signal was the result of the progressive uptake and wash-out characteristics of the injected dyes at tumor sites. This is approximately correct provided that the change in the compensated PAT summation caused by intrinsic hemoglobin contrast is negligible.

## 4. 2.6 Fluorescence Scanner

Ten-micrometer frozen tumor sections were dried and imaged by an Odyssey Infrared Imaging System (Li-COR Biosciences, Lincoln, Nebraska). This instrument provides scan resolution ranging from 21 to 339 μm. The fluorescence images were acquired at the highest resolution of 21 μm. The selected excitation channel was 785 nm and the emission channel was

820 nm with a bandwidth of 40 to 50 nm. The images were obtained from the analysis software provided by the company. The length of time the laser spends on any given point is the dwell time. The laser dwell time per pixel of the Odyssey system used in this study, is approximately equal to the resolution/speed. The speed is set by the quality setting and varies from 5 cm/s at the highest quality to 40 cm/s for the lowest. Laser intensity is constant. In our experiments at resolution =21 mm and quality = highest, the dwell time (per pixel) = $(21 \times 10^{-4})/5 \sim= 0.42$ ms. All samples were imaged using the same setup parameters for the Odyssey Infrared Imaging System in terms of resolution, brightness, and contrast. Two quantitative terms were computed from the fluorescence images using Image J software package.[42] The first term was the mean pixel value of the fluorescence images in the entire sample area. The second term was the mean pixel values of fluorescence images only inside the tumor and at the boundary of the tumor for each sample. A 2 $\times$ 2 $mm^2$ window was used to measure the mean intensity of the tumor interior and boundary. For each fluorescence image, Image J measured 10 peripheral and two central areas, and the mean pixel values in the peripheral and central areas were used to obtain the relative fluorescence intensity ratio of each mouse sample, because the pixel value in fluorescence image was proportional to the average fluorescence intensity. This procedure was repeated for five ICG and five ICG/SWCNT samples.

## 4.3 Results

Figure 4.2(a) shows the chemical structure of the bis-caboxylic acid-ICG covalently attached to an amino-functionalized SWCNT, and Figure 4.2(b) shows the optical absorbance spectrum of this compound. The peak observed at 750 nm exhibits more than 25-fold higher absorbance at the same wavelength compared with the non-functionalized SWCNT.

Two examples of co-registered PE/PAT images of ICG/SWCNT- and ICG-injected mice are shown in Figure 4.3(b) and 4.3(c) and Figure 4.3(e) and 4.3(f), respectively. There is also an example of control without injection of contrast agent, as shown in Figure 4.3(h) and 4.3(i). Because the maximum PAT beam envelope in ICG/SWCNT experiment is higher than that in ICG and the control case, we have different PAT dynamic ranges (25, 20, and 18 dB, respectively) for the three examples to obtain better visualization of these three sets of images. In all studies, the PE images reveal a hypoechoic mass near the skin surface, which was verified at the beginning of each experiment to be the tumor area. Note the color bar in Figure 4.3 is the color map used for the display of PE image or co-registered PE/PAT image. In post-processing, PAT reference in ICG/SWCNT experiment is different from that in ICG experiment and control case. Thus, the same color in these three sets of images corresponds to different levels of light absorption except the pure red, which corresponds to system noise threshold.

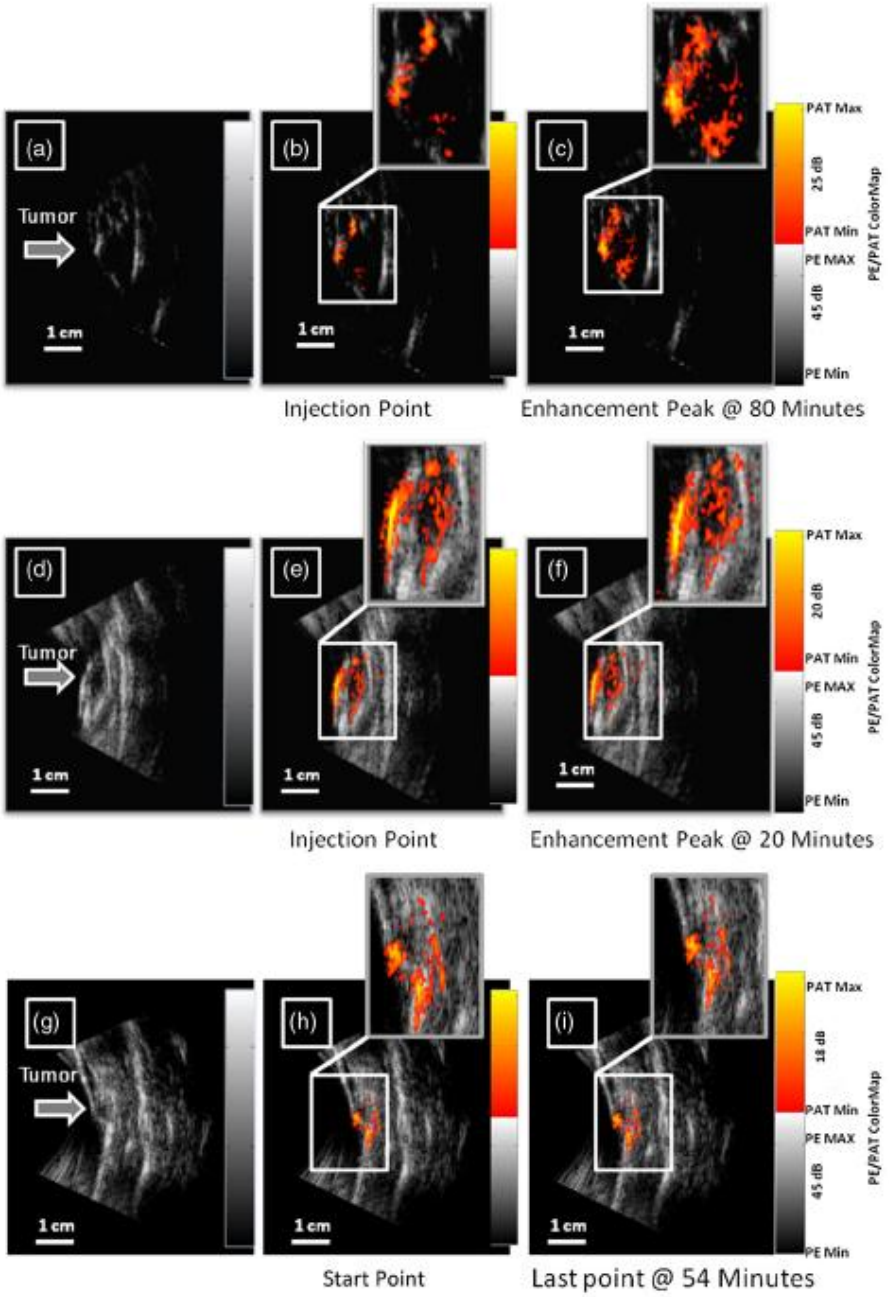


Figure 4.3 Co-registered PE/PAT images acquired at tumor sites. (a) Pulse-echo (PE) image of ICG/SWCNT-injected mouse at injection point. (b) Co-registered PE/PAT image of ICG/SWCNT-injected mouse at injection point. (c) Co-registered PE/PAT image of ICG/SWCNT-injected mouse at 80 min after injection (enhancement peak of ICG/SWCNT). (d) PE image of ICG injected mouse at injection point. (e) Co-registered PE/PAT image of ICG-injected mouse at injection point. (f) Co-registered PE/PAT image of ICG-injected mouse at 20 min after injection (enhancement peak of ICG). (g) PE image of control sample. (h) Co-registered PE/PAT image of control sample at the experiment's start point. (i) Co-registered PE/PAT image of control sample after 54 min. The signal-to-noise ratio (SNR) for PAT was 25 dB in (b, c), 20 dB in (e, f), and 18 dB in (h, i); while SNR for PE was 64 dB in (a–c), 49 dB in (d–f), and 48 dB in (g–i). For display, the PAT dynamic range was set to be the same as PAT SNR to maximize the visualization, while the PE dynamic range was kept to be 45 dB in all subfigures.

The compensated PAT summation signal for the ICG/SWCNT-injected mouse tumor in Figure 4.3(b) and 4.3(c) and the ICG-injected mouse tumor in Figure 4.3(e) and 4.3(f) are shown in Figure 4.4(a) and 4.4(b), respectively. The control case is given in Figure 4.4(c). The co-registered PE/PAT images shown in Figure 4.3(b) and 4.3(c) and the corresponding PAT summation signal shown in Figure 4.4(a) indicates that most of the ICG/SWCNT dye uptake by the tumor is distributed around the periphery, and the compensated PAT summation signal is 3.32 times higher than the pre-injection level. The images shown in Figure 4.3(e) and 4.3(f) reveal similar periphery enhancement but have much weaker compensated PAT summation signal of 1.50 times higher at the peak of the post-ICG injection as compared with the pre-injection level. The corresponding PAT summation signal increases after injection, reaches a peak after about 20 min and then slowly reduces to the pre-injection level at around 60 to 80 min, as shown in Figure 4.4(b). This is in sharp contrast to the ICG/SWCNT-injected mouse [Figure 4.4(a)], in which the compensated PAT summation signal keeps increasing during the entire experiment. Note that Figure 4.3(c) was obtained at 80 min post-injection of ICG/ SWCNT, and Figure 4.3(h) was at the peak enhancement of ICG around 20 min.

In our experiment, the light absorption mainly comes from intrinsic hemoglobin and injected dyes. Both contribute to the compensated PAT summation signal during the experiment. Figure 4.4(c) shows the corresponding compensated PAT summation of the mouse without injection and monitored for 54 min. The curve is almost flat, and the standard deviation is only 4.78% of its mean. It shows that the hemoglobin contrast of the mouse tumor under anesthesia for longer PE/PAT experiment causes negligible change in the PAT summation signal. The compensated PAT summation signals in ICG/SWCNT and ICG experiments are mainly caused by the injected dyes.

The statistical analysis of the normalized compensated PAT summation signals for the ICG- and ICG/SWCNT-injected mice is shown in Figure 4.5, revealing that ICG is able to provide 1.33(±0.1) times higher compensated PAT summation than the pre-injection level at approximately 20 min peak response time. On the other hand, ICG/SWCNT provides 2.28 (±0.78) times higher compensated PAT summation than the pre-injection level at 80 min and an even higher ratio of 2.96 (±0.69) at the end point of the experiments (120 min on average). Statistical significance was achieved between the two groups at 80 min ($p < 0.032$). If the end point of compensated PAT summation signal of ICG/SWCNT was compared with that of ICG group, the statistical significance is even higher with $p < 0.004$.

The *ex vivo* fluorescence images obtained from excised tumor samples (Figure 4.6) help to visualize the distribution of both ICG/SWCNTs and ICG. Figure 4.6(b) demonstrates the significant increase in ICG/SWCNT accumulation and also the peripheral distribution, while Figure 4.6(a) shows weaker ICG fluorescence signals and more uniform distribution. The fluorescence images obtained from tumor samples support the photoacoustic findings. Figure 4.7 shows the statistics of mean pixel value of the entire samples measured from *ex vivo* fluorescence images obtained from two groups of ICG and ICG/SWCNT using Odyssey Infrared Imaging System. The mean pixel value of the entire sample is 5.68 (±4.74) for the ICG group and 41.00 (±11.11) for the ICG/SWCNT group. This difference is statistically significant ($p = 0.001$).

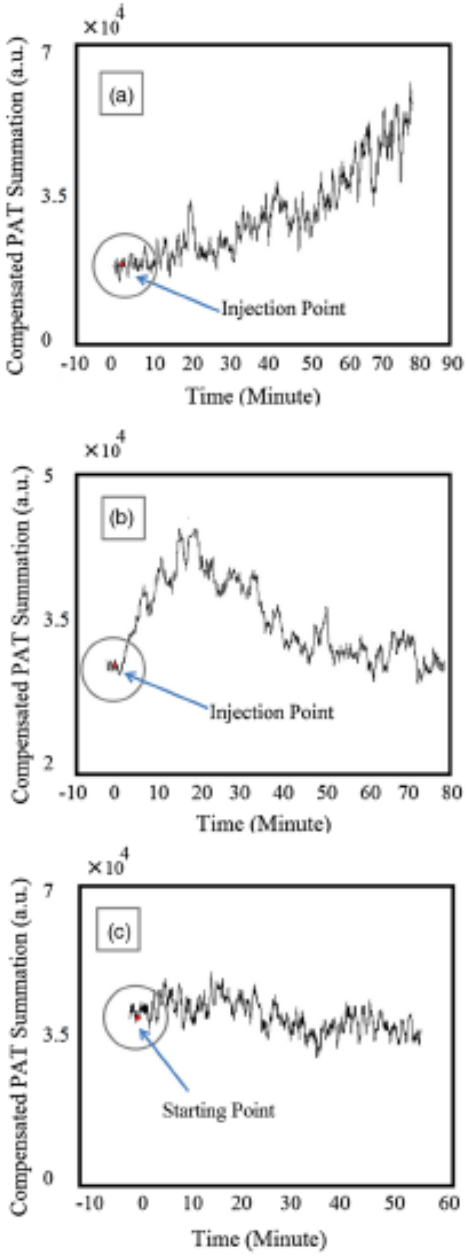


Figure 4.4 (a, b) Typical compensated PAT summation curves of ICG/SWCNT- and ICG-injected groups. (a) Compensated PAT summation of ICG/SWCNT-injected mouse with PAT images shown in Figure 4.3(c) and 4.3(d). (b) Compensated PAT summation of ICG-injected mouse with PAT images shown in Figure 4.3(g) and 4.3(h). (c) Compensated PAT summation curve for tumor mouse without dye injection.

We also compared the statistical significance of the mean pixel value of the tumor interior and tumor boundary in fluorescence images for the two groups (Figure 4.8). For the ICG group, the mean pixel value of the interior is 3.22 (±1.69) and the mean at the tumor boundary is

8.13 (±3.99) (p = 0.035). For the ICG/SWCNT group, the mean pixel value of the interior is 12.30 (±7.05) and the mean pixel value at the tumor boundary is 36.46 (±12.68) (p = 0.006). The statistical significance between the mean intensities of the inside and the periphery of ICG/SWCNT group increased significantly compared with that of ICG.

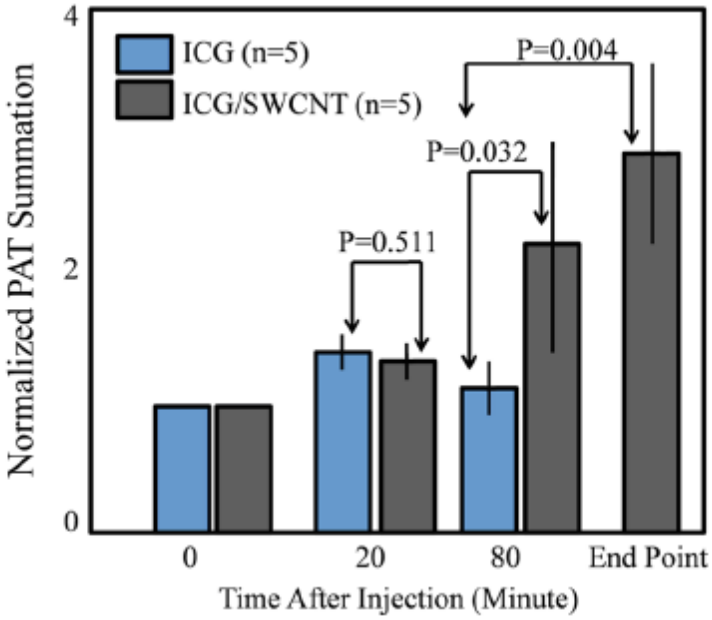


Figure 4.5 Statistics of normalized PAT summation signals after compensation obtained at injection point 20- and 80-min post-injection of ICG and ICG/SWCNT groups and end points of the ICG/SWCNT group.

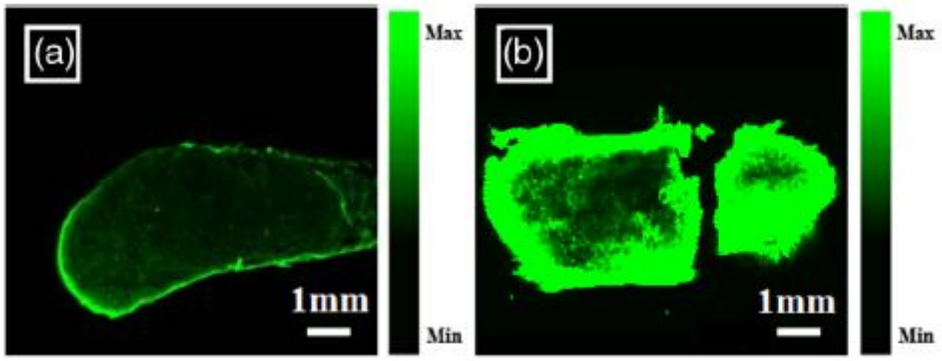


Figure 4.6 *Ex vivo* fluorescence images of harvested tumors. (a) *Ex vivo* fluorescence image of ICG-injected tumor sample. (b) *Ex vivo* fluorescence image of ICG/SWCNT-injected tumor sample.

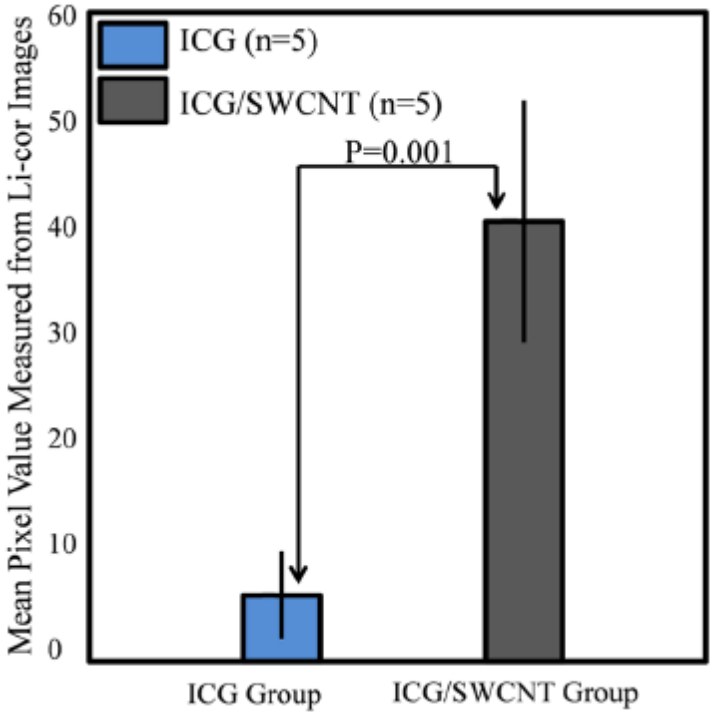


Figure 4.7 Statistics of mean pixel value of the entire samples measured from *ex vivo* fluorescence images obtained from tumor samples of two groups.

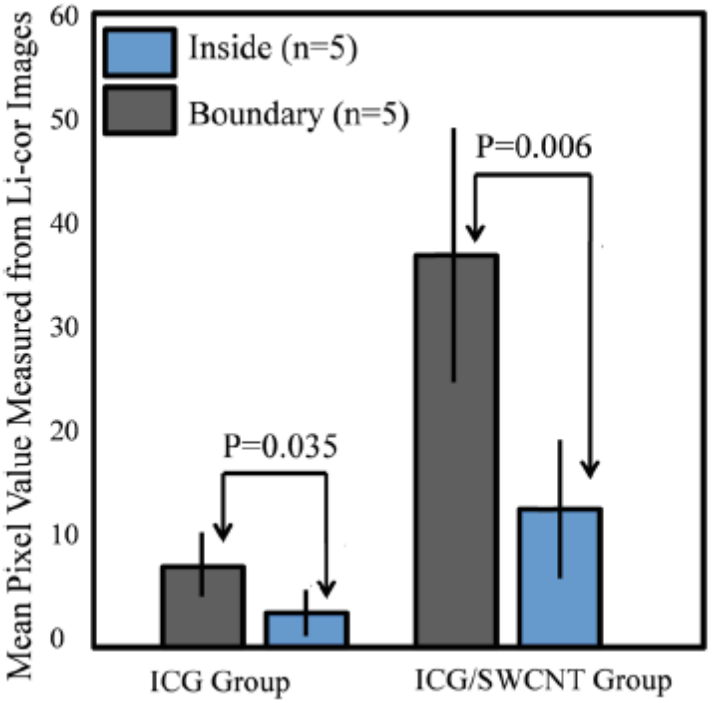


Figure 4.8 Statistics of mean pixel values measured inside tumor and periphery of the tumor from *ex vivo* fluorescence images.

## 4.4 Discussion and Summary

In our experiments, the compensated PAT summation signal after injection from ICG group always decreased to pre-injection level after approximately 60 to 80 min. However, the compensated PAT summation signal after injection from ICG/SWCNT group was always increasing during experiment. Ideally, we would like to record the complete post-injection wash-out characteristics of ICG/SWCNT. However, the condition of the mice under long periods of anesthesia is very unpredictable. Repositioning of the tumor back to the same imaging plane of the PAT imaging system for continuous monitoring after an anesthesia break is a challenging task, because the high-resolution PAT images are very sensitive to the relative positions of the mouse tumor and the ultrasound transducer. Since our goal was to compare uptake and wash-out characteristics of ICG and ICG/SWCNT and to quantify the contrast improvement of ICG/SWCNT in a similar time frame, we recorded the PAT data of the ICG/SWCNT-injected mouse group from 80 to 165 min, depending on the health condition of each mouse. At 20-min post-injection, which was the peak enhancement of ICG, we obtained a similar enhancement of 29% and 33% for ICG and ICG/SWCNT ($p = 0.511$), respectively. However, at 80-min post-injection, the ICG/SWCNT demonstrated 128% enhancement, while ICG was at a similar pre-injection level ($p = 0.032$). If the end point of the compensated PAT summation in the ICG/SWCNT group was used to compute the enhancement, 196% enhancement was achieved ($p = 0.004$). It is highly likely that the PAT signal of ICG/SWCNT would continuously rise beyond the end point and that would provide further contrast enhancement.

It is not surprising that we have observed prolonged PAT enhancement with the ICG/SWCNT. The microenvironments of solid tumors are fundamentally different from normal tissues. It includes poorly organized vascular architecture, impaired lymphatic system, poor oxygenation, acidosis, higher interstitial fluid pressure, and the presence of the extracellular

matrix.[43,44] It has been reported that the degree of penetration of nanoparticles through the cancer cells depends on several factors including size,[45] morphology,[46] and surface charge.[47] The enhanced permeability and retention (EPR) effect aids in nanoparticles diffusion and convection through abnormal large fenestrations tumor vasculature and the inefficient lymphatic drainage. EPR allows nanoparticles generally less than 150 nm in diameter to cross from vasculature into the interstitium.[48] Generally, diffusion of nanoparticles into solid tumors is limited by the interactions with high-density cells, presence of the extracellular matrix as a transport barrier, and higher interstitial fluid pressure.[49] Huo et al. studied the size effect of gold nanoparticles on the localization and penetration behavior in tumor.[50] They showed that small size nanoparticles penetrated more deeply into tumor and accumulated more effectively after a single intravenous dose. In contrast, larger nanoparticles were primarily localized in the periphery of the tumor spheroid and around blood vessels hindering deep penetration into tumors. In our study, we used SWCNTs with lengths ranging from 100 to 1000 nm. Although it is desirable to enhance the delivery of contrast agents or drugs into interior of the tumor using smaller nanoparticles, the observed periphery enhancement from PAT images and confirmed measurements from fluorescence images is valuable in guiding surgeons to assess tumor boundary and to improve surgical resection of tumors for achieving clean tumor margins.[51] Future studies will be focused on the synthesis of ICG/SWCNT with tumor-targeting agents or drugs of different sizes for potential diagnostic and therapeutic applications.

Both ICG, from Sigma-Aldrich, and bis-caboxylic acid-ICG are small molecules (on the order of 1 nm). We believe that removal mechanisms for both compounds are the result of renal clearance and elimination of residues from general circulation by the liver. Bis-caboxylic acid-ICG, however, is able to remain in the body for a longer time. ICG from Sigma-Aldrich contains a naphthindole unit in the ICG dye rather than the simple indole unit present in our dye. We incorporated a carboxylic acid group on the benzene ring, i.e., an indolecarboxylic acid rather

than a naphthindole moiety. Since the ICG derivative contains two indole units, there are two carboxylic acid groups in the ICG used in this study. The replacement of the naphthindole with an indolecarboxylic acid may influence the aggregation issue, which was predominant in the commercially available variant of the dyes. The di-carboxylic acid moiety certainly increased the ICG dye solubility in aqueous solutions, which we believe led to a longer resistance in the circulation in comparison with ICG from Sigma-Aldrich. Further, we utilized these reactive COOH moieties to covalently attach the SWCNT to the dye. The excretion of bis-carboxylic acid derivative-ICG covalently conjugated to SWCNTs is strongly dependent on the size, shape, and surface chemistry, and it may happen via renal and fecal pathways [52] and need a much longer time in comparison with ICG groups alone, as the size of the ICG/SWCNT particles are much larger than that of ICGs.

Non-functionalized CNTs seem to be able to remain in the body for a long time, but not permanently. Ryman-Rasmussen et al. showed the inhaled nanotubes remained in the sub-pleural wall for at least 14 weeks.[53] Elgrabli et al. showed that the large numbers of CNTs instilled into the lungs of rats were cleared after 3 months.[54] On the other hand, the length of CNTs has a great impact on the clearance process, and a high aspect (length to width) ratio can influence biopersistence.[55] The recent studies indicate that there is a completely different story for functional CNTs.[56] Singh et al. reported that surface-functionalized, water-dispersible SWCNTs (average diameter 1 nm; average length 300 to 1000 nm) were capable of rapid and effective renal clearance and urinary excretion with a blood circulation half-life of about a few hours.[57] In this study, we believe that the removal mechanism for SWCNT is the result of rapid renal clearance and elimination of residues from general circulation by the liver. Because of experimental constraints for animals under continuous anesthesia, we could not monitor the ICG/SWCNT-injected mice for several hours in this study. Future studies will consider starting

experiments after injecting ICG/SWCNT for a certain period of time to assess the life time of ICG/SWCNT.

This study has limitations. In a previous work, we found that simply mixing the ICG and the SWCNT together was ineffective in accumulating the dye in the tumor. We attributed this to the lack of covalent binding that led to quick wash-out of the ICG molecules. We therefore reacted the SWCNT with triethylenetetramine to generate SWCNT-$NH_2$. We also prepared our bis-carboxylic acid-ICG dye via previously reported methodology. The free carboxyl groups were converted to the corresponding acid chloride by reaction with oxalyl chloride, and subsequent reaction with SWCNT-$NH_2$ gave the ICGSWCNT-$NH_2$. Successive filtration and washings removed non-covalently attached ICG and SWCNT-$NH_2$ leaving the covalently bound ICG-SWCNT-$NH_2$. Analysis by Raman IR showed the band at 514 nm, consistent with the expected amide moiety. The insolubility of this complex in the solvents required to do NMR and the lack of the volatility to the obtained cogent mass spectral data made it virtually impossible to exactly determine the extent of covalent bonding. We attempted to determine the weight % and found that 192 mg of the ICG resulted in 88 mg of the ICG-SWCNT-$NH_2$. However, we were unable to separate the un-reacted starting material in sufficient purity to accurately determine the mass of the un-reacted ICG or the un-reacted SWCNT-$NH_2$, which makes the weight % calculation unreliable. While we cannot determine where the units are attached or exactly how many units are attached per unit of the dye, the Raman IR data clearly shows covalent binding. Based on the literature data, a covalent attachment system generally improves delivery of cargos to the target site.[58] For example, the covalent attachment of electro-active groups on the side-wall of CNTs is a good strategy to avoid any loss of these groups by diffusion in the solution.[59] However, to the best of our knowledge, there is no report in the literature on delivery of ICGs through covalent attachment to SWCNTs; this could be a future topic of research.

In summary, we have presented a novel photoacoustic contrast agent which is based on bis-carboxylic acid derivative of ICG covalently conjugated to SWCNT (ICG/SWCNT). The detection sensitivity of the new contrast agent in a mouse tumor model was demonstrated in vivo using ICG and ICG/SWCNT-injected mice. It was shown that ICG/SWCNT provides approximately two times higher post-injection contrast than ICG. Additionally, the ICG/SWCNT enhancement was mainly observed at the tumor periphery, due to the size and shape of the SWCNTs, which is valuable in guiding surgeons to assess tumor boundaries in order to achieve clean tumor margins, and thereby to improve the surgical resection of tumors.

## References


1. R. Philip et al., “Absorption and fluorescence spectroscopic investigation of indocyanine green,” J. Photochem. Photobiol. A 96(1), 137–148 (1996).

2. M. L. Landsman et al., “Light-absorbing properties, stability, and spectral stabilization of indocyanine green,” J. Appl. Physiol. 40(4), 575–583 (1976).

3. R. C. Benson and H. A. Kues, “Fluorescence properties of Indocyanine green as related to angiography,” Phys. Med. Biol. 23(1), 159–163 (1978).

4. A. El-Desoky et al., “Experimental study of liver dysfunction evaluated by direct indocyanine green clearance using near infrared spectroscopy,” Br. J. Surg. 86(8), 1005–1011 (1999).

5. T. Wygnanski-Jaffe et al., “ICG angiography-guided photodynamic therapy for large pigment epithelial detachments in age-related macular degeneration,” Ophthal. Surg Lasers Imag. 37(5), 358–363(2006).

6. H. Shinohara et al., “Direct measurement of hepatic indocyanine green clearance with near-infrared spectroscopy separate evaluation of uptake and removal,” Hepatology 23(1), 137–144 (1996).

7. W. R. Chen et al., “Chromophore-enhanced laser tumor tissue photothermal interaction using an 808-nm diode laser,” Cancer Lett. 88(1), 15–19 (1995).

8. S. Fickweiler et al., “Indocyanine green: intracellular uptake and phototherapeutic effects in vitro,” J. Photochem. Photobiol. B 38(2–3), 178–183 (1997).

9. L. S. Bass et al., “Changes in type I collagen following laser welding,” Lasers Surg. Med. 12(5), 500–505 (1992).

10. K. Schomacker et al., “Biodistribution of indocyanine green in a porcine burn model: light and fluorescence microscopy,” J. Trauma 43(5), 813–819 (1997).

11. A. Rubben et al., “Infrared videoangiofluorography of the skin with indocyanine green—rat random cutaneous flap model and results in man,” Microvasc. Res. 47(2), 240–251 (1994).

12. T. Velde et al., “The use of fluorescent dyes and probes in surgical oncology,” Eur. J. Surg. Oncol. 36(1), 6–15 (2010).

13. M. Jacob et al., “Impact of the time window on plasma volume measurement with indocyanine green,” Physiol. Meas. 29(7), 761–770(2008).

14. R. Mudra et al., “Analysis of nearinfrared spectroscopy and Indocyanine green dye dilution with Monte Carlo simulation of light propagation in the adult brain,” J. Biomed. Opt. 11(4), 044–009 (2006).

15. V. Saxena, M. Sadoqi, and J. Shao, “Enhanced photo-stability, thermalstability and aqueous-stability of indocyanine green in polymeric nanoparticulate systems,” J. Photochem. Photobiol. B 74(1), 29–38(2004).

16. V. Saxena, M. Sadoqi, and J. Shao, “Polymeric nanoparticulate delivery system for indocyanine green: biodistribution in healthy mice,” Int. J. Pharm. 308(1–2), 200–204 (2006).

17. G. Kim et al., “Indocyanine green-embedded PEBBLEs as a contrast agent for photoacoustic imaging,” J. Biomed. Opt. 12(4), 044020(2007).

18. V. Rodriguez et al., “Encapsulation and stabilization of Indocyanine green within poly(styrene-alt-maleic anhydride) block-poly(styrene) micelles for near-infrared imaging,” J. Biomed. Opt. 13(1), 014025 (2008).

19. R. Rajagopalan et al., “Stabilization of the optical tracer agent Indocyanine green using noncovalent interactions,” Photochem. Photobiol. 71(3), 347–350 (2000).

20. J. Devoiselle et al., “Preliminary study of the in vivo behaviour of an emulsion formulation of indocyanine green,” Lasers Med. Sci. 13(4) 279–282 (1998).

21. V. B. Rodriguez et al., “Encapsulation and stabilization of Indocyanine green within poly(styrene-alt-maleic anhydride) block-poly(styrene) micelles for near-infrared imaging,” J. Biomed. Opt. 13(1), 014025 (2008).

22. C. Cha et al., “Carbon-based nanomaterials: multifunctional materials for biomedical engineering,” ACS Nano. 7(4), 2891–2897 (2013).

23. L. Zhuang, Y. Kai, and L. Shuit-Tong, “Single-walled carbon nanotubes in biomedical imaging,” J. Mater. Chem. 21(3), 586–598 (2010).

24. M. Hughes, E. Brandin, and J. Golovchenko, “Optical absorption of DNA-carbon nanotube structures,” Nano Lett. 7(5), 1191–1194 (2007).

25. S. Berciaud et al., “Absorption spectroscopy of individual single-walled carbon nanotubes,” Nano Lett. 7(5), 1203–1207 (2007).

26. V. G. Andreev et al., “Optoacoustic tomography of breast cancer with arc-array transducer,” Proc. SPIE 3916, 36–47 (2000).

27. X. Wang et al., “Noninvasive laser-induced photoacoustic tomography for structural and functional in vivo imaging of the brain,” Nat.Biotechnol. 21(7), 803–806 (2003).

28. R. A. Kruger et al., “Photoacoustic ultrasound reconstruction tomography,” Med. Phys. 22(10), 1605–1609 (1995).

29. L. V. Wang, “Prospects of photoacoustic tomography,” Med. Phys. 35(12), 5758–5767 (2008).

30. G. Hong et al., “Multifunctional in vivo vascular imaging using nearinfrared II fluorescence,” Nat. Med. 18(12), 1841–1846 (2012).

31. M. Pramanik et al., “In vivo carbon nanotube-enhanced non-invasive photoacoustic mapping of the sentinel lymph node,” Phys. Med. Biol. 54(11), 3291–3301 (2009).

32. J. R. Rajian et al., “Drug delivery monitoring by photoacoustic tomography with an ICG encapsulated double emulsion,” Opt Express. 19(15), 14335–14347 (2011).

33. C. Wang et al., “Protamine functionalized single-walled carbon nanotubes for stem cell labeling and in vivo Raman/magnetic resonance/photoacoustic triple-modal imaging,” Adv. Funct. Mater. 22(11), 2363–2375 (2012).

34. A. de la Zerda et al., “Ultrahigh sensitivity carbon nanotube agents for photoacoustic molecular imaging in living mice,” Nano Lett. 10(6),2168–2172 (2010).

35. C. Pavlik et al., “Synthesis and fluorescent characteristics of imidazole-indocyanine green conjugates,” Dyes Pigm. 89(1), 9–15 (2011).

36. U. Alqasemi et al., “FPGA-based reconfigurable processor for ultrafast interlaced ultrasound and photoacoustic imaging,” IEEE Trans. Ultrason. Ferroelectr. Freq. Control 59(7), 1344–1353(2012).

37. A. Osorio et al., “H2SO4/HNO3/HCl-functionalization and its effect on dispersion of carbon nanotubes in aqueous media,” Appl. Surf. Sci. 255(5), 2485–2489 (2008).

38. G. R. Cherrick et al., “Indocyanine green: observations on its physical properties, plasma decay, and hepatic extraction,” J. Clin. Invest. 39(4), 592–600 (1960).

39. R. A. Mucci, “A comparison of efficient beamforming algorithms,” IEEE Trans. Acoust. Speech Signal Process 32(3), 548–558 (1984).

40. C. G. A. Hoelen and F. F. M. de Mul, “Image reconstruction for photoacoustic scanning of tissue structures,” Appl. Opt. 39(31), 5872–5883 (2000).

41. M. Xu and L. H. Wang “Photoacoustic imaging in biomedicine,” Rev. Sci. Instrum. 77(4), 041–101 (2006).

42. S. Chou et al., “Ultrasonographic evaluation of endometrial changes using computer assisted image analysis,” J. Obstet. Gynaecol. Res. 36(3), 634–638 (2010).

43. J. M. Brown and A. J. Giaccia, “The unique physiology of solid tumors: opportunities (and problems) for cancer therapy,” Cancer Res. 58(7),1408–1416 (1998).

44. J. Brown and W. Wilson, “Exploiting tumour hypoxia in cancer treatment,” Nat. Rev. Cancer. 4(6), 437–447 (2004).

45. H. Cabral et al., “Accumulation of sub-100 nm polymeric micelles in poorly permeable tumours depends on size,” Nat. Nanotechnol. 6(12), 815–823 (2011).

46. V. Chauhan et al., “Fluorescent nanorods and nanospheres for real-time in vivo probing of nanoparticle shape-dependent tumor penetration,” Angew Chem Int Ed Engl. 50(48), 11417–11420 (2011).

47. B. Kim et al., “Tuning payload delivery in tumour cylindroids using gold nanoparticles,” Nat. Nanotechnol. 5(6), 465–472 (2010).

48. H. Maeda et al., “Tumor vascular permeability and the EPR effect in macromolecular therapeutics,” J. Control Release 65(1–2), 271–284 (2000).

49. T. T. Goodman, P. L. Olive, and S. H. Pun, “Increased nanoparticles penetration in collagenase-treated multicellular spheroids,” Int. J. Nanomed. 2(2), 265–274 (2007).

50. S. Huo et al., “Superior penetration and retention behavior of 50 nm gold nanoparticles in tumors,” Cancer Res. 73(1), 319–330 (2013).

51. J. Ruiterkamp et al., “Impact of breast surgery on survival in patients with distant metastases at initial presentation: a systematic review of the literature,” Breast Cancer Res. Treat. 120(1), 9–16 (2010).

52. K. Yang and Z. Liu, “In vivo biodistribution, pharmacokinetics, and toxicology of carbon nanotubes,” Curr. Drug Metab. 13(8), 1057– 1067 (2012).

53. J. P. Ryman-Rasmussen et al., “Inhaled carbon nanotubes reach the subpleural tissue in mice,” Nat. Nanotechnol. 4(11), 747–751 (2009).

54. D. Elgrabli et al., “Biodistribution and clearance of instilled carbon nanotubes in rat lung,” Part. Fibre Toxicol. 5, 20 (2008).

55. P. G. Coin, V. L. Roggli, and A. R. Brody, “Persistence of long thin chrysotile asbestos fibers in the lungs of rats,” Environ. Health Perspect. 102(5), 197–199 (1994).

56. L. Lacerda et al., “Carbon-nanotube shape and individualization critical for renal excretion,” Small 4(8), 1130–1132 (2008).

57. R. Singh et al., “Tissue biodistribution and blood clearance rates of intravenously administered carbon nanotube radiotracers,” Proc. Natl. Acad. Sci. U S A 103(9), 3357–3362 (2006).

58. S. M. Früh et al., “Covalent cargo loading to molecular shuttles via copper-free click chemistry,” Biomacromolecules 13(12), 3908–3911 (2012).

59. N. Allali et al., “Covalent functionalization of few-wall carbon nanotubes by ferrocene derivatives for bioelectrochemical devices,” Phys. Status Solidi B 249(12), 349–2352 (2012).

# Chapter 5 Feature extraction, Feature Selection and Classifiers for Ovarian Tissue Characterization

In chapter 3, the design and implementation of real-time US/PAT system was fully introduced, including front end circuit, module FPGAs, PCIe FPGA, and PC multi-thread program. With the second version of US/PAT system, we were able to acquire and store RF PAT data, PE beams, intermediate reconstruction result and reconstructed image. Usually, we can get access to the vasculature distribution on the surface of ovaries in the co-registered US/PAT images but it is hard for physicians to judge if the sample is benign or malignant. Note that US/PAT images are normalized absorption amplitude, its spatial distribution is valuable for diagnosis but the phase information is lost in these images. From RF PAT data, or PE beam data, to the final normalized image, there are some other information we can extract to help the diagnosis procedure. So this chapter will try to explore some of photoacoustic features which may be valuable for diagnosis of ovary cancer, then discuss some feature selection method. In the last, two classifiers, logistic regression and support vector machine are presented. Ultrasound spectral features and menopausal condition, as extended features for in-vivo diagnosis are also simply introduced.

## 5.1 Introduction

Ovarian cancer has the highest mortality of all gynecologic cancers because it is predominantly diagnosed in the late stage due to the nonspecific early stage symptoms and lack of efficacious screening techniques.[1,2] Basic examinations including pelvic examination, blood test for CA-125, and transvaginal ultrasound have a low positive predictive value.[3–8] X-ray computed tomography(CT) is also poor in detecting small metastases of less than 2 cm in diameter.[6] Furthermore, magnetic resonance imaging (MRI) is expensive to use and is only reserved as a secondary imaging method when transvaginal ultrasound is not deterministic,

though it is more sensitive than x-ray CT.[9] Positron emission tomography (PET) is useful for detection of recurrent or residual ovarian cancer and for monitoring response to therapy, but it may yield false-negative results in patients with small, necrotic, mucinous, cystic, or low-grade tumors.[10]Based on ultrasound and CA-125 levels, the risk of malignancy index (RMI) was developed to estimate the risk of ovarian cancer. An RMI2 (RMI of method 2) has been estimated to have a sensitivity of 74% to 80%, a specificity of 89% to 92%, and a positive predictive value of approximately 80% for ovarian cancer detection.[11,12] Unfortunately, the subjective scoring with different physicians may result in different diagnostic results for the same patient. Other complex models, such as artificial neural network models and relevance vector machines, have been used to improve ovarian cancer diagnosis, with the relevance vector machine showing the best performance.[13,14]

Photoacoustic tomography (PAT) has been widely investigated as a noninvasive tool for cancer detection and diagnosis.[15–18] PAT utilizes high optical contrast and high resolution ultrasound to image tumor vasculature distribution. In PAT, biological tissue is illuminated by short laser pulses with wavelengths in visible red or near-infrared range, to achieve better penetration depth. Laser energy absorbed by tissue produces transient thermoelastic expansion and generates wideband acoustic waves, which can be detected by ultrasound transducer arrays for reconstruction of the optical absorption distribution of the tissue. Optical absorption distributions at multiple wavelengths can be used to map tumor hemoglobin distribution and oxygen saturation which are directly related to tumor proliferation, growth, and metastasis.[19]

We have developed several co-registered ultrasound and photoacoustic imaging systems for small animal imaging and ovarian cancer detection and characterization; the ultrasound provides anatomical information, while the PAT provides the corresponding light absorption distribution within the anatomical structure.[18, 20–23] The study reported in Reference 18 evaluated 33 *ex vivo* ovaries and showed that malignant ovaries on average exhibited a much higher total

absorption than normal ovaries. The quantitative parameter used to evaluate the total absorption was the measured "average maximum radio-frequency" (AMRF) PAT signal for each ovary, with the maximum taken from the RF signal at each ultrasound array element and the average taken across all the array elements. This single parameter method achieved a sensitivity and specificity of 83% between malignant and normal ovaries ($p = 0.0237$) in the postmenopausal group. The study reported in Reference 23 focused on the spatial frequency and statistical properties of the PAT images. The support vector machine (SVM) classifier in this study achieved 100% sensitivity and specificity for the training group of 33 ovaries, and 76.92% sensitivity and 95.12% specificity for the testing group of 37 ovaries. These results suggest that photoacoustic imaging is a promising modality for improving ultrasound diagnosis of ovarian cancer. However, the above two methods have their own drawbacks. For the single parameter testing used in Reference 18, the measurement of the PAT signal can be affected by imaging system parameters and signal-to-noise ratio (SNR). When the PAT signal from an ovary has a low SNR, these RFs data-based method may not be sensitive enough.

On the other hand, the method developed in Reference 23 focused on PAT images and their spatial patterns. PAT images represent the amplitude of light absorption but cannot provide details such as diagnostic information offered by the spectra of PAT beamformed data or beams, which is the delay-and-sum of all channel RF signals. Studies from other groups have revealed that the spectrum parameters from a PAT channel signal[24–27] or beam, [28, 29] such as the spectral slope and 0-MHz intercept, are affected by the photoacoustic target dimension and chromospheres' concentration; [24–29] these parameters could provide valuable information for cancer characterization and classification. Furthermore, in the formation of PAT images, the spatial patterns of PAT images are affected by the manually set dynamic range and the mapping method between beam envelope and pixel values. Improper setting of the dynamic range or nonlinear mapping of beam envelope and pixel values may lower the sensitivities and

specificities for image-based classifiers.[23] In this chapter, we extract new features from photoacoustic beams and their envelopes to explore the spectral information and spatial homogeneity of light absorption in ovarian tissues and to combine them with statistical and spatial features obtained from PAT images to improve the performance of classifiers for ovarian cancer diagnosis.

## 5.2 Methodology

The details of the experimental setup and imaging system can be found in Reference 30. The typical size of human ovaries is in the range of 2 to 7 cm with approximately elliptical shapes. In *ex vivo* studies, each ovary was placed inside intralipid solution and supported by a holder made of thin optical fibers. The distance between the sample and the imaging probe surface was adjusted to approximately 1 cm, which is the typical vaginal muscle wall thickness. The intralipid had a reduced scattering coefficient of 4 $cm^{-1}$ and absorption coefficient of 0.02 $cm^{-1}$ to emulate the optical properties of tissue. Based on the measurements of pig vaginal muscles, the reduced scattering coefficient is in the range of 3 to 5 $cm^{-1}$ and the absorption coefficient is in the range of 0.02 to 0.04 $cm^{-1}$. The details of the co-registered ultrasound and PAT probe used for the reported experiments were given in Reference. 30. Note that different light delivery system may cause different illumination pattern for ovary imaging which may affect the effectiveness of features related to illumination or absolute value of absorption. This will be simply discussed in the end of this chapter.

Briefly, the probe consists of a transvaginal ultrasound probe (6-MHz central frequency and 80% bandwidth, Gore and Associates, Inc., Newark, Delaware) and 36 fibers of 200-μm core diameter mounted around the ultrasound transducer to uniformly deliver the light. Both ultrasound probe and the fibers were shielded inside a protective sheath internally lined with a highly reflecting aluminum sheet, with which uniform fluence underneath the probe surface can be achieved. The laser energy density on the tissue surface was $\sim 17 mJ/cm^2$ at 750 nm

wavelength, which is below the American National Standards Institute safety limit of 24 mJ/cm$^2$ at this wavelength.

Signals from 128 channels of the transvaginal probe were used to form the co-registered ultrasound and PAT images. Both the pulse-echo (PE) ultrasound image and PAT image were formed by using conventional delay-and-sum beamforming techniques.[31,32] In PE imaging, one angular beam is formed by applying a delay-and-sum algorithm on the received RF signals from all channels or a certain number of channels (65 in our study) centered in the direction of the transmission. A total of 93 evenly distributed PE beams over 120 degrees are used to form PE images. In PAT, a sector scan is also used to co-register with the corresponding PE image. Each angular beam is formed by applying a delay-and-sum algorithm on the received RF photoacoustic signals synchronized with each laser pulse. A total of 151 PAT beams were formed and evenly distributed across the 120-degrees image plane. The PE and PAT beam envelopes were subsequently obtained by base-band demodulation and amplitude detection. Spectral information was lost in the procedure of demodulation and amplitude detection of beam envelope. However, it was preserved in the PE and PAT beams. In the preprocessing stage, the mapping between the PAT beam envelopes and PAT image pixel values was set to be linear instead of the conventional logarithmic mapping in ultrasound imaging. The dynamic range of the image was set by mapping the system noise threshold of the PAT beam envelope to a pixel value of 0 and mapping the maximum of the envelope to a pixel value of 255. The system noise threshold for each image frame was estimated from the averaged envelope peaks of non-region-of-interests (nonROIs) identified from the co-registered PE image. NonROIs are regions away from ovarian samples in the imaging plane where the light absorption was negligible. Both RF channel data from the transducer array and PAT beams contained spectral information. However, the channel data were the integration of signals from the arc with the center at the channel element and its SNR was low in general. In beamforming, the coherent RF signals from the same absorber detected at all

channels were appropriately delayed and summed and the SNR was improved. In the reported study, we have used the averaged spectral parameter (see section 5.2.2.1 for details) of PAT beams in the suspicious area to extract features for classification.

### 5.2.1 Center Estimation for Suspicious Area

The ultrasound imaging field of view covers 120 degrees in the lateral dimension and 7.7 cm in depth, while reconstructed PAT images are mainly confined to several centimeters' area underneath the probe. Therefore, limiting data analysis within the suspicious area will greatly reduce the total computation time. To crop the suspicious areas, the centers of these areas should be estimated. A simple method introduced in Reference 23 was applied as follows: the radon transforms of a PAT image along 0 (x axis) and 90 degrees (y axis) can be simply calculated from the summation of the PAT pixel values along the column and row directions. After normalization to their respective peaks, the radon transforms along 0 and 90 degrees were used to estimate the center of the suspicious area using the normalized Gaussian model in the following equation:

$$f(x) = exp\left[-\frac{(x-\mu)^2}{2\sigma^2}\right] \quad (5.1)$$

In equation 3.1, $\mu$ is the index of the estimated center and σ represents the spatial expansion of vasculature along the projection direction. A 3.0 cm by 1.5 cm window (large enough in most cases) with the estimated center was then applied to the PAT image to crop the suspicious area. Note that the normalized Gaussian model is used to estimate the center of the suspicious area from 0 and 90 degrees or x and y projections.

### 5.2.2 Feature Extraction

Seventeen features were selected from three categories: PAT beams, PAT beam envelopes, and PAT images. Spectral parameters from the PAT beams revealed the distribution of the frequency components within the frequency range of the transducer array which could be related to vasculature dimension and concentration.[24–29] Features from PAT beam envelopes, such as the total summation of envelopes (PAT summation)[33] and the peak envelope, described the light absorption distribution within the suspicious area. Statistical analysis was performed on the PAT images to obtain their mean values and variances. By separately applying several spatial filters constructed from the joint frequency spectrum of the malignant or normal cases, the common features which were not visibly distinguishable but were embedded in the spatial spectrum of the PAT image could be extracted.[23]

#### 5.2.2.1 Spectrum parameters of photoacoustic tomography beams

Power spectra were calculated using fast Fourier transform (FFT) on the PAT beams inside the cropped window. The cropped rectangular window defined the angular sector and the depth range of PAT beams inside the window. To ensure a high quality spectral estimation, any beams with SNR below 15 dB were excluded from spectral information extraction. The spectrum of PAT beam normalized to the spectrum of an approximate point-like target (a 100-μm black thread orthogonal to PAT imaging plane) was used to estimate the spectral slope and 0-MHz intercept.[29] A linear fitting was performed on the normalized spectrum in logarithmic scale within the 80% bandwidth of transducer's 6-MHz central frequency. The spectrum of an approximate point-like target characterizes the frequency response of the transducer and the electrical receiving system.[29] The PAT beam and its spectrum obtained from the approximate point target-like were shown in Figure 5.1. After taking the average of the spectral slopes and 0-MHz

intercept obtained from all high quality beams, the mean spectral slope and 0-MHz intercept were chosen as spectral features.

### 5. 2.2.2 Features of photoacoustic tomography beam envelope

PAT beam envelopes contain the amplitude information of PAT beams. The system noise threshold was estimated first from the average peaks of the PAT beam envelopes in the nonROIs, where almost no photoacoustic signals were generated. The system noise threshold was used as a cutoff value for PAT image formation. The count of image pixels with light absorption higher than the system noise threshold is defined as the PAT area and the summation of the envelopes of these pixels is defined as PAT summation.[33] PAT summation describes the total light absorption within the suspicious area. Peak envelope is the maximum of PAT beam envelope within the suspicious area, representing the maximum light absorption. It is a replacement for the single parameter AMRF used in Reference 18. Compared with AMRF, peak envelope is less affected by noise since the delay-and-sum beamforming can effectively increase the SNR of the PAT beams. We characterized the homogeneity of the PAT beam envelopes by the mean correlation coefficients of adjacent envelopes within the cropped windows since the light fluences along adjacent beam directions were similar. The histogram of PAT beam envelope was used to carry out an estimation of probability density function of Rayleigh distribution.[34] The scale parameter of the Rayleigh distribution was also chosen as one of the features.

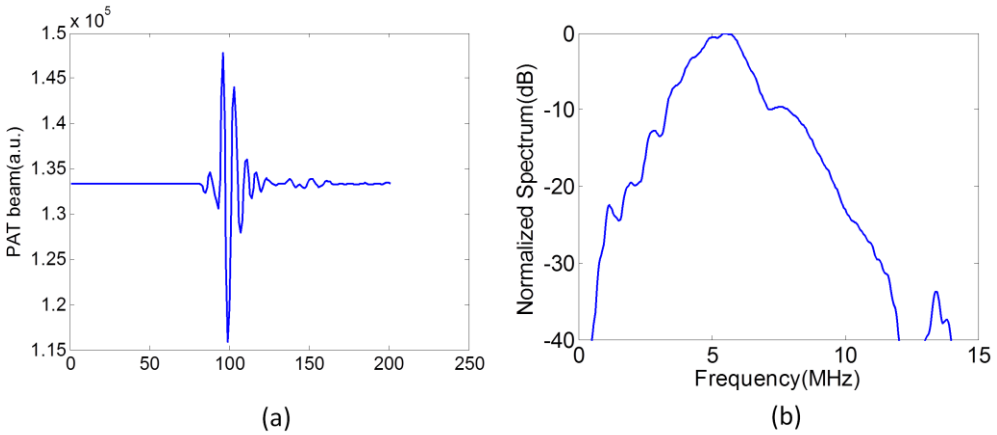


Figure 5.1 Waveform of PAT beam of a point-like target (a) and its spectrum (b).

#### 5.2.2.3 Features of photoacoustic tomography images

The features from the PAT images were mainly adopted from Reference 23. The mean and variance of the PAT images describes the average light absorption intensity and the spatial variation of the absorption. From our experimental observations, the PAT images of malignant cases usually showed clustered distributions due to the abundant and localized smaller vessels, whereas the distribution was more diffused, scattered, and spatially spread out in normal cases.[23] The center estimation method outlined in section 5.2.1 was extended to quantify this observation as follows: the normalized radon transforms from 0 degree to 90 degrees with an interval of 1 degree were calculated and fed to the Gaussian model after averaging. The parameter sigma ($\sigma$) estimated from the mean radon transform was used as a feature to describe the overall spatial spread of photoacoustic intensity. A high value of Gaussian fitting error meant a high irregularity of PAT spatial distribution.[23] This error was defined as the norm of the difference between the mean radon transform and the fitting value of the Gaussian model.

Two sets of optimum spatial filters were constructed from the existing malignant[23] and normal ovarian tissue PAT images, which served as image templates for malignant and normal

ovaries, respectively (see Reference 23 for more details). When the order parameter k of the spatial filter was set to 1, the filter was linear. Additional nonlinear versions (cubic root and binary) of this filter were achieved by setting k to 1/3 and 0.01, respectively, to make them more tolerant to distortions and obtain better recognition SNR.[35] The peak outputs of the two sets of spatial filters were chosen as features for two classifiers. High peak outputs of spatial filters constructed from malignant PAT image templates and low outputs of spatial filters constructed from normal PAT image templates were expected to be an indication of cancer. On the other hand, high peak outputs of spatial filters constructed from normal PAT image templates and low outputs of spatial filters constructed from malignant PAT image templates were more likely to be an indication of normal cases.

### 5.2.3 Logistic and Support Vector Machine Classifier

Logistic regression was widely used for the binary classification[36] in clinical studies using the following logistic function:

$$F(\vec{x}) = \frac{1}{1 + e^{-(\beta_0 + \sum_1^n \beta_i x_i)}} \tag{5.2}$$

In the above equation, $\vec{x}$ is the feature vector, $\beta_0$ is a constant term, and $\beta_i$ is the coefficient for each feature $x_i$. The constant term and coefficients can be estimated from the training group data using maximum likelihood estimation (MLE) with label 0 representing 'normal' and label 1 representing 'malignant'. For the testing group, samples with corresponding logistic function values less than the cutoff value (usually 0.5) are classified as label 0 (normal) while the rest are classified as label 1 (malignant). By varying the cutoff value, the receiver operating characteristic (ROC) curve can be derived and the area under ROC curve (AUC) can be calculated to demonstrate the performance of this logistic classifier.

Our previous study had shown the feasibility and good performance of SVM classifier for ovarian tissue characterization. and classification.[23] SVM with different kernels can be used to map the input data to higher dimensional feature spaces and find the hyperplane with maximum distance to the two input populations.[37,38] In this application, a radial basis function (RBF)kernel was used. The training was terminated when 100% sensitivity and 100% specificity were achieved or when a high number of iterations (1000) had been reached. The trained SVM structure was then applied to the testing samples for validation.

Table 5.1 17 extracted PAT features and indices of the 13 features after feature correlation analysis and ranking

| Feature Category | # of features | Features in each category |
|---|---|---|
| Spectral parameters from beam data | 2 | Mean spectral slope of PAT beams |
| | | mean 0-MHz intercept |
| Features from beam envelopes | 5 | PAT area |
| | | PAT summation |
| | | maximum PAT envelope |
| | | PAT envelope homogeneity |
| | | scale parameter of Rayleigh fitting of envelopes |
| Features from PAT images | 10 | PAT Mean |
| | | PAT Variance |
| | | spatial spread of suspicious area |
| | | Gaussian fitting error of mean Radon transform |
| | | peak outputs of spatial filters (malignant template, k = 1) |
| | | peak outputs of spatial filters (malignant template, k = 1/3) |
| | | peak outputs of spatial filters (malignant template, k = 0.01) |
| | | peak outputs of spatial filters (normal template, k = 1) |
| | | peak outputs of spatial filters (normal template, k = 1/3) |
| | | peak outputs of spatial filters (normal template, k = 0.01) |

### 5.2.4 Features Selection

Both the logistic model and SVM have better performances if the input features are independently distinguishable. However, this is not the case for all of the 17 extracted features. There are three features from the maximum output of spatial filters constructed from malignant PAT image templates and three from normal PAT image templates. Each set of three features is highly correlated and we have selected one feature each from the maximum outputs of malignant and normal PAT templates, respectively. These two features are independent and yielded the lowest p-values from t-tests.

For the general purpose of feature selection, two types of approaches may be used: (1) filters and (2) wrappers.[39,40] With the first method, features are selected based on intrinsic characteristics such as mutual information, statistical tests, or correlations between features. The selected features are uncorrelated to that of the learning methods, resulting in a better generalization property. In the wrappers type method, features' selection is "wrapped" around a learning method: here, the usefulness of a feature is directly judged by the estimated accuracy of the learning method.[41,42] Though wrappers type methods can give a high accuracy with a very small number of non-redundant features, the generalization property is not as good as filter type methods. Since the samples in our study were very limited, we adopted the filters type method to rank the rest of the 11 features for a better generalization property. The simplest way of "filter" method is ranking features by the descending order of the p-values of t-tests between features and classes. It was reasonable because the remaining 11 features were non-correlated in nature.

Then, logistic and SVM classifiers were trained on half of the malignant samples and half of the normal/benign samples with different numbers of ranked features, while the remaining samples were used for testing. The data resampling procedure was repeated 50 times to obtain the mean values of sensitivities, specificities, positive predictive values (PPVs), negative predictive

values (NPVs), and misclassification errors (MCEs) for the evaluation of the performances of two classifiers. The number of selected features was determined when the minimum of the mean MCE was reached.

## 5.3 Results and Discussions

Table 1 lists 17 extracted features. Among the 17 features, features from the first two categories and the maximum output of the spatial filters constructed from normal ovaries are new features in addition to those reported in References 18 and 23. The new features provide additional information from the spectrum of PAT beams and the quantitative description of light absorption in suspicious areas.

For other result, readers are encouraged to find them in Reference 44. The details of result are not shown in this dissertation to avoid possible issues in the future but summary will be presented in the following paragraphs. From the curve of MCE versus number of features after ranking, we can determine the optimal number of features for final classification by choosing it when the MCE hit its global minimum. It is expected that the MCE drops as the number of features after ranking increases before the optimal number of features, and then MCE increases as number of features increases after that. According, we can get the sensitivity, specificity, PPV and NPV versus number of features after ranking. It is possible that not all of these four performances achieve best value at the same number of features. So in this study, we just simply use MCE as the criterion for choosing optimal number of features and use the mean values of sensitivity, specificity, PPV and NPV as the performance of each classifier.

After getting optimal features after ranking, performances of classifiers can be evaluated based on cross-validation. In this study, we just used the average performance of 50 runs of equal and random partitions of our data pool as performance of classifiers. In the data set in Reference 44, SVM shows a slightly better performance than logistic regression. However, it is not

guaranteed that SVM will always be better for bigger data pool in the future. One reason is that comparing with logistic regression, the boundary of SVM is very rigid. It is more likely for SVM to get in trouble of overfitting than logistic regression, which means that SVM may get better result for current data set but fail to perform well in other set. Logistic regression has a smoother change from malignant to benign because it is based on weight of each feature. In nature, it can automatically rank the features but may fail if the number of features is too large or some features are closely correlated. It may have a better general application in practice than SVM. In current data set, there are some similar frames used in data pool. In this case, correlation between features may be high. However, SVM only rely on support vector as boundary, the correlated data will not affect its performance. That is one big advantage for SVM over logistic regression. According to author's experience, the key point for this study still relies on the feature extraction. Once feature extraction is done, there is no big difference for different classifiers (logistic regression, SVM, neuron network and etc).

## 5.4 Other Features for *in vivo* Study and Improvements

In Reference 45, there is no useful information (features) about ultrasound data. However, the US features are possible to carry information for diagnosis. The US spectrum analysis developed by Lizzi and co-workers [45,46] showed that US pulse-echo (PE) spectral parameters are related to the lesion attenuation, sizes, concentrations and relative acoustic impedances of scatters. These features have shown promise in cancer detection and classification of the eye[46], prostate [47], and breast[48]. These features may be useful for improving PAT feature-based classification of malignant and benign ovarian tissues as well. Three features can be extracted from the PE beams after calibration with the transducer frequency response for spectral analysis; they are: PE spectral slope, PE 0MHz intercept, and PE mid-band fit. Every PE beam segment in the ROI need to be multiplied by a Hamming window before spectral feature extraction. The averaged value of each spectral feature can be used to characterize each imaging frame. In addition, we

can also extract the ovary area in B-scan from the PE images by modeling the ovary as ellipsoid and measuring the lengths of the long and short axes, because malignant ovaries usually have a larger size than benign ones in the *ex vivo* data. We can also include the menopausal status of patients in our extracted features for classifier input (1: postmenopausal, 0: premenopausal).

Another possible improvement for this classification study is to improve the feature selection method for classifiers. Section 5.2 has already shown some of techniques, including filter type or wrapper type of feature selection. When the number of features is small (<20), then it is possible that we exam the every possible combination of features. For larger number of feature, a greedy feature selection method is also possible, such as forward feature selection method or backward feature selection method. The result of greedy algorithm (e.g., forward feature selection) may not be global optimal but it can save us a lot time for computing. It is a trade off for computing time and accuracy. In this study, all the parameters in logistic regression and SVM are default parameters in MATLAB. It is also possible to improve the performance of them by fine tuning these parameters.

The goal of this chapter is to find useful PE/PAT features for the aid of diagnosis of ovary cancer. In current state, we have only limited analysis on ex-vivo ovary data. In the next step, with reasonable number of in-vivo ovary data set, a comparison study of ex-vivo data and in-vivo data will be conducted. This feature-based classification can be extended for in-vivo classification if they are comparable for certain features. For these non-comparable features, we may exclude them for in-vivo studies; especially features related to the absolute value of light fluence may be strongly affected).

The ideal case for this study should be only based on large data pool of in-vivo ovaries. At that time, more PE/PAT features can be used, such as oxygen saturation level. If we keep light delivery system unchanged, the light fluence related PAT feature will also survive for in-vivo

study. Another way for the improvement is the combination of PE/PAT with Diffuse Optical Tomography, which is another topic called quantitive PAT, to extract quantitive optical absorption inside tissues.

Although there is a lot of drawbacks in this study, but I believe with the development of light delivery, ultrasound detection probe, computer science, artificial intelligence and the further exploration of cancer mechanism, computer aided diagnosis for human disease, not only for ovarian cancer, will definitely come into clinical application in coming future.

## References


1. R. M. Anne et al., “Predictive value of symptoms for early detection of ovarian cancer,” J. Natl. Cancer Inst. 102(4), 222–229 (2010).

2. D. A. Fishman et al., “The role of ultrasound evaluation in the detection of early-stage epithelial ovarian cancer,” Am. J. Obstet. Gynecol. 192(4), 1214–1222 (2005).

3. V. Seltzer et al., “Ovarian cancer: screening, treatment, and follow-up,” NIH Consensus Statement 273(6), 491–497 (1995).

4. J. Tammela and S. Lele, “New modalities in detection of recurrent ovarian cancer,” Curr. Opin. Obstet. Gynecol. 16(1), 5–9 (2004).

5. A. Shaaban and M. Rezvani, “Ovarian cancer: detection and radiologic staging,” Clin. Obstet. Gynecol. 52(1), 73–93 (2009).

6. V. Nossov et al., “The early detection of ovarian cancer: from traditional methods to proteomics. Can we really do better than serum CA-125?” Am. J. Obstet. Gynecol. 199(3), 215–223 (2008).

7. B. V. Calster et al., “Discrimination between benign and malignant adnexal masses by specialist ultrasound examination versus serum CA-125,” J. Natl. Cancer Inst. 99(22), 1706–1714 (2007).

8. M. Goozner, “Personalizing ovarian cancer screening,” J. Natl. Cancer.Inst. 102(15), 1112–1113 (2010).

9. C. K. Kim et al., “Detection of recurrent ovarian cancer at MRI: comparison with integrated PET/CT,” J. Comput. Assist. Tomogr. 31(6),868–875 (2007).

10. S. Hongju et al., “Role of FDG PET/CT in staging of recurrent ovarian cancer,” Radiographics 31(2), 569–583 (2011).

11. I. Jacobs et al., “A risk of malignancy index incorporating CA 125, ultrasound and menopausal status for the accurate preoperative diagnosis of ovarian cancer,” Br. J. Obstet. Gynecol. 97(10), 922–929 (1990).

12. W. Moolthiya and P. Yuenyao, “The risk of malignancy index (RMI) in diagnosis of ovarian malignancy,” Asian Pac. J. Cancer Prev. 10(5), 865–868 (2009).

13. D. Timmerman et al., “Simple ultrasound-based rules for the diagnosis of ovarian cancer,” Ultrasound Obstet. Gynecol. 31(6), 681–690 (2008).

14. E. Fruscella et al., “Sonographic features of decidualized ovarian endometriosis suspicious for malignancy,” Ultrasound Obstet. Gynecol.24(5), 578–580 (2004).

15. M. Pramanik et al., “Design and evaluation of a novel breast cancer detection system combining both thermoacoustic (TA) and photoacoustic (PA) tomography,” Med. Phys. 35(6), 2218–2223 (2008).

16. L. V. Wang, “Prospects of photoacoustic tomography,” Med. Phys. 35(12), 5758–5767 (2008).

17. J. Jose et al., “Imaging of tumor vasculature using Twente photoacoustic systems,” J. Biophotonics 2(12), 701–717 (2009).

18. A. Aguirre et al., “Potential role of coregistered photoacoustic and ultrasound imaging in ovarian cancer detection and characterization,” Transl. Oncol. 4(1), 29–37 (2011).

19. P. Vaupel et al., “Blood flow, oxygen and nutrient supply, and metabolic microenvironment of human tumors: a review,” Cancer Res. 49(23), 6449–6465 (1989).

20. J. Gamelin et al., “Curved array photoacoustic tomographic system for small animal imaging,” J. Biomed. Opt. 13(2), 024007 (2008).

21. A. Aguirre et al., “Coregistered 3-D ultrasound and photoacoustic imaging system for ovarian tissue characterization,” J. Biomed. Opt. 14(5), 054014 (2009).

22. U. Alqasemi et al., “FPGA-based reconfigurable processor for ultrafast interlaced ultrasound and photoacoustic imaging,” IEEE Trans. Ultrason. Ferroelectr. Freq. Control 59(7), (2012).

23. U. Alqasemi et al., “Recognition algorithm for assisting ovarian cancer diagnosis from coregistered ultrasound and photoacoustic images: *ex vivo* study,” J. Biomed. Opt. 17(12), 126003 (2012).

24. G. Xu et al., “Photoacoustic spectrum analysis for microstructure characterization

in biological tissue: a feasibility study,” Appl. Phys. Lett. 101(22), 221102–221105 (2012).

25. S. Wang et al., “Quantitative detection of stochastic microstructure in turbid media by photoacoustic spectral matching,” Appl. Phys. Lett. 102(11), 114102 (2013).

26. Y. Yang et al., “Photoacoustic tomography of tissue subwavelength microstructure with a narrowband and low frequency system,” Appl. Phys. Lett. 101(3), 034105 (2012).

27. S. D. Kamath et al., “Photoacoustic spectroscopy of ovarian normal, benign, and malignant tissues: a pilot study,” J. Biomed. Opt. 16(6), 067001 (2011).

28. G. Xu et al., “The functional pitch of an organ: quantification of tissue texture with photoacoustic spectrum analysis,” Radiology. 271(1),248–254 (2014).

29. R. E. Kumon et al., “Frequency-domain analysis of photoacoustic imaging data from prostate adenocarcinoma tumors in a murine model,” Ultrasound Med. Biol. 37(5), 834–839 (2011).

30. P. Kumavor et al., “Co-registered pulse-echo/photoacoustic transvaginal probe for real time imaging of ovarian tissue,” J. Biophotonics 6(6–7), (2013).

31. R. A. Mucci, “A comparison of efficient beamforming algorithms,” IEEE Trans. Acoust. Speech, Signal Process. 32(3), 548–558 (1984).

32. C. G. A. Hoelen and F. F. M. de Mul, “Image reconstruction for photoacoustic scanning of tissue structures,” Appl. Opt. 39(31), 5872–5883 (2000).

33. S. Zanganeh et al., “Photoacoustic imaging enhanced by Indocyanine green-conjugated single-wall carbon nanotubes,” J. Biomed. Opt. 18(9), 096006 (2013)

34. R. C. Molthen et al., “Comparisons of the Rayleigh and K-distribution models using in vivo breast and liver tissue,” Ultrasound Med. Biol. 24(1), 93–100 (1998).

35. B. Javidi and D. Painchaud, “Distortion-invariant pattern recognition with fourier-plane nonlinear filters,” Appl. Opt. 35(2), 318–331 (1996).

36. T. H. Wang et al., “Characterization of ovarian tissue based on quantitative analysis of photoacoustic microscopy images,” Biomed. Opt. Express. 4(12), 2763–2768 (2013).

37. C.-C. Chang and C.-J. Lin, “LIBSVM: a library for support vector machines,” ACM Trans. Intell. Syst. Technol. 2(3), 1–27 (2011).

38. N. Cristianini and J. Shawe-Taylor, An Introduction to Support Vector Machines and Other Kernel-Based Learning Methods, Cambridge University Press, Cambridge, UK (2000).

39. R. Kohavi and G. John, “Wrapper for feature subset selection,” Artif. Intell. 97(1–2), 273–324 (1997).

40. P. Langley, “Selection of relevant features in machine learning,” in Proc. AAAI Fall Symp. on Relevance, pp. 140–144, AAAI Press, New Orleans, Louisiana (1994).

41. C. Ding and H. C. Peng, “Minimum redundancy feature selection from microarray gene expression data,” J. Bioinform. Comput. Biol. 3(2),185–205 (2005).

42. H.C. Peng, F.H. Long, and C. Ding, “Feature selection based on mutual information: criteria of max-dependency, max-relevance, and min-redundancy,” IEEE Trans. Pattern Anal. Mach. Intell. 27(8), 1226–1238(2005).

43. X. Robin et al., “pROC: an open-source package for R and S+ to analyze and compare ROC curves,” BMC Bioinf. 12, 77 (2011).

44. Li H, Kumavor P, Alqasemil U, Zhu Q, "Utilizing spatial and spectral features of photoacoustic imaging for ovarian cancer detection and diagnosis.", J. Biomed Opt.; Jan;20(1):016002. doi: 10.1117/1.JBO.20.1.016002(2014).

45.F. L. Lizzi, S. K. Alam, S. Mikaelian, P. Lee, and E. J. Feleppa, “On the statistics of ultrasonic spectral parameters,” Ultrasound Med. Biol. 32(11), 1671–1685 (2006).

46. E. J. Feleppa, F. L. Lizzi, D. J. Coleman, and M. M. Yaremko, “Diagnostic spectrum analysis in ophthalmology: A physical perspective,” Ultrasound Med. Biol. 12, 623–631 (1986).

47. E. J. Feleppa, R. D. Ennis, P. B. Schiff, C. S. Wuu, A. Kalisz, J. Ketterling, S. Urban, T. Liu, W. R. Fair, C. R. Porter, and J. R. Gillespie, “Ultrasonic spectrum-analysis and neural-network classification as a basis for ultrasonic imaging to target brachytherapy of prostate cancer,” Brachytherapy 1, 48–53 (2002).

48. S. K. Alam, F. L. Lizzi, E. J. Feleppa, T. Liu, and A. Kalisz, “Computeraided diagnosis of breast lesions using a multifeature analysis procedure,” SPIE Medical Imaging 4687, 296–303 (2002).

# Chapter 6 Conclusion and Future work

The main objective of this study is to design and implement real-time co-registered ultrasound/photoacoustic tomography system for clinical study of ovarian tissues and characterize ovarian tissues based on photoacoustic / ultrasound features. Two versions of US/PAT systems were built in this procedure. The first version is based on FPGAs-DSP-PC structure. Front end circuits are controlled by modules FPGAs; DSP acts as data coordinator and intermediate controller; PC is responsible for reconstruction and display. Ultrasound PE mode and photoacoustic PAT mode are run in a sequential way instead of the true TDM fashion in our second system. Other design drawbacks, such as low data transfer rate between FPGAs and DSP and Ethernet cable, are also the limitations for this system. This is our first try and we make the online coregisration of PE/PAT implemented, although the speed is only 1 fps on average. Phantom, mouse model and ex-vivo ovarian experiments showed that this first system had good resolution and potential to perform real-time imaging after solving these bottlenecks.

The second version of US/PAT system improved a lot by overcoming the low data transfer rate problem. It is base on FPGAs-FPGA-PC structure. We kept the multiple module FPGAs in our first system design and upgrade the DSP to an advanced FPGAs with PCIe bus. LVDS solved the data transfer of module FPGAs to PCIe FPGA and DMA based PCIe transfer solved the bulk data transfer to PC and reformed the structure of software on PC. Instead of sequential PE and PAT DAQ then processing, multi-threads techniques allowed this second system to process buffered data and acquired new data simultaneously. The maximum imaging frame rate is 15 fps in Coregistered mode, which is limited by laser pulse repetition rate. This real-time feature made it practical for clinical application. Figure 6.1 shows the picture of this system in UCONN health center.

The performance of our newly developed contract agent SWCNT/ICG was also demonstrated by long time PAT monitoring with laser energy shift compensation. It significantly improved the PAT SNR after injection, which is very helpful for PAT application because the SNR from nature contrast agent (Hb and HbO2) was relatively low.

Classification algorithm was based on PAT features only. All types of data in the procedure of processing were used, especially the PAT spectral features. They provided different views of light absorption inside ovarian tissues in either spectral domain or spatial distribution domain. Typical feature selection and classical classifiers were explored. With optimal feature set, both of logistic regression and SVM achieved high sensitivity and high specificity (both were over 90%).

Although we have gotten good result so far, there is still room for system and classification algorithm improvement. Traditional ultrasound imaging features, such as Doppler imaging, can also be implemented in our system. However, it needs to reform current system design. Processing of US B-Mode imaging can no longer be handled by CPU. Instead, direct processing in FPGAs is the best option. A compromise method is to use GPU for parallel processing. Even, in our system design, the performance of system can be promoted by state-of-art GPU with well written algorithm.

In current classification algorithm, there is still a lack of quantitive features. So quantitive ultrasound analysis may be very helpful for ovarian tissue characterization and diagnosis. It may require storing the ultrasound RF data, which will not be a burden for PCIe bus. Feature selection and other classifiers can also be explored. Techniques to reduce the impact of redundant features are also valuable in this study.

As stated in Chapter 5, comparison study of ex-vivo and in-vivo ovarian tissue should be conducted in near future to validate if the framework of classification works for in-vivo ovarian

tissue. In ideal cases, features should only be extracted from all in-vivo ovarian tissues with high quality imaging system and laser system. Besides the features from ultrasound and photoacoustic information, any other type of imaging and test can be combined to aid the diagnosis of ovarian disease. With the development of artificial intelligence, machine learning and screening techniques, not only photoacoustic but also other types of imaging modules, the early detection of ovarian cancer will finally come true.

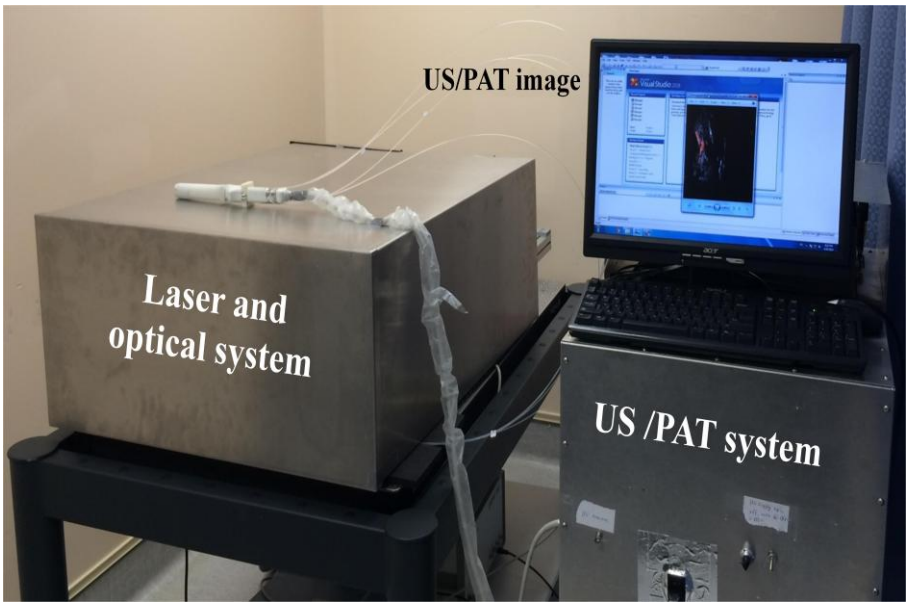


Figure 6.1Photograph of real-time US/PAT system in UCONN health center

# List of Publications

**Journals:**

1) **Hai Li**; Patrick Kumavor; Umar Salman Alqasemi; Quing Zhu, "Utilizing spatial and spectral features of photoacoustic imaging for ovarian cancer detection and diagnosis", J. Biomed. Opt. 20 (1), 016002 (January 02, 2015).

2) Umar Alqasemi*, **Hai Li***, Guangqian Yuan, Patrick Kumavor, Saeid Zanganeh, and Quing Zhu, "Interlaced photoacoustic and ultrasound imaging system with real-time co-registration for ovarian tissue characterization", J Biomed Opt.; 19(7):76020(Jul ,2014)

3) Zanganeh S*, **Li H***, Kumavor PD, Alqasemi U, Aguirre A, Mohammad I, Stanford C, Smith MB, Zhu Q, "Photoacoustic imaging enhanced by ICG conjugated single wall carbon nanotubes", J Biomed Opt.;18(9):096006(Sep , 2013).

4) Kumavor PD., Alqasemi U, Tavakoli B, **Li H**, Yang Y, Sun X, Warych E and Zhu Q, "Co-registered Pulse-Echo/Photoacoustic Transvaginal Probe for Real Time Imaging of Ovarian Tissue", J Biophotonics.;6(6-7):475-484(Jun , 2013).

5) Hassan S. Salehi, Tianheng Wang, Patrick D. Kumavor, **Hai Li**, and Quing Zhu, "Design of miniaturized illumination for transvaginal co-registered photoacoustic and ultrasound imaging", Biomedical Optics Express, Vol. 5, Issue 9, pp. 3074-3079 (2014).

6) Alqasemi U., **Li H. **,** Aguirre A. and Zhu Q., "FPGA-based Reconfigurable Processor for Ultrafast Interlaced Ultrasound and Photoacoustic Imaging", IEEE Transaction on Ultrasonic, Ferroelectrics and Frequency Control 2012 Jul;59(7):1344-53(2012).

7) Xu C, Kumavor PD, Alqasemi U, **Li H**, Xu Y, Zanganeh S, Zhu Q , "Indocyanine green enhanced co-registered diffuse optical tomography and photoacoustic tomography", J Biomed Opt.;18(12):126006(Dec , 2013).

8) Xu C, Vavadi H, Merkulov A., **Li H**, Erfanzadeh, M, Mostafa A, Gong Y, Hassan Salehi H, Tannenbaum S, "Ultrasound-guided Diffuse Optical Tomography for Predicting and Monitoring Neoadjuvant Chemotherapy of Breast Cancers: Recent Progress", Ultrasonic Imaging (April 17, 2015)

* Equal contribution **Cover letter

**Conference Proceedings:**

9) Saeid Zanganeh, Andres Aguirre, Nrusingh C. Biswal, Christopher Pavlik, Michael B. Smith, Umar Alqasemi, **Hai Li**, Quing Zhu, "Hypoxia targeted carbon nanotubes as a sensitive contrast agent for photoacoustic imaging of tumors", Proc. SPIE 7899, Photons Plus Ultrasound: Imaging and Sensing 2011, 78991S (February 28, 2011);

10) Umar Alqasemi, **Hai Li,** Andres Aguirre, Quing Zhu, "Real-time co-registered ultrasound and photoacoustic imaging system based on FPGA and DSP architecture", Proc. SPIE 7899, Photons Plus Ultrasound: Imaging and Sensing 2011, 78993S (February 23, 2011);

11) Umar Alqasemi, **Hai Li**, Guangqian Yuan, Andres Aguirre, Quing Zhu, "Ultrafast ultrasound and photoacoustic co-registered imaging system based on FPGA parallel processing". Proc. SPIE 8223, Photons Plus Ultrasound: Imaging and Sensing 2012, 82232U (February 9, 2012);

12) Saeid Zanganeh, **Hai Li**, Patrick Kumavor, Umar Alqasemi, Andres Aguirre, Innus Mohammad, Courtney Stanford, Michael B. Smith, Quing Zhu, "Single wall carbon nanotube/bis carboxylic acid-ICG as a sensitive contrast agent for in vivo tumor imaging in photoacoustic tomography", Photons Plus Ultrasound: Imaging and Sensing 2013(Mar, 2013)

13) Patrick D. Kumavor, Umar Alqasemi, Behnoosh Tavakoli, **Hai Li**, Yi Yang, Quing Zhu," Transvaginal photoacoustic imaging probe and system based on a multiport fiber-optic beamsplitter and a real time imager for ovarian cancer detection", Photons Plus Ultrasound: Imaging and Sensing 2013(Mar, 2013)

14) Umar Alqasemi, **Hai Li**, Guangqian Yuan, Patrick Kumavor, Saeid Zanganeh, Quing Zhu," Real-time interlaced ultrasound and photoacoustic system for in vivo ovarian tissue imaging", Photons Plus Ultrasound: Imaging and Sensing 2013(Mar, 2013)

15) **Hai Li**, Patrick D. Kumavor, Umar Alqasemi, Quing Zhu," Classification algorithm of ovarian tissue based on co-registered ultrasound and photoacoustic tomography", SPIE Photonics West, Photons Plus Ultrasound: Imaging and Sensing, San Francisco, USA (Mar, 2014)

16) Hassan S. Salehi, Patrick D. Kumavor, Umar Alqasemi, **Hai Li**, Tianheng Wang, Quing Zhu, " High-throughput fiber-array transvaginal ultrasound/photoacoustic probe for ovarian cancer imaging", SPIE Photonics West, Photons Plus Ultrasound: Imaging and Sensing, San Francisco, USA(Mar, 2014)

17) Chen Xu, Hamed Vavadi, Jiqi Chen, Mohsen Erfanzadeh, Quangqian Yuan, Yanping Gong, Hassan Salehi, **Hai Li**, Quing Zhu," Toward Miniature Diffuse Optical Tomography System for Assessing Neoadjuvant Chemotherapy", OSA's BIOMED 2014, Miami, Florida United States(Apr,2014 )

18) Hassan Salehi, Tianheng Wang, **Hai Li**, Patrick Kumavor, Quing Zhu," Co-Registered Ultrasound and Photoacoustic Probe with a Miniaturized Light Illumination Scheme for in vivo Ovarian Cancer Imaging", Biomedical Optics, Miami, Florida United States(Apr, 2014)